2004

Characterization of the microstructure and corrosion behavior of AL-6XN friction stir welds

Suzanna M. Klingensmith
Lehigh University

Klingensmith, Suzanna M.

Characterization of the Microstructure and Corrosion Behavior of AL-6XN Friction Stir...

May 2004

Characterization of the Microstructure and Corrosion Behavior of AL-6XN Friction Stir Welds

by

Suzanna M. Klingensmith

A Thesis

Presented to the Graduate and Research Committee

of Lehigh University

In Candidacy for the Degree of Master of Science

in

Materials Science and Engineering

Lehigh University

April 2004

This thesis is accepted and approved in partial fulfillment of the requirements for the Master of Science.

4-27-04

Date

Thesis Advisor – A.R. Marder

Co-Advisor – J.N. DuPont

Chairperson of Department

Acknowledgements

I would first like to thank my advisor, Dr. Arnold Marder, for approaching me about graduate school and making my being here possible. Throughout my career at Lehigh University I have learned a great deal from you and from my experiences. Not only have I learned valuable work skills, I have also been taught invaluable life lessons. A thank you is also extended to the Office of Naval Research, the sponsors whose financial support has made this work possible.

Through my six years at Lehigh University many others have helped me. A big thanks John DuPont, my foster advisor, who has provided me with his knowledge of welding to help me grasp the details of friction stir welding. I would also like to thank Arlan Benscoter for assistance and training in the black art of metallography and with whom I can sympathize about trying to keep a "clean house" despite the attempts of all others. And thanks to my fellow EMG members – Jon Regina, Matt Perricone, Weiping Lui, Ryan Deacon, Shane Para, Rick Noecker, Ken Adams, Tim Anderson, and Mike Minicozzi. I do not think there will be another time when I find myself surrounded by so many wonderful and handsome men. You guys truly treat me like a princess, tee-hee and a hair toss. But seriously, thank you for letting me be me.

I would like to thank my parents, Marshall and Sandi Klingensmith. Your constant support and encouragements, high expectations, and love have made me the amazing person I am today. And finally, to Matt, my fiancé, you have been through this journey with me every step of the way. You have been so many things to me – my

shoulder to cry on, the arms that hold me, the words that soothe me, and the heart that loves me. Thank you, Thank you, Thank you. I love you.

Table of Contents

List of Tables

List Of Figures

Abstract

The Navy has proposed a new Advanced Double Hull (ADH) design for the fabrication of naval combatants which offers numerous benefits compared to the present design. AL-6XN is an attractive material for the ADH design because of its superior mechanical properties, high corrosion resistance, non-magnetic structure, high availability, and relatively inexpensive cost. When fusion welded, however, the corrosion resistance of AL-6XN is severely degraded as a result of a solidification defect – microsegregation. In using a solid-state welding process such as friction stir welding (FSW), solidification defects are not an issue. In this research, the microstructures and corrosion behavior of AL-6XN FS welds are characterized and the corrosion properties are investigated.

The microstructural zones that develop during FSW reflect decreasing strains and less severe thermal cycles with increasing distance from the weld centerline. The *nugget*, located around the centerline, has a refined structure of equiaxed grains as a result of the extreme strain and temperatures experienced during welding. The *heat affected zone* consists of a mixture of relatively large austenite grains and smaller recrystallized grains nucleated at grain boundaries. The *thermal mechanical affected zone*, located between the nugget and heat affected zone, shows a microstructural transition from the completely refined structure to a structure very similar to the base metal. Due to the changing microstructure from base metal to the weld zone, there are corresponding changes in hardness. Moving towards the centerline from the base metal, hardness increases due to refinement of the microstructure.

Of particular importance is that microsegregation was avoided and the corrosion resistance of the FS weld should be similar to the base metal. A variety of tests were performed to assess the corrosion performance of the welds including both immersion tests and electrochemical tests. The tests that most closely mimic the true marine environment suggest that FS welds have superior resistance to fusion welds and only slightly lower resistance to as-received plate.

1. Introduction

FSW is a relatively new joining technique that is gaining a great deal of interest in the industrial community as a possible alternative to fusion welding. Presently, FSW is used to join aluminum and is producing welds with outstanding properties. The range of materials joined by FSW is expanding rapidly and now includes high-strength materials like stainless steels.

In comparison to aluminum, little research has been dedicated to FS welding of steels because steels are readily fusion welded. A major shortcoming of fusion welds on stainless steels is the unavoidable solidification defect – microsegregation. Microsegregation results in Mo-depleted dendrite cores that are highly susceptible to pitting. FSW is being explored as an alternative joining method with hopes of improving the poor corrosion resistance of stainless steel welds.

At present, only a few studies have been dedicated to understanding the microstructural development of stainless steel FS welds. There have been no studies on the corrosion behavior of these welds. The goal of this study is to thoroughly characterize the microstructure and the corrosion behavior of an AL-6XN FS weld.

2. Background

2.1 Friction Stir Welding

2.1.1 Basic Friction Stir Welding

Friction stir welding (FSW), developed by The Welding Institute (TWI) in 1991[1] is a solid-state welding process that offers an attractive alternative to arc welding. The entire process appears relatively simple in that a rotating tool is plunged between the surfaces of two abutting plates and is then traversed along the length of the plates, Figure 2-1. Details of the tool and several processing terms are identified in this image. As seen, the FSW tool consists of a *pin* and a *shoulder*. During welding, the pin rotates beneath the plate surface and causes the majority of the material deformation and mixing. The pin material is different depending on the material to be welded but it must be harder than the base material to prevent significant tool wear[2]. The shoulder of the tool rotates across the plate surface at some controlled force and prevents the softened material in the weld zone from being expelled[3]. The *retreating* and *advancing* sides of the weld are defined by the direction of tool rotation with respect to the tool translation. Tool rotation and translation are in the same relative direction on the advancing side while tool rotation opposes the direction of translation on the retreating side. The *lead edge* of the tool refers to the front of the tool which reaches the virgin material first. The *trailing edge* refers to the side of the tool which passes over the weld last. The critical processing parameters of FSW include translational speed, tool rotational speed, and the force applied to the plate from the shoulder[4].

During the FSW process, frictional forces between the tool and plates create intense local heating. Although, temperatures may approach the melting temperature of the plates, they will remain solid. Figure 2-2 shows thermal cycles recorded via thermocouples placed 0.125 mm from the edge of the stir zone during FSW of hot-rolled AISI 1018 steel. Peak temperatures ranged from 590 to 665°C. At the shoulder/workpiece interface, temperature measurements, made via an infrared system, were higher, reaching approximately 990°C[4]. Similar to fusion welding, the thermal cycles produced by FSW are controlled by weld parameters and material properties. During FSW, material softens around the rotating tool such that a plasticized region of material is created[5]. Mixing the material from the two plates during FSW is complex but is often explained as a simple extrusion process. Tool rotation intimately mixes the plates together as it transfers material around the tool. Forward tool translation essentially extrudes the softened material backwards, in the opposite direction as tool translation[6,7,8]. The "extrusion die" is created by the tool and the unsoftened plate material[6,8,9]. The downward pressure of the tool shoulder, as it passes over the weld zone confines the softened material within the surface of the plate[3].

2.1.2 Material Flow

The above explanation is an oversimplification of material flow – more detailed models of flow have been developed. Although there is extensive research on this aspect of FSW, there is still uncertainty as to details of flow. K. Colligan[10] researched material flow of 6061-T6 and 7075-T6 aluminum alloys during FSW using a tracer line technique.

In this technique, a line of steel shot is embedded in the plate parallel to the weld direction. After welding, movement of the shot caused by material flow is tracked. For both alloys, tracer movement appeared similar. The original tracer line locations for the 6061-T6 plate are indicated as positions 1-14 in Figure 2-3A. The schematic representations of horizontal and vertical movement of tracers after welding are seen in Figures 2-3B and C, respectively. From these schematics, it is seen that tracer movement and thus material flow can be categorized as one of two types depending on the initial tracer location. Tracers at positions 1-3, located near the surface of the advancing side, show unique tracer movement with respect to the other positions. At these locations, final tracer position after welding appeared completely random. The horizontal distribution of tracers showed no correlation to their original linear configuration – they were chaotically distributed, Figure 2-3B. Positions 4-13 show less disruptive horizontal flow, in which a semi-continuous line of tracers persists after welding. Tracking of the vertical movement of tracers, Figure 2-3C, reveals a similar trend of a difference between positions 1-3 and positions 4-13. As tracers in positions 1-3 approach the tool, they were lifted slightly and then pulled downwards, below their original position. Tracer movement at positions 4-13 was in one direction – slightly upwards from original positions.

In summary, material flow at the surface of the advancing side (positions 1-3) is chaotic and disruptive whereas flow on the retreating side and below the surface (positions 4-13) is calmer, suggesting material deformation but less real mixing[10]. It should be noted that flow may differ depending on material and welding parameters. The

above description describes material flow for FS welds of two aluminum alloys produced at specific weld parameters. Numerous other attempts have been made to characterize material flow of FSW, some of which may agree or disagree with the aforementioned results.

2.1.3 Microstructural Zones and Properties

Similar to arc welding, distinct microstructural zones develop during FSW. The microstructures and thus properties of the zones in these two welding processes may, however, be very different. Generally, three regions are identified in FS welds – the nugget, the thermal mechanical affected zone (TMAZ), and the heat affected zone (HAZ). Figure 2-4 is an illustration of the approximate locations of these three regions in a generic case. It should be noted that relative sizes and locations of each region may differ upon material and welding parameters. The nugget, slightly larger than the pin, experiences the highest temperatures and most sever strains. The TMAZ, also affected by thermal cycles and strains, surrounds the nugget. Compared to the nugget, however, peak temperatures are lower, times at temperature are shorter, and strains are lower[3,4,6,11,12]. The HAZ surrounds the TMAZ and experiences no deformation but is exposed to mild thermal cycles[3]. As mentioned, a variety of materials have been successfully joined via FSW. As will be shown, the developing microstructures are largely dependent on the material and on the weld parameters used.

2.1.4 Aluminum and Friction Stir Welding

A number of materials have been joined by FSW – aluminum, lead, zinc, magnesium, copper and some steels[2]. Aluminum, however, is the most commonly and successfully FS welded material. The high driving force to find an alternative joining process for aluminum alloys stemmed from the poor structural integrity of aluminum arc welds. In heat-treatable aluminum alloys, the desirable properties obtained by precipitation hardening are essentially destroyed as a result of severe thermal cycles created during welding. FSW provided an acceptable and feasible alternative to arc welding. Before the process could be industrialized, however, extensive characterization of the resulting microstructures and material flow patterns was required to understand and optimize the FSW process. Since FSW is relatively new, many studies have been dedicated to understanding the resulting microstructures of aluminum alloys including the 1xxx, 2xxx, 5xxx, 6xxx, and 7xxx series[3, 5, 6-8, 11-13].

The 2xxx series is a class of aluminum alloys with copper as the major alloying element. These alloys have superior properties as a result of their precipitation hardening characteristics and are a popular choice for aerospace applications such as fuselage panels, tanks, and small structural parts[14,15]. The change in the microstructure as a function of distance was analyzed in a 2024-T3 FS weld using a rotational speed of 360 rpm and a translational speed of 3.3 mm/sec. The nominal composition of a 2024 Al alloy is Al-(3.8-4.9)Cu-(0.3-0.9)Mn-(1.2-1.8)Mg (by wt%) with trace amounts of other elements such as silicon, iron, and chromium. The T3 temper consists of solution heat-treating and then cold working. The as-received material consisted of elongated grains

from rolling operations. Figure 2-5A shows the microstructural transition occurring at increasing distances from the weld centerline. Positions 1 and 2, both in the nugget, have refined structures consisting of fine equiaxed grains. These microstructures are a result of dynamic recrystallization caused by the intense strain and temperatures in the nugget. Position 3 corresponds approximately to the edge of the pin and reveals the microstructural change from the refined nugget to the coarse grained structure of the HAZ. The change in microstructure results from the decreasing strains and temperatures with increasing distance from the weld center. It should be noted that the grains at position 1 and 2 may be larger than grains near the top left in the image of position 3. Closer to the weld centerline (positions 1 and 2) , the grain size may be larger because of greater static grain growth at the higher temperatures achieved here. Position 4 represents the HAZ and consists of coarsened grains but no effect of strain is seen. At position 5, approximately 4.5 mm from the shoulder edge, there is no evidence of heating or deformation – the microstructure is that of the unaffected base metal.

In addition, the grain size was shown to vary throughout the plate thickness with larger grains at the crown (surface side at which the shoulder makes contact) and smaller grains towards the weld root (surface side that is furthest from the tool shoulder), Figure 2-5B. Extra heating is provided by the tool shoulder rotating at the plate surface which allows for greater static grain growth. In addition, because conduction is the sole means of cooling this region, it may have slower cooling rates than material below. A banding structure was seen in the nugget and is commonly referred to as onion rings. The banding was shown to be related to variations in the distribution of second phase

particles, Figure 2-6. The appearance of the bands is directly related to material flow and the welding parameters, mainly the tool translation speed[13].

Li et al[5] employed LOM and TEM techniques to analyze the effect of weld speed on the microstructure of a 2024-T4 FS weld produced using rotational speeds ranging from 400-1200 rpm and a constant translational rate of 1 mm/sec. The T4 temper refers to solution heat-treating and then naturally aging to a stable condition. The unaffected base metal consists of large grains which are slightly elongated, Figure 2-7A, while the nugget consisted of small equiaxed grains, Figure 2-7B. TEM images reveal that the large grains of the base metal have a high dislocation density, Figure 2-7C. The dislocation density of the nugget grains, however, is low, Figure 2-7D. The decrease in dislocation density of these grains is a result of recrystallization during FSW. The grain size was shown to increase with increasing rotational speed. Figures 2-8A and B show the nugget microstructures of welds produced at 400 and 800 rpm, respectively. The dislocation densities in the nugget of welds produced at 400 and 800 rpm are seen in Figures 2-8C and D, respectively. Both structures show dislocations but the 800 rpm weld, Figure 2-8D, contains dislocation loops and spirals. Increased magnifications of the spirals in the 800 rpm structure are seen in Figures 2-9A and B. The occurrence of dislocation spirals indicates a climb component in their creation during welding and heat generation[5].

Litynska et al[16] analyzed the precipitate structure found within a 2xxx Al alloy FS weld produced using a rotational speed of 850 rpm and translational speed of 1.25 mm/sec. The nominal composition of this alloy was Al-6.0Cu-0.75Mg-0.65Ag-0.19Mn-

0.36Zr (by wt%). In the base metal, the grains were approximately 20 μm in size and the Ω phase (Al_2Cu) was the dominant strengthening precipitate, Figure 2-10A. This phase forms as hexagonal-shaped plates on the {111} plane of the matrix and ranged from 20-80 nm in size. There were also small amounts of Θ' (Al_2Cu) and S' (Al_2CuMg) precipitates present. The grain size in the nugget ranged between 3 – 5 μm, Figure 2-10B. The temperatures reached in the nugget during welding caused dissolution of the Ω, Θ', and S' phases and resulted in a homogenous distribution of Al_3Zr precipitates and elliptical $Al_{20}Cu_2Mn_3$ dispersoids. The HAZ – different from the nugget and the base metal – contained Θ (Al_2Cu), σ ($Al_5Cu_6Mg_2$), Ω (Al_2Cu), Θ' (Al_2Cu) and S' (Al_2CuMg) precipitates, Figure 2-10C. The temperatures reached in the HAZ caused coarsening of the Ω, Θ', and S' precipitates. Heating also caused the density of Ω plates to decrease and the density of the Θ' and S' precipitates to increase in this region[16].

Charit et al.[17] investigated the orientation relationship between grains within the nugget of a FS weld using orientation imaging microscopy (OIM). A FS weld of a 2042-T4 alloy produced with a rotational speed of 300 rpm and translational speed of 0.42 mm/sec was analyzed. The base metal consisted of elongated grains in the direction of rolling, Figure 2-11A, while the nugget had a refined structure of equiaxed grains, Figure 2-11B. The second phase particles in the nugget can be seen using TEM, Figure 2-12A. Orientation Imaging Microscopy (OIM), reveals that over 95% of the grain boundaries are high angle grain boundaries, Figure 2-12B. The high angle grain boundaries are a characteristic of a completely recrystallized structure[17].

The 1xxx series alloys are "pure" aluminum alloys such that the concentration of aluminum is greater than 99%. Unlike the 2xxx series, the 1xxx series is not a precipitation hardened class of alloys. A FS weld of a cold-rolled 1050 Al alloy was produced using a constant translational speed of 1.55 mm/sec and rotational speeds of 560, 980, and 1840 rpm. All welds produced had a u-shape, much like other FS welds, with a clear difference between the weld zone and the base metal. Compared to the retreating side, the advancing side of the weld showed a more abrupt change between the base metal and weld zone, Figure 2-13A. The difference between the advancing and retreating sides relates to the differences in material flow. The base metal consisted of elongated grains along the rolling direction, Figure 2-13B. Even though the 1050 Al alloy is essentially pure aluminum, some second phase particles are present here. The nugget consisted of very fine recrystallized grains, Figure 2-13C. Second phase particles here were much smaller and had a more homogeneous distribution that in the base metal. TEM analysis showed effects of rotational speed and provided further details of the nugget structure. Consistent with the 2024 Al alloy, higher rotational speeds led to higher weld temperatures and greater static grain growth. At 560 rpm, grains were on the sub-micron size of about 0.5 μm, Figure 2-14A. At 980 rpm, grains were 1-2 μm, 2-14B, while at 1840 rpm, grains were 3-4μm, Figure 2-14C[18].

The weld microstructure of an equal-channel angular (ECA) pressed 1050 Al alloy was analyzed by Sato et al[19]. ECA pressing is a very high-strain deformation process used to create an extremely fine grained microstructure. The FS welds were produced with a translational speed of 5.9 mm/s but no tool rotational speed was

provided. The as-received alloy consisted of small grains having a substructure with a cell size 0.58 μm and a high dislocation density, Figure 2-15A. This structure is a result of recovery during ECA pressing. The weld zone also had a fine structure, but consisted of equiaxed grains with an average size of 0.61 μm. It should be noted that the plate thickness in this case was 1 mm, much thinner than plates used for most FSW. The extremely small grain size suggests that cooling was fast enough to prevent the static grain growth which results in the coarser-grained nuggets seen in FS welds on thicker plates. As seen from the TEM image, Figure 2-15B, grains in the nugget had a low dislocation density. The TMAZ consists of a cellular structure similar to the base metal, a result of recovery, Figure 2-15C. Cells are larger and dislocation density is lower in the TMAZ when compared to the ECA pressed base metal because the temperatures during FSW are higher than that achieved during ECA pressing. It should be noted that the cell size in the TMAZ is approximately the grain size in the weld nugget. In summary, the higher temperatures in the nugget allow for both recovery and recrystallization while temperatures of the TMAZ were sufficient enough to allow for only recovery[19].

Hardness traces across the weld zone reflect changes in the microstructure. Therefore, heat-treatable aluminum alloys, having similar microstructures, show similar hardness trends. Figure 2-16A shows hardness across the weld zone as a function of distance from the centerline of a 2024-T3 aluminum alloy. In Figure 2-16A, the minimum data points falling just outside the dashed vertical lines represent the HAZ. The nugget and TMAZ, within the dashed lines, is harder than the HAZ but still softer than the base metal due to the dissolution of precipitates[7,12]. Although, properties are still

sacrificed in FSW, the decrease in hardness is less severe than experienced during arc welding[4]. As described above, the microstructure of a work-hardened aluminum is different than a precipitation hardened alloy. In turn, the hardness traces across the weld zone are also different, Figure 2-16B. In the case of a 1100 Al alloy, the hardness of the weld zone, falling between the two arrows, is somewhat superior to the base metal as a result of grain refinement[20]. Unlike the 2xxx series, there is no decrease in hardness due to precipitation affects.

As can be seen from the above results, characteristics of developing microstructural zones – the nugget, the TMAZ, and the HAZ – are dependent on the alloy composition and the weld parameters.

2.1.5 Friction Stir welding of Steel

2.1.5.1 Advantages

Recently, there has been increasing interest in FSW of harder materials like stainless steel. Although most steels are readily weldable using standard techniques, FSW offers a number of advantages over arc welding. In arc welding, a thorough cleaning of the surface is usually required – this is not the case for FSW. Due to the complex material transport, surface contamination is eventually expelled from plates in flash. Also, because FSW is an autogenous process requiring neither a flux nor shielding gas, the potential for composition changes is very low[21]. A number of benefits such as lower distortion, lower shrinkage, and no porosity are a direct result of the lower operating temperatures of FSW[22]. Also, similar to aluminum alloys, the lower thermal

cycles of FSW should result in superior weld properties compared to arc welds[4]. For stainless steels, there are two advantages that make FSW particularly desirable. First, hexavalent chromium, a carcinogenic gas generated in arc welding, is absent in FSW[4]. Second, and most importantly, solidification defects commonly seen in arc welding such as solidification cracking and microsegregation should be avoided[21].

2.1.5.2 Difficulties

Despite its possible advantages, progress in FSW of steel has been slow and greatly lags the progress made in FSW of aluminum alloys. As stated, the poor weldability of many aluminum alloys has been the driving force to understand FSW and make it a practical joining process. Because arc welding produces acceptable welds on stainless steel, there has been little effort to find alternative welding processes. Also, in comparison to aluminum, stainless steel has a much higher flow stress and lower thermal diffusivity, creating a harsher tool environment and causing accelerated tool wear[23]. Tool wear limits process productivity and may also result in weld contamination. With proper tool design and better selection of tool material, however, wear can be minimized[24].

2.1.5.3 Microstructures of FS Welded Steels

2.1.5.3.1 Type 304 Stainless Steel

Although several studies of 304 SS FS welds have been performed[23-26], only one such study provides a thorough characterization of the resulting microstructure[25]. Figure

2-17A, shows that the base metal consists of coarse austenite grains about 20 μm in size with small particles of ferrite. The austenite grains had a low dislocation density, Figure 2-17B. Similar to the aluminum alloys discussed, the nugget had a refined microstructure of equiaxed grains, Figure 2-17C. The average grain size was approximately 14 μm. The TEM image of the nugget shows a moderate amount of dislocations present within these grains, Figure 2-17D. This microstructure is indicative of recovery and recrystallization. The TMAZ consisted of slightly irregular austenite grains, Figure 2-17E. The TEM image, Figure 2-17F, reveals a subgrain structure within the grains of the TMAZ. The presence of subgrains reveals recovery in the TMAZ.

A banding phenomenon was seen at the lower edge of the advancing side of the weld zone, Figure 2-18A. Two different morphologies of the banding are labeled A and B in this figure. Figure 2-18B is a high magnification image of the banding in the region labeled A. As seen, the banding consists of a streaky second phase within an austenite matrix. The banding in region B, Figure 2-18C, had a somewhat lamellar structure consisting of alternating layers of austenite and high density bands of second phase particles. The banding was also analyzed using OIM, TEM, and EDS. The OIM map of region A, Figure 2-19A, reveals 500-1000 nm particles within the grain boundaries. The TEM image of this region is seen in Figure 2-19B. A quantitative analysis of the EDS spectrum of particles in region A, Figure 2-19C, indicates the second phase had a composition of 54.6 Cr, 43.1 Fe and 1.0 Ni (by wt%). The 304SS base metal had a nominal composition of 18.1 Cr, 8.56 Ni, 0.59Si, 1.08 Mn and a balance of Fe (by wt%). The OIM analysis of region B, Figure 2-20A, shows smaller grains in comparison to

region A, Figure 2-19A. The particle size, determined using TEM images ranged, from 200-400 nm, Figure 2-20B. A quantitative analysis of the EDS spectrum of this phase, Figure 2-20C, indicates a composition of 33.8 Cr, 60.6 Fe, and 5.0 Ni (by wt%). Again, the composition of the second phase is different than the base metal. The compositions of the second phases in region A and B suggest that they are carbides or sigma phase. A high magnification TEM image of the second phase particle in region A is seen in Figure 2-21A. The particle contains many staking faults with a preferential orientation. Analysis of the electron diffraction pattern, Figure 2-21B, revealed that the particle is sigma phase. Sigma likely formed as a result of a solid-state transformation induced by the highest temperatures experienced only at the advancing side of the FS weld. As the microstructure heats, austenite transforms to δ-ferrite, which upon cooling decomposes to sigma and austenite. Although decomposition to sigma normally requires long times, the transformation has been shown to be accelerated by high strain and recrystallization, both of which are present in FS welds[25].

The microstructural analysis of 304 SS FS welds by Posada et al.[24] was brief. Onion rings, consisting of alternating layers of ferrite and austenite were noted in the nugget. No banding was mentioned, however, suggesting no sigma formation in this particular FS weld[24].

2.1.5.3.2 AL-6XN

At present, Reynolds et al[27] has the sole investigation of a super austenitic stainless steel FS weld. In this case, the material welded was AL-6XN. The base metal

consisted of large equiaxed austenite grains about 80μm in size, Figure 2-22A. Also seen in this figure is centerline sigma which is a product created during plate fabrication. Although there was no mention of onion rings in the AL-6XN FS weld, the nugget consisted of refined grains. The HAZ, surrounding the nugget, had a microstructure of large austenite grains with some type of nucleation phenomenon at the grain boundaries. The microstructure of both the nugget and the HAZ are seen in Figure 2-22B. In this figure, the nugget is in the upper left region and the HAZ is towards the bottom. It was suggested that the nucleated grains at grain boundaries were either the sigma phase or new, recrystallized austenite grains[27]. No further research, however, was dedicated to identify this phase.

2.2 Passivity

Almost all metals will react with their environment to form a surface layer of a stable compound, often an oxide. For example, aluminum alloys form a very thin and stable aluminum oxide scale. The characteristics of this layer depend on the metal composition, the aggressive environment, and the temperature of the system. If the layer acts as a protective coating, preventing further reaction between the metal and the aggressive environment, it is said to be a *passive* layer. Many high performance alloys, such as stainless steels, owe their superior corrosion resistance to passive layer formation.

Early experiments yielded results indicating that passivation behavior may be different depending on the corrosion system. There are two definitions used today to describe passivity:

Definition 1 – A metal is passive if it undergoes anodic polarization and thus resists further corrosion[28].

Definition 2 – A metal is passive if, thermodynamically, corrosion is a stable reaction but the metal does not corrode[28].

With respect to the electrochemistry, Definition 1 refers to passivation resulting in low corrosion rates at noble electrochemical potentials. Metals such as nickel, chromium, molybdenum, titanium, and stainless steels exhibit this type of passivation. Definition 2, however, refers to systems with low corrosion rates while at active potentials. Lead in sulfuric acid and magnesium in water are two examples of systems that experience passivity according to definition 2[29].

2.2.1 Formation of the Passive Layer

There are many theories to explain the mechanisms responsible for passive layer formation and growth. Cabrera and Mott developed the *oxidation theory* – one of the earliest theories of passive layer formation. This theory suggests growth via ionic transport driven by the high electric field across the passive film[30]. A number of more recent theories such as the *Hopping model*, the *induced space charge model,* and *point defect model* are simply modified versions of the original oxidation theory. Other theories do not assume an electrical field is the driving force for ionic transport. For example, the *adsorption theory* attributes passivity to adsorption of a thin layer of oxygen at the metal surface. The thin oxygen layer prevents adsorption of aggressive ions, which effectively slows the corrosion rate[31]. Passive layer growth, in the *phase exchange*

model, proposed by Sato and Cohen, occurs by the exchange of oxygen atoms and metal ions at the metal-electrolyte interface[32].

2.2.2 Characteristics of Passive Layers

Five characteristics controlling the behavior of the passive layer are thickness, chemical composition, structure, defects, and electronic properties. These characteristics are inherently related to one another. With respect to thickness, there are two types of passive layers. Two-dimensional films (described by the adsorption theory) are very thin, consisting of a monolayer or less of adsorbed oxygen. As mentioned, this type of layer prevents corrosion by retarding corrosion rates at the metal-electrolyte interface. Three-dimensional films are much thicker and prevent further dissolution of metal by acting as a diffusion barrier against aggressive species. Passive film thickness may dictate susceptibility to breakdown, the breakdown mechanism, and the repassivation capabilities. The passive layer may have many stable compositions and is controlled by the metal composition and the aggressive environment. Passive films on iron and iron alloys have been shown to exist as at least six different compounds. Not only can the composition of the passive layer control breakdown, the breakdown process may alter the composition of the layer. Three important distinctions relating to composition are as follows: thickness, presence of hydrogen, and presence of alloying elements. Passive film structure is closely related to composition[32]. McBee and Kruger[33] showed that the structure of the passive film, whether it tends toward a crystalline or non-crystalline glassy structure, plays a role in breakdown. Also affecting the passive layer and its

breakdown are the defects inherently present in all materials. For example, cation vacancy concentration has been shown to affect frequency distributions of the breakdown parameters, critical breakdown potential, and induction time[34]. In addition, because passive film formation and breakdown inherently involve the transport of charged species, the electronic properties of these films will have some influence[32].

2.2.3 Thermodynamics

Conditions of passivity, and corrosion in general, can be described in terms of thermodynamics and kinetics. The thermodynamics of corrosion is based on the energy associated with chemical reactions. The electromotive force (EMF) series is a list of half reactions and their standard electrode potentials in reference to the standard hydrogen electrode, Figure 2-23. The magnitude and sign of the potential represents driving force for a reaction to occur. A large negative sign indicates that corrosion is very likely while a large positive sign indicates corrosion is unlikely. Accordingly, the negative end of the EMF series is referred to as *active* and the positive end of the EMF series is referred to as *noble.* Although the EMF series can be useful, its capabilities are limited because the data provided is very specific and concerns reactions at standard conditions, an event which rarely occurs[35].

Pourbaix diagrams, plots of potential versus pH, are a much more applicable form of thermodynamic data. As seen in Figure 2-24A, the Pourbaix diagram for iron in water, regions are labeled with stable phases for the given potential and pH range. Depending on what phase is stable, the Pourbaix diagram dictates whether a metal will exhibit

passivity, immunity, or corrosion. For example, compare Figures 2-24A and B. As seen, iron is immune if the reduced form, Fe, is stable but will corrode when its soluble oxidized ions, Fe^{3+} or $HFeO_2^-$, are stable. As defined previously, passivation occurs when a stable oxide forms on the metal surface to protect the underlying metal[36]. As seen in 24A and B, $Fe(OH)_3$ is the stable oxide in the passive region.

Boundaries of the various regions on Pourbaix diagrams are obtained by evaluating the general form of the Nerst Equation,

$$E = E^o + (2.3RT/nF)\ \log[a_{oxid}]/[a_{red}]$$

where
E = measured potential
E^o = equilibrium potential
R = gas constant
T = temperature
n = number electrons transferred
F = Faraday's constant
a_{oxid} = activity of the oxidation reaction
a_{red} = activity of the reduction reaction,

for the possible electrochemical and chemical reactions of a given system[35]. It is important to note that thermodynamic data indicates only whether a given reaction is possible, it does not indicate rate of the reaction.

2.2.4 Kinetics

To describe the kinetics or reaction rates of passivation, polarization curves are one of the standard tools employed. Polarization curves are plots of electrochemical potential, E, versus the current density, *i*. The electrochemical potential refers to the cell potential referenced to the standard hydrogen electrode and, as stated previously, is a

measure of driving force. Current density is defined as the current per unit of surface area of the exposed metal and is related to the corrosion rate via the following equation

$$\mathbf{r} = i/\mathbf{nF}$$

where
r = reaction rate
i = corrosion rate
n = number of electrons transferred
F = Faraday's constant[37].

Stainless steels and other metals exhibiting Type I passivity have a distinct electrochemical behavior referred to as an active-passive transition that is portrayed by a distinct polarization curve. The anodic or oxidation polarization curves for such metals have, in general, an "s" shape as seen in Figure 2-25[37].

Similar to Pourbaix diagrams, the behavior of a metal in a particular environment may be determined via polarization curves. Based on potential and current density, three distinct regions are often identified on polarization curves: the active, the passive, and the transpassive regions, Figure 2-25. In the active region, typically at lower potentials, corrosion (or dissolution) rates increase with increasing potential. As the potential is increased to the passive potential, E_{PP}, corrosion rates drop to the passive current density, i_{pas}. Corrosion rates are lower in this region as a result of the formation of a stable passive layer. Current density in the passive region remains low and constant with further increases in the potential[37]. Eventually, at the critical potential, E_C, the passive film is no longer stable and breakdown occurs[38]. This is referred to as the transpassive region where corrosion is likely to occur in some localized form such as pitting[37].

The behavior of a metal in a specific environment can be assessed by plotting the oxidation polarization curve of the metal with the reduction polarization curve for the environment. Figure 2-26 shows a series of generic reduction polarization curves intersecting an oxidation polarization curve. According to the mixed potential theory, the intersection of polarization curves occurs at a potential in which the rate of the oxidation and reduction reactions are equal. The region in which the curves intersect – active, passive, transpassive – determines behavior of the metal. For example, corrosion will occur for reduction lines 1 and 2, while the system will be passive for reduction lines 4-6. In the case of lines 7 and 8, localized corrosion is likely to occur. In some cases, as shown by line 3, however, polarization curves may intersect multiple times. Intersection at point C occurs in the active region while intersection at C' occurs in the passive region. Therefore, both corrosion and passivation are stable for this particular system. Intersection X on line 3 occurs in a region of increasing potential and decreasing current on the oxidation polarization curve. This is not a stable condition and will not likely occur in a system[30,37].

As evident from the previous discussion, passivity is a complex phenomenon. Not just one but several theories describe passive layer formation and growth. Also, there is no standard passive layer. The passive layer that forms depends on the sample and the environment. Tools such as Pourbaix diagrams and polarization curves are used to describe the thermodynamics and the kinetics of passivity and help to quantify aspects of this phenomenon.

2.3 Corrosion

2.3.1 Pitting Corrosion

Almost all metals experience corrosion, a deterioration of structure and properties, upon reaction with the environment. The yearly cost of corrosion in today's society is substantial, totaling billions of dollars annually. Although corrosion may appear in any of several forms, one of the most insidious forms is pitting corrosion. Pitting is generally defined as a localized attack of a metal as a result of passive layer breakdown in an aggressive environment[39].

One reason pitting is so destructive is that pit detection is difficult – pits are typically small and often concealed by a "cap" of corrosion products leaching from within the pit. Also, pit morphology may be such that surface attack is minimal but a large undetectable volume of metal beneath the surface has been consumed by corrosion. This type of pit morphology is referred to as undercutting. Figure 2-27, a cross-section of a stainless steel tube wall shows sever undercutting. The difficulty in monitoring pitting severity also contributes to the destructive nature of this type of corrosion. Tracking total weight loss of a structure is used to monitor some forms of corrosion. This method, however, is unacceptable to evaluate the severity of pitting. Since pitting is localized, a few deep pits may lead to catastrophic failure without a significant weight loss. Some techniques used to evaluate pitting are measuring pit density, total surface area of pits, and or maximum pit depth. These evaluation methods are very tedious and their capability to properly gauge the severity of pitting is questionable. Out of these methods,

pit depth measurements seem to be preferred. ASTM Standard G46-76 outlines the procedure for pit depth measurements[40].

2.3.2 Pit Initiation

Four conditions are required for pitting: 1) the critical potential must be exceeded, 2) an aggressive ion or species must be present, 3) an induction period prior to pit formation, and 4) the breakdown of the passive film at a localized site[41]. Pit initiation, or passive layer breakdown, due to its random nature and the short time required, has remained one of the least understood stages of pitting. Three popular theories explaining passive layer breakdown are the *penetration mechanism*, the *film breaking mechanism*, and the *adsorption mechanism*[39]. In the *penetration mechanism*, Figure 2-28A, aggressive ions diffuse through the passive layer where they eventually react with the metal surface[42]. One penetration based model stems from the point defect model used to describe passive layer formation. In the model, cation vacancies, created by adsorption of anions, diffuse towards the metal-oxide interface essentially creating a flux of cations towards the metal-electrolyte interface. Accumulation of vacancies at the metal-oxide interface can result if the diffusion of vacancies through the passive layer is greater than diffusion of vacancies into the metal. Eventually, accumulating vacancies form voids at the interface which create mechanical stresses that can lead to passive layer breakdown[43].

Adsorption mechanisms of pit initiation, Figure 2-28B, assume the passive layer consists of a monolayer or thinner of adsorbed oxygen. This mechanism focuses on the competition between the adsorption of hydroxyl ions or chloride ions at the film and

electrolyte interface. As aggressive ions are adsorbed, the passive layer thins and the local field strength increases, creating a stronger driving force for ionic transport. The field is created by the difference in potentials at the interface of the electrolyte and the passive layer and the interface of the passive layer and the metal substrate. Higher driving forces ease ionic diffusion through the passive film which, in turn, further increases the field strength. This cycle continues until the passive layer thins to the point of breakdown[39].

According to the *film-breaking mechanism*, breakdown is unavoidable due to mechanical stresses in the passive layer, Figure 2-28C. Surface defects act as natural stress concentrators and serve as prime initiation sites for passive layer breakdown[44,45]. In non-aggressive environments, metals have the ability to quickly heal, or repassivate, to prevent further attack. In aggressive environments, however, metals lose ability to repassivate, allowing for the continued attack of the exposed metal[39].

2.3.3 Pit Growth

Although a pit may initiate, its continued growth is not guaranteed. Pit growth occurs by an auto-catalytic reaction, creating a unique but unfortunate condition which promotes and accelerates corrosion within the pit (or the anode). Dissolution within the pit results in an accumulation of M^+ ions and a local positive charge that attracts aggressive Cl^- ions. Hydrogen, created by hydrolysis reactions, also accumulates near the pit mouth. Both Cl^- and H^+ ions tend to enhance the pitting process. The material

surrounding the pit remains unattacked and acts as the cathode – a site for oxygen reduction[46].

Once initiated, certain conditions will promote pit stability or growth. As with pit initiation, there are several theories explaining pit growth. In one theory, pit growth depends on formation of a salt film at the bottom of the pit. The film is an accumulation of corrosion products created by anodic reactions within the pit. The film controls ionic transport between the electrolyte and the metal and thus controls pit growth[41].

Some theories explain pit stability in relation to potential drops and local pH. Within a pit, there exists a potential drop (compared to the bulk electrolyte) that is a function of local current density, pit radius, and specific conductivity. The potential drop, ΔU, is defined by the following equation,

$$\Delta U = a i_{cp} r/\kappa$$

where
a = geometric factor
i_{cp} = local current density
r = pit radius
κ = specific conductivity.

Depending on the magnitude of the drop, the potential within the pit may be shifted into the active range of the polarization curve and corrosion will proceed[43].

The concentration of ions in the pit electrolyte is the controlling factor in other theories describing pit growth. In such theories, a minimum concentration of anions, C_{min}, is required for stable pit growth. This threshold for pit stability is defined by the following equation,

$$C_{min} = aV_m i_{c,p}\delta/DFV$$

where
C_{min} = minimum concentration of anions
δ = salt film thickness
c = concentration minimum
i = current density
a = geometric factor
D = diffusion constant
V = volume[43].

2.3.4 Pit Repassivation

Once a pit initiates, it is possible for the pit to heal or repassivate. The repassivation potential (E_{RP}), the potential below which pits can repassivate, lies between the passive potential, E_{PP}, and the critical pitting potential, E_C. If the corrosion potential is noble to E_{RP} but is active with respect to the E_C, existing pits will continue to grow but new pits will not form. In stainless steels, the potential of the electrolyte underneath a protective corrosion cap may be altered which allows metastable pit growth. If the film ruptures, the pit electrolyte and the bulk electrolyte will mix and repassivation occurs. If the film remains intact or the electrolyte potential is above the E_C, the pit continues to grow in a stable manner. Above the E_C, the passive film is unnecessary due to the formation of a salt film that forms at the base of the pit. The potential drop across the salt film stabilizes further dissolution[41].

2.3.5 Severity of Pitting

2.3.5.1 Solution Composition

Solution composition is just one of many factors affecting pitting. Aqueous solutions containing halide ions, particularly chlorides, tend to promote pitting[46]. The specific role of chloride ions in pitting has been studied extensively but is still unclear. Some evidence suggests that chloride ions initiate passive film breakdown[47]. As mentioned, the adsorption theory involves competition between ions to bond at the metal surface. Unlike oxygen, when Cl^- bonds to the metal surface, the dissolution reaction is favored[48]. Other theories suggest that Cl^- simply prevents repassivation only after passive film breakdown occurs [47]. With respect to the marine environment, dissolved ions of NaCl do not significantly alter the pH of the solution. The corrosion rate increases with increasing concentration until approximately 3% NaCl, Figure 2-29A. The increasing number of ions results in higher conductivity and lower polarization with higher corrosion currents between adjoining anodes and cathodes. Increases in NaCl concentration beyond 3%, leads to decreasing corrosion rates because of the decreased solubility of oxygen[49].

As inferred above, dissolved oxygen also plays a large role in corrosion. At ambient temperatures, a stable protective passive film forms when no oxygen is present. As seen in Figure 2-29B, the corrosion rate increases linearly with the concentration of dissolved oxygen. Factors affecting the dissolved oxygen, in turn, alter corrosion rates. For example, as stated above, as the concentration of NaCl increases, the solubility of oxygen decreases[49]. Conversely, some ionic species in a solution improve pitting

resistance. For example, the presence of sulfates, hydroxides, chromates, molybdates in a solution will improve the corrosion resistance of stainless steels. Such species are believed to aid in corrosion resistance by either interfering with aggressive ion adsorption at the metal surface or by forming a more protective passive film[50].

The pH of the solution, as seen in Pourbaix diagrams, influences corrosive behavior. Figure 2-29C shows the effect of pH on corrosion of iron in aerated water. As the pH changes, the cathodic reaction also changes. In acidic solutions, below pH 4, oxygen is reduced according to the following equation

$$O_2 + 4H^+ + 4e^- \rightarrow 2H_2O.$$

In these acidic solutions, the oxide is soluble and corrosion rates increase due to the availability of H^+ and the accessibility of dissolved oxygen. In the pH range of 4-10, a porous layer of ferrous oxide forms on the surface. At this pH range, the diffusion rate of dissolved oxygen through this layer controls the corrosion rate. Reduction of oxygen, in this case, occurs according to the following equation

$$O_2 + 2H_2O + 4e^- \rightarrow 4OH^-.$$

In basic solutions, pH above 10, a passive film of ferric oxide forms and corrosion rates are low[49].

2.3.5.2 Solution Velocity

Depending on the rate controlling mechanism of corrosion, the velocity of the aggressive solution with respect to the metal surface may influence pitting. Activation polarized systems show no dependence on solution velocity but in a concentration

polarized system solution velocity plays a major role. For these systems, fast solution velocities limit the concentration of aggressive species and corrosion proceeds slowly. As solution velocity decreases, aggressive ions can accumulate at the surface. Since the corrosion rate of this system is limited only when there are few aggressive ions present, corrosion will occur at the fastest rate possible[37].

2.3.5.3 Temperature

Temperature, as with other corrosion processes, affects pitting. For many metals, it is possible to establish a temperature below which pitting will not occur even at long exposure times. This temperature is referred to as the critical pitting temperature (CPT) and is used as a criterion to rank pitting resistance of metals. Generally, as temperature increases above the CPT, the severity of pitting also increases[39].

2.3.5.4 Surface Area

Surface area of exposed metal affects pitting in two ways. First, as the exposed area increases, pitting becomes more severe. Figure 2-30 shows that both pit depth and the probability of finding a pit increases with increasing surface area[40]. Second, the relative areas of the pit and the surrounding, unattacked material (the anode-to-cathode ratio) affect pitting. It was shown by Stern[51] that the corrosion rate is a maximum when the ratio approaches unity. Any deviation from this ratio results in decreasing corrosion

rates. Some, however, believe that both oxidation and reduction occur at the same regions and there is no critical ratio[52].

2.3.5.5 Metallurgical Variables

The composition of the metal itself plays a huge role in pitting behavior. Even seemingly small composition changes can have significant effects on pitting. In reference to steels, additions of chromium, nickel, nitrogen, and molybdenum enhance pitting resistance[46]. The effect of increasing molybdenum content is seen in 2-31A[53]. Increasing additions of sulfur, however, tend to degrade the pitting performance of steels. It has been shown that sulfides serve as preferential pit initiation sites[54]. T. Suter et al[55] used relatively new microelectrochemical testing to investigate the electrochemical behavior of MnS inclusions and their role in pit initiation. Figure 2-31B shows the results of potentiodynamic tests performed on steels of varying sulfur content. In this testing, a transient in the current density occurs as the result of increasing corrosion rates and more specifically the dissolution of the sulfide. From the test results, it can be seen that increasing sulfur content leads to more transients and thus a greater number of pit initiation events[55].

The microstructure of the alloy in question also plays a role in pitting. In the case of 18-8 stainless steel wrought products pitting occurred preferentially at edges[46]. Hananappel et al. [56] showed that 304 stainless steel cooking utensils showed a similar trend with preferential attack at highly deformed regions.

2.3.6 Galvanic Couples

While in a corrosive media, a metal has a unique corrosion behavior that corresponds to a unique corrosion potential. When two different metals in a corrosive environment are in contact, the differences in their corrosion potentials cause a net flow of electrons and one of the metals corrodes. In general, the metal with higher corrosion resistance is cathodically protected at the expense of the less corrosion resistant metal. Corrosion of the anode in the galvanic couple is typically more severe than if no couple was formed.

Similar to the EMF series, a Galvanic Series has been developed, Figure 2-32. Although similar, these lists are different in that the EMF series lists potentials that result from equilibrium conditions and the Galvanic Series lists corrosion potentials determined by polarization of two or more half-cell reactions to a common mixed potential. As the separation between two metals in the EMF series increases, the potential difference (or driving force for corrosion) increases. It should be noted that the Galvanic Series provides only an indication of what may happen when two metals are coupled[57].

2.3.7 Pitting Resistance and ASTM Standards

In many practical applications, it is necessary to understand the pitting behavior of a metal. There are two general types of tests used to determine the pitting behavior of a material – electrochemical and immersion techniques. Electrochemical methods, compare the measured corrosion potential, E_{CORR}, of a material with its passive potential, E_P. When E_{CORR} is greater than E_P, pitting occurs but when E_{CORR} is less than E_P, no

pitting occurs. As mentioned previously, under some circumstances pits may repassivate below the repassivation potential, E_{RP}. During electrochemical testing, E_{RP} can be determined by reversing the direction of the potential scan after E_C is reached[58]. ASTM Standard G150-99[59] outlines procedures used to determine the CPT of stainless steels using electrochemical testing.

Immersion techniques involve immersing material in an aggressive media, such as a concentrated ferric chloride ($FeCl_3$) solution, for determined length of time. The test environment can be altered either by changing the solution concentration or the testing temperature. Immersion tests are generally used to establish the CPT and rank the corrosion resistance of one material with respect to many others[58]. ASTM Standard G48-97[60] outlines procedures to evaluate the pitting and crevice corrosion of stainless steels and a number of related alloys when immersed in a strongly oxidizing environment of ferric chloride. Although performance of metals in the specific test conditions has been correlated to certain environments, no predictions about performance in non-chloride containing environments can be made[58].

2.4 Super Austenitic Stainless Steels

2.4.1 AL-6XN

Austenitic stainless steels are popular because of their superior properties, ease in fabrication and production, and general weldability. A class of steels known as super austenitic stainless steels (SASS) has been developed with the goal of achieving superior corrosion resistance. Typically, SASS contain high concentrations of chromium, nickel,

molybdenum, and nitrogen such that the concentration of iron is often less than 50%. In addition to enhanced corrosion resistance, mechanical properties of SASS are also superior to that of stainless steels[61].

AL-6XN, a SASS, was developed in 1984 and has a chemistry as specified by UNS N08367 of 20.0-22.0 Cr, 23.5-25.5 Ni, 6.0-7.0 Mo, 0.18-0.25 N (by wt %) and the balance of Fe, Table 2.1[62]. AL-6XN is an attractive material for the advanced double hull (ADH) design proposed by the U.S. Navy because, in addition to its superior mechanical properties and corrosion resistance, it is non-magnetic, readily available, and affordable. It should be noted that prior to AL-6XN, Allegheny Ludlum had developed AL-6X. The chemistry of AL-6X, as defined by UNS N08367, is 20.0-22.0 Cr, 23.5-25.5 Ni, 6.0-7.0 Mo (by wt.%) and the balance of Fe, Table 2.1. Although close in chemistry, corrosion properties of AL-6XN are superior to AL-6X as a result of the nitrogen additions. Nitrogen also has beneficial effects of increasing the strength without sacrificing ductility and suppresses the formation of intermetallic phases.

As mentioned previously, the corrosion resistance of SASS is superior to that of other alloys but they are not immune to corrosion. Attack of stainless steels, in general, is dominated by localized forms of corrosion such as pitting, crevice, intergranular and stress cracking corrosion. In a survey of corrosion failures of Dupont metallic piping from 1968 -1971, the majority of failures were attributed to some form of localized corrosive attack[50]. From the literature, it is apparent that corrosion of SASS also follows this trend. One of the major issues concerning localized corrosion is the high tendency to form intermetallic phases such as chi, sigma, and laves in high alloy stainless steels.

When such phases form by precipitation, a sensitized region around the intermetallic phase exists and is highly susceptible to corrosion[50,63,64].

Sedriks and Dudt[65] recently reviewed issues relating to corrosion behavior – namely pitting, crevice corrosion, and stress corrosion cracking – of several stainless steel alloys used for ship hulls, including AL-6XN. In pitting experiments, samples were immersed in natural seawater for extended times while potential was recorded to indicate the onset of pitting. Under examination, there was no evidence of attack of AL-6XN, suggesting that it is immune to pitting corrosion in natural seawater. Crevice corrosion tests were performed on AL-6X (the older and less corrosion resistant form of AL-6XN) in natural seawater in crevices created by natural fouling processes. Similar to pitting tests, there was no evidence of attack[65,66]. When crevices were formed by a thin layer of paint, however, crevice corrosion occurred[65,67]. To analyze the stress corrosion cracking behavior of AL-6XN, three different methods were used – ASTM G123, ASTM G26 and the Wick Test. AL-6XN failed only ASTM G36, immersion in a boiling magnesium chloride bath[65]. Apparent from these results, AL-6XN proves to have a substantially high corrosion resistance.

Romero et al[68] performed an electrochemical study of AL-6XN in brackish water. In a field evaluation, samples were immersed in brackish water for a period of 5 months and the open circuit potential (OCP) of the material was measured periodically. The variation of the OCP with time is used to compare corrosion behavior of materials. Figures 2-33A shows the OCP as a function of time for AL-6XN and, for comparison, Figure 2-33B shows the same results for a Cu-10% Ni alloy. Passive materials show

relatively constant potentials where as materials prone to pitting show erratic behavior with great fluctuations in potential. AL-6XN has a relatively stable potential, particularly during the end of testing, indicating it is not highly susceptible to pitting in this environment. In comparison, the OCP of the CU-Ni alloy is erratic, indicating localized corrosion[68].

Polarization resistance and cyclic polarization tests were also performed[68]. In both cases, tests were performed in chlorinated and non-chlorinated brackish water. Polarization resistance (PR) tests are used to determine the current density, an indicator of corrosion rate. In these tests, the polarization resistance is indirectly proportional to the corrosion rate. Figure 2-34, a measurement of 1/PR for AL-6XN and the Cu-10% Ni alloy, shows that AL-6XN has a very low corrosion rate while the Cu-10% Ni alloy has a substantially higher corrosion rate. Figures 2-35A and B show the results of the of cyclic polarization tests of AL-6XN and the Cu-10% Ni alloy, respectively. In Figure 2-35A, there is a positive hysteresis when the potential scan is reversed, indicating that there is no localized corrosion. The Cu-10% Ni alloy shows a negative hysteresis indicating that pitting did occur, Figure 2-35B. This reaffirms that AL-6XN has a superior pitting resistance in comparison to the copper-nickel alloy[68].

2.4.2 Arc Welding AL-6XN

Although AL-6XN and other stainless steels have superior corrosion properties, welding these alloys greatly degrades corrosion resistance. During weld solidification, molybdenum, responsible for increased corrosion resistance, tends to segregate to

interdendritic regions, resulting in molybdenum depleted dendrite cores that are highly susceptible to pitting[61,63,69-72].

The CPT, as defined previously, is the temperature below which pitting does not occur even at extended testing times. Information regarding AL-6XN autogenous welds is scarce but studies have been performed on AL-6X.

2.4.2.1 Autogenous Welds

As discussed previously, arc welding significantly degrades corrosion resistance of stainless steels[63,69,70,72,73]. A plot of CPT versus molybdenum content for a series of high alloy austenitic stainless steels including AL-6X is seen in Figure 2-36A. The CPT of unwelded AL-6X is approximately 67°C while autogenously welded AL-6X has a CPT of only about 33°C. The same trend is seen for the other steels represented in Figure 2-36A. The poor pitting resistance of autogenous welds is attributed to microsegregation of Mo and Cr to interdendritic regions and depletion of the dendrite cores[74].

2.4.2.2 Dissimilar Welds

Often, corrosion resistance of high alloy austenitic stainless steels arc welds is improved by using a high alloy filler metal[61,69,70]. When a Mo-rich filler metal is used, the minimum concentration of Mo at the dendrite cores is increased. Thus, even though microsegregation is not avoided, the increased Mo concentration should improve pitting

resistance. Garner et al.[75] showed the effect of using high alloy filler metals on 317L, 904L and 254 SMO stainless steels. The chemistry of these metals can be seen in Table 2.2. As seen in Figure 2-36A, the CPT of 317L base metal decreased from approximately 20°C to 10°C when autogenously welded. When 317L was welded with 317L-16, 309 Mo L-16, and other higher alloys filler metals, the CPT is preserved, Figure 2-36B. The compositions of these alloys are seen in Table 2.2 as well. For alloys 904L and 254 SMO, the trend is the same – using filler metals with a sufficient molybdenum content improves pitting resistance of arc welds[75].

Typically, in welds produced with over-alloyed filler metal, pitting corrosion occurs in the unmixed zone. The unmixed and the partially melted zone are regions between the fusion zone and the HAZ that have essentially the same composition of the base metal. The microstructure of these zones is the same as an autogenous weld (dendritic, with alloy depleted dendrite cores) leaving this region particularly sensitive to pitting[75]. Thus, the unmixed zone determines the pitting resistance in dissimilar welds. Figures 2-37A and B show the attack of the unmixed zone in AL-6XN dissimilar welds using IN 625 filler metal. The composition of In 625 is 20.0-23.0 Cr, 8.0-10.0, Mo, 7.0 Fe, 0.5 Cu and a balance of Ni. As seen in both images, pitting is concentrated at the weld interface[72].

Lundin et al.[76] researched the affect of the unmixed zone of AL-6XN autogenous and dissimilar arc welds. Dissimilar welds were made with an over-matched nickel-based filler metal to compensate for affects of microsegregation. As expected, ferric chloride immersion testing indicated the corrosion resistance of the unmixed zone was

inferior to the base metal for all welds. Interestingly, it was noted that the unmixed zone in dissimilar welds was superior to the fusion zone in autogenous welds due to less severe microsegregation in the unmixed zone.

In addition, pit growth was also investigated using immersion techniques. Figures 2-38A-C show pitting at 2, 4, and 30 minutes, respectively. At 2 minutes, just dendrite cores in the unmixed zone are attacked, Figure 2-38A. At 4 minutes, the interdendritic regions as well as the dendrite cores are attacked, Figure 2-38B. In addition, new pits have initiated. After 30 minutes, a large surface area was attacked and the small initiation sites have growth together to form a large pit. Also, it is evident that there is substantial sub-surface attack, Figure 2-38C. A transverse view of pitting at the weld interface is seen in Figure 2-38D. From these images, pit growth in the unmixed zone of dissimilar welds can be summarized as a series of steps. Pitting initiates at dendrite cores in the unmixed zone. Attack continues at the dendrite cores but eventually consumes the interdendritic regions. When the pit becomes large enough, attack occurs readily beneath the pit surface[76].

2.5 Corrosion and Friction Welds

Although, pitting corrosion resistance of arc welds is improved by using high-alloy filler metals, using an alternative joining method such as FSW may offer even higher pitting resistance. Although the information is somewhat limited, the pitting behavior of FS welds has been evaluated for several aluminum alloys and stainless steels FS welds.

2.5.1 Aluminum Alloy 5454

Frankel and Xia[77] examined pitting corrosion of aluminum alloys 5434-O and 5434-H34 via potentiodynamic polarization tests. The –O temper consists of a full anneal followed by slow cooling while the –H34 temper consists of a stabilizing heat-treat after strain hardening. The corrosion behavior of FS welds was compared to samples of unaffected metal and both autogenous and dissimilar GTA welds.

Microstructures of the different welds were typical of that produced by FSW and GTAW. FS welds contained a fine-grained nugget region and a HAZ. However, no formal distinction of the TMAZ was made. Pits initiated in the HAZ in both aluminum alloys. The GTA weld microstructure consisted of a dendritic weld zone and a HAZ of recrystallized grains. Pitting, in this case, initiated at the interdendritic regions of the weld zone. For Al 5454–O samples, the passive current densities, i_{pass}, of all welds were significantly higher compared to the base metals. The breakdown potential, E_P, of FS welds compared closely with the E_P of the base metal and both were noble to GTA welds. Similar trends were seen for Al 5454-H34 welds. Potentiodynamic data provided here suggests that FS welds offer superior corrosion resistance over GTA welds[77].

2.5.2 Aluminum Alloys 2024 and 2195

Corral et al.[78] evaluated corrosion behavior of FS welds of aluminum alloys 2024 and 2195 via static emersion tests and potentiodynamic methods. Static emersion tests of

both alloys revealed that base metal and the weld zone corroded in the same manner and possessed roughly equal amounts of corrosion product build-up. There was no evidence of preferential pitting – both base metal and weld zone were equally attacked. Potentiodynamic testing revealed similar corrosion behavior. Polarization curves of the base metal and weld zone yielded essentially the same current densities and corrosion potentials. Again, data suggests that FSW has no significant affect on corrosion properties[78].

2.5.3 Stainless Steel

Gooch et al.[79] investigated corrosion behavior of *friction welds* on high alloy austenitic stainless steels and compared the results to corrosion behavior of as-received plate material and arc welds. Five stainless steel alloys were tested, Table III. Friction welding, developed prior to FSW, also uses frictional heat to join metals. Due to the nature of the process, friction welding is limited to certain geometries such as bars and tubes. In the process, a rapidly rotating bar is forced against a fixed bar, resulting in large frictional forces and thus heat. The heat created causes formation of a plasticized region at the abutting surfaces and the bars become intimately joined. In potentiodynamic testing, the pitting potential (E_P) of friction welds was only slightly below the E_P of parent materials. The E_P of GTA welds, both autogenous and dissimilar metals, were significantly lower, Figure 2-39. Pit initiation sites were determined via potentiostatic methods. As-received material showed no distinct correlation between microstructure and pit initiation. In friction welds, pit initiation occurred at the weld line and at grain

boundaries of the HAZ. As expected, pit initiation in GTA welds occurred at Mo-depleted dendrite cores. In summary, friction welds offered a superior corrosion resistance to arc welds by avoiding microsegregation[79].

Although the pitting resistance of AL-6XN is superior in comparison to other metals, welding significantly degrades its corrosion properties. Improvements to the corrosion behavior of fusion welds have been achieved by using high alloy filler metals to compensate for the Mo-depleted dendrite cores in the weld affected regions. The new technique of FSW, however, may provide even better corrosion resistance.

Table 2. 1 *Compositions of AL-6XN and AL-6X.*

Material Trade Name	UNS Code	Cr wt %	Mo wt %	Fe wt %	Ni wt %	N wt%
AL-6XN	N08367	20.00-22.00	6.00-7.00	Balance	23.50-25.50	0.18-0.25
AL-6X	N08366	20.00-22.00	6.0-7.0	Balance	23.5-25.5	NA

Table 2. 2 *Chemistry of base metal and filler metals used to evaluate the corrosion resistance of stainless steel welds.*

Material Trade Name	Cr wt %	Ni wt %	Mn wt %	C wt %	N Wt%	Si wt%	P wt%	S wt%	Mo wt%	Fe wt%
317L	18	14	1.9	0.02	—	0.1	0.021	0.012	2.8	Bal
904L	20	25	1.8	0.02	—	0.4	0.025	0.004	4.2	Bal
SMO 254	20	18	0.5	0.02	0.21	0.5	0.015	0.002	6.1	Bal
317L-16	18	13	1.7	0.04	—	0.4	0.026	0.014	3.8	Bal
309 Mo	23	14	1.7	0.04	—	0.4	0.030	0.011	2.6	Bal

Table 2. 3 *High alloy stainless steels used for evaluation of corrosion behavior of friction welds.*

UNS deisgnation	Trade name
S30403	Type 304
S31000	Type 310
N08320	Hastelloy-20MOD
N08904	Type 904
S31254	SMO 254

*high alloy filler metals were used for GTAW

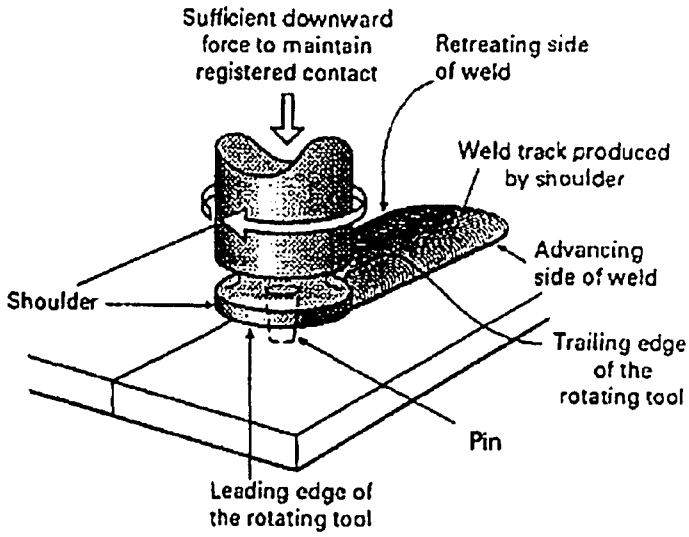

Fig. 2- 1 Illustration of the FSW process for butt joint welding[2].

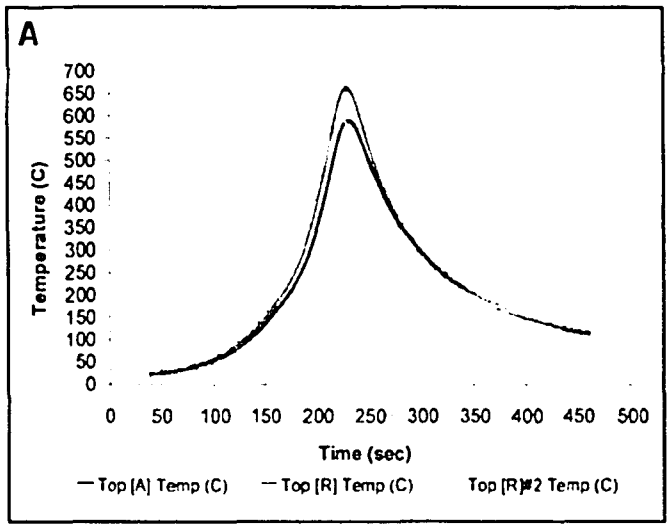

Fig. 2- 2 Temperature profile of AISI 1018 steel at 0.125 mm from the weld zone edge[4].

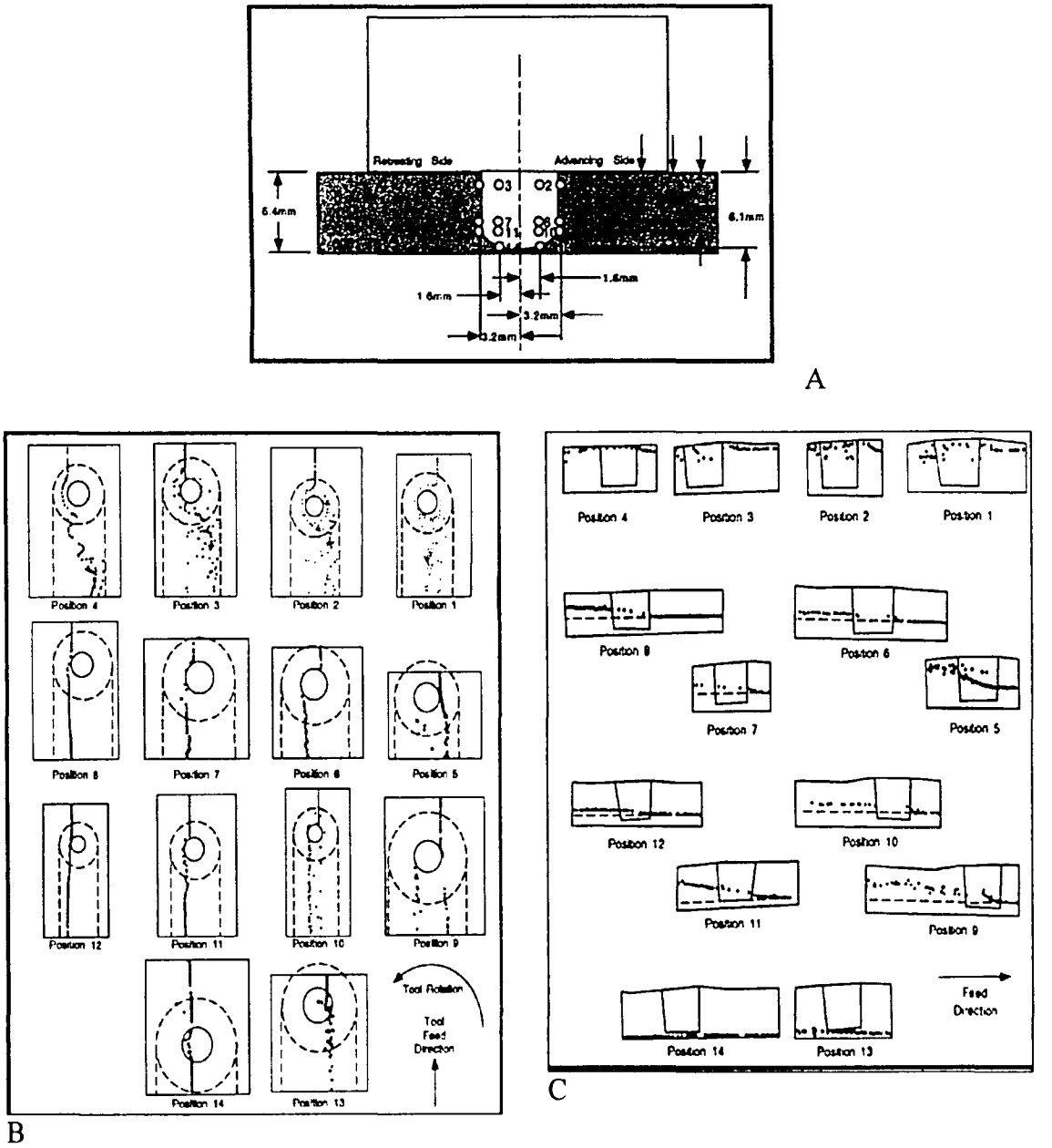

Fig. 2- 3 A) Original placement of the line of steel shot tracers imbedded within 6061-T3 aluminum alloy, and the B) horizontal and C) vertical movement of tracers after welding[10].

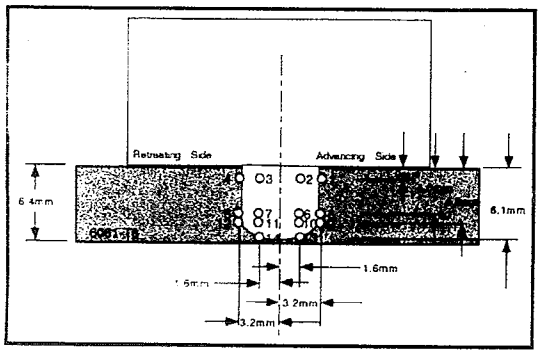

A

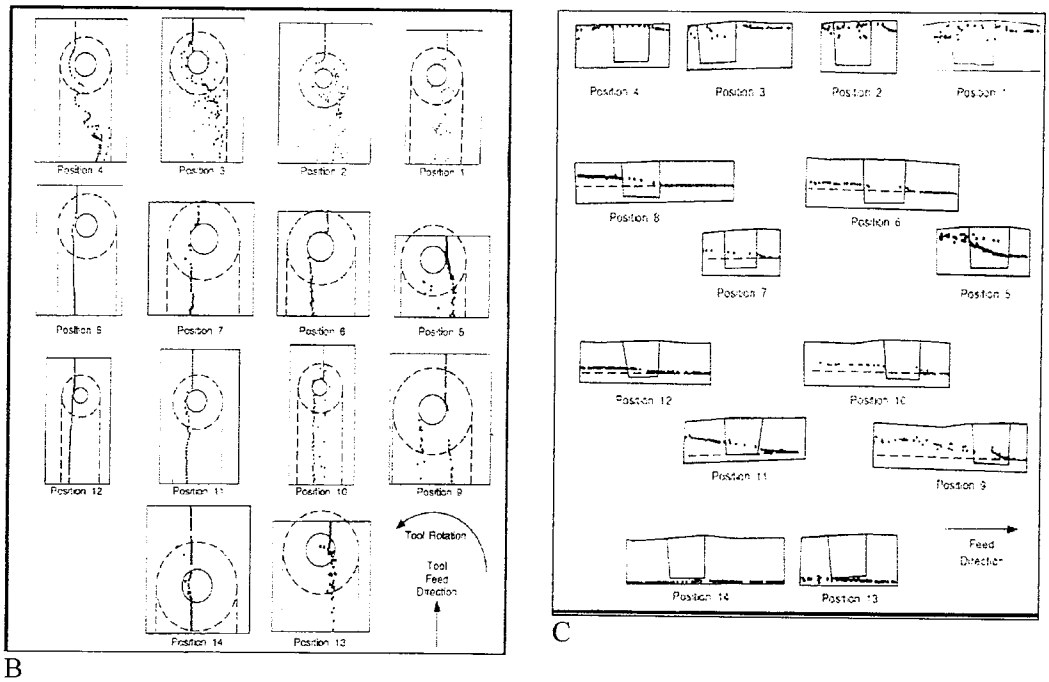

B C

Fig. 2- 3 A) Original placement of the line of steel shot tracers imbedded within 6061-T3 aluminum alloy, and the B) horizontal and C) vertical movement of tracers after welding[10].

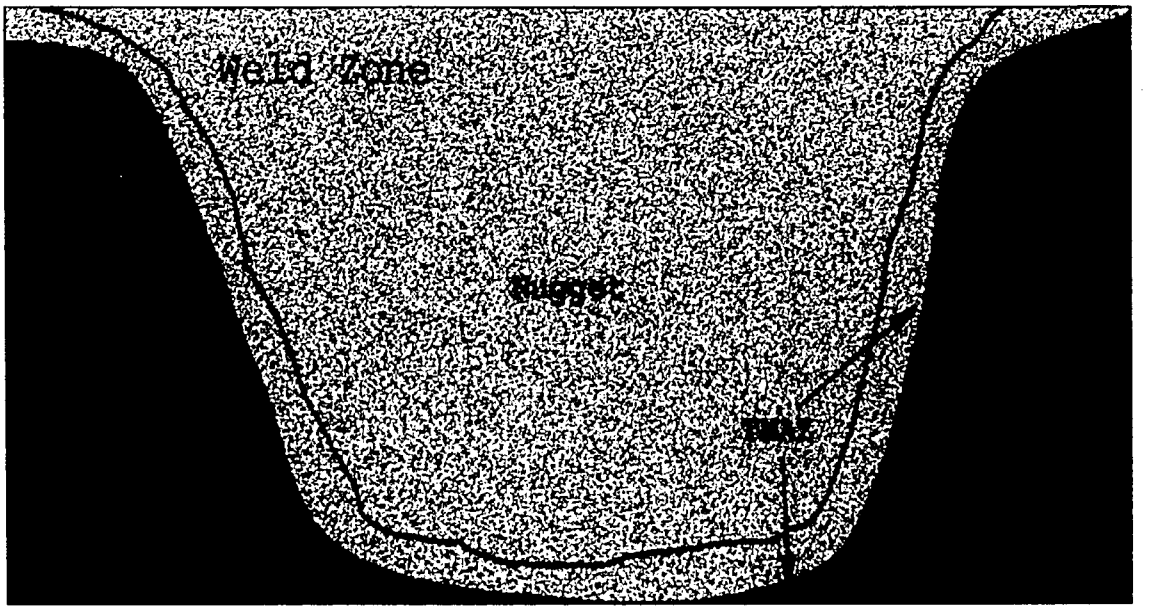

Fig. 2- 4 Schematic illustration of the microstructural regions developed as a result of FS weld

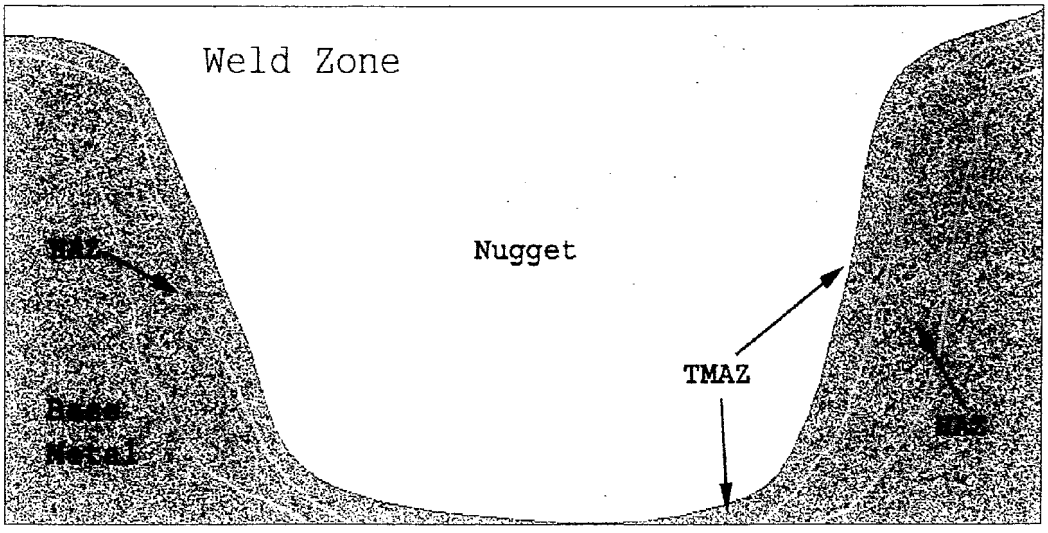

Fig. 2- 4 Schematic illustration of the microstructural regions developed as a result of FS weld

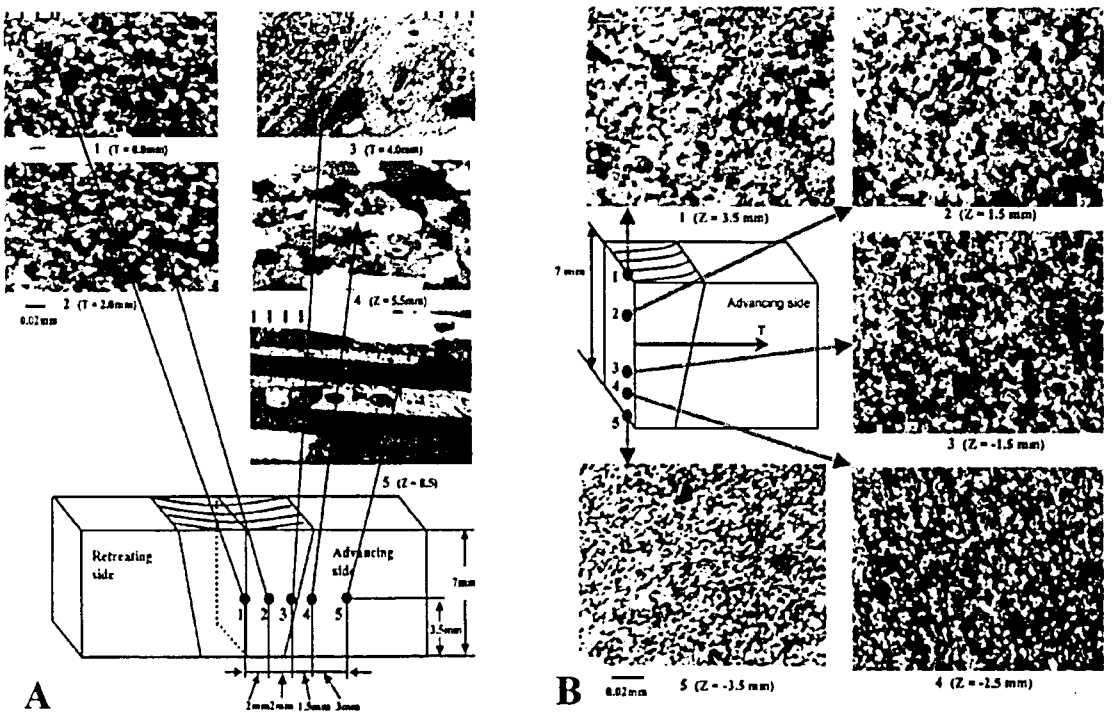

Fig. 2- 5 Microstructure as a function of distance A) from the weld centerline and B) from the plate surface in a FS weld of a 2024-T3 alloy[13].

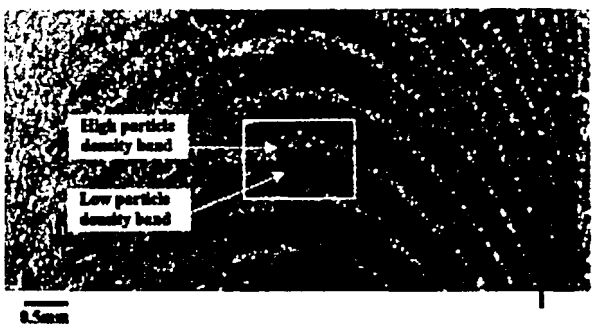

Fig. 2- 6 SEM image of the variations in the distribution of second phase particles in a 2024-T3 FS weld[13].

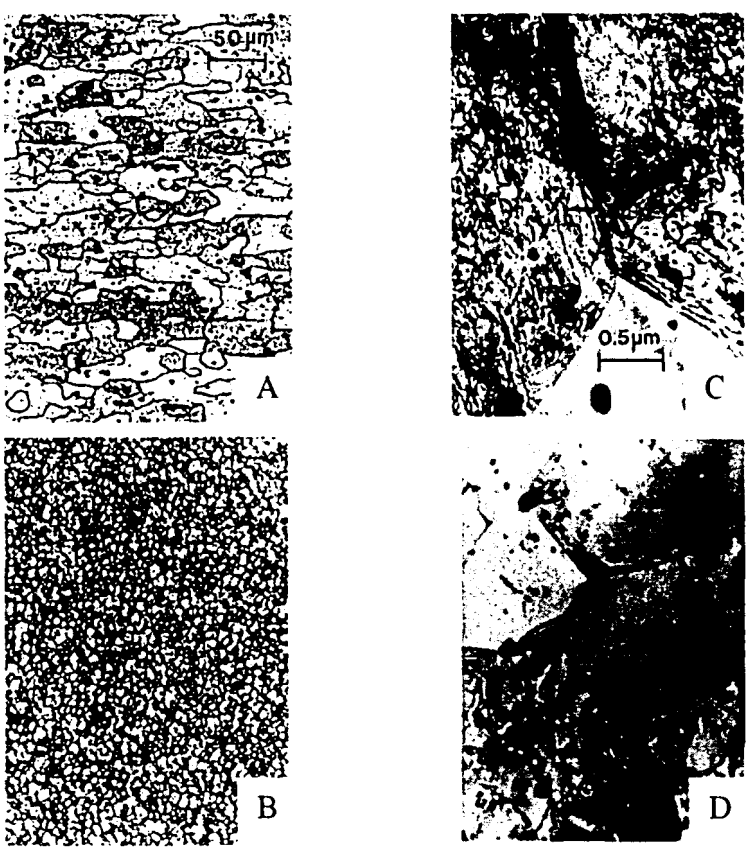

Fig. 2- 7 Representative microstructure of the 2024-T4 A) base metal and the B) nugget and the corresponding TEM images of the C) base metal and D) nugget[5].

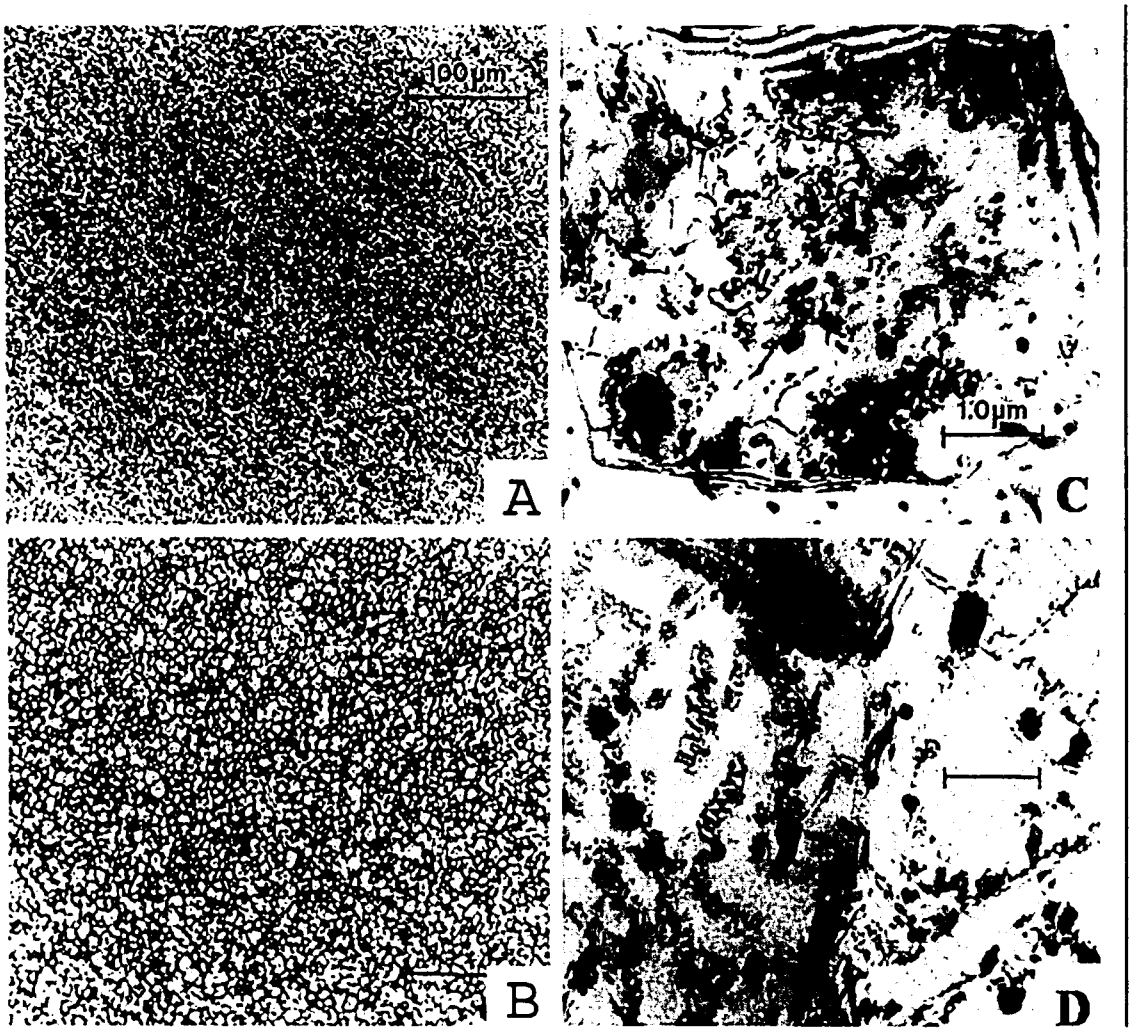

Fig. 2- 8 Residual grain size in the nugget of a 2024-T4 alloy produced using rotational speeds of A) 400 and B) 800 rpm and the TEM images of their corresponding sub-structures at rotational speeds of D) 400 and E) 800 rpm[5].

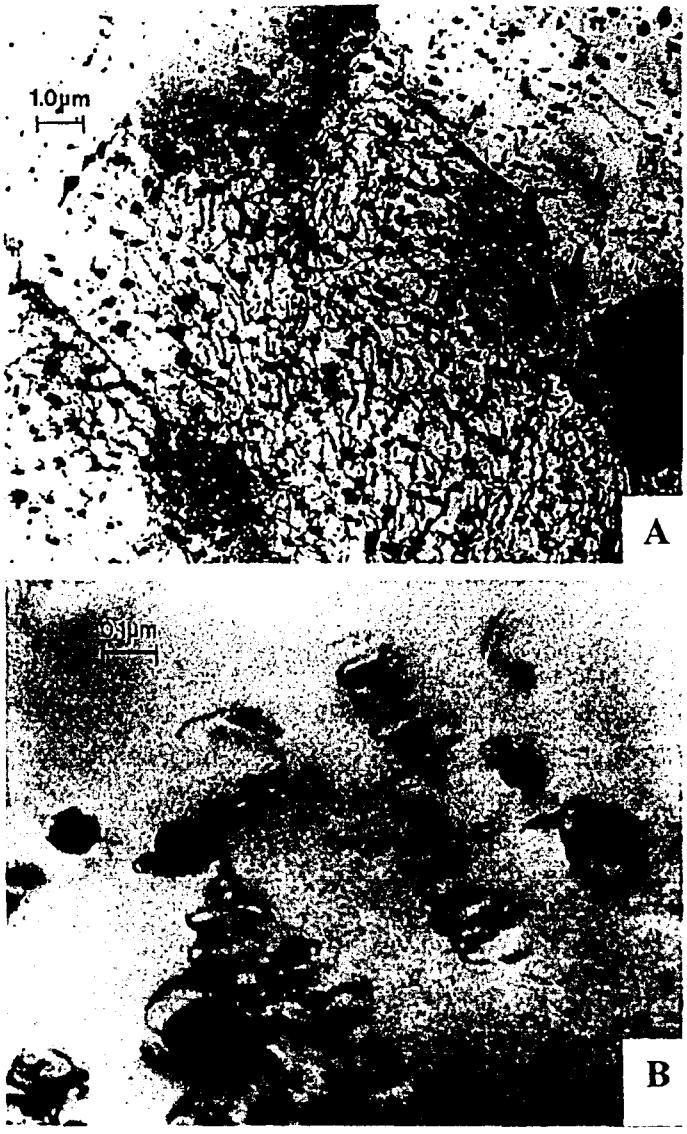

Fig. 2- 9 A) Dislocation spirals in the nugget region of the welds on a 2024-T4 alloy produced at rotational speed of 800 rpm and B) high magnification image of the spirals[5].

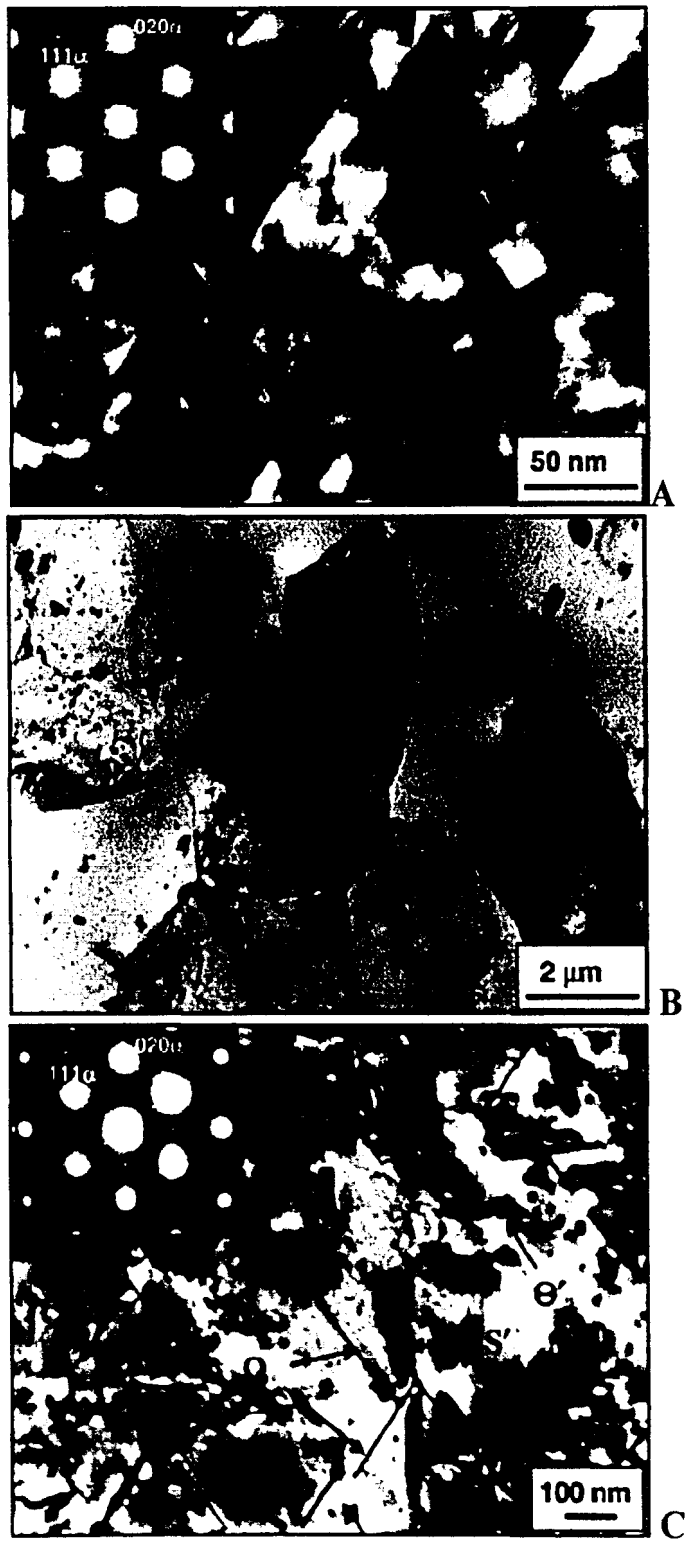

Fig. 2- 10 A) TEM micrograph and corresponding diffraction pattern of the AlCuMgAg base alloy, B) TEM micrograph of the nugget, and C) TEM micrograph of the TMAZ and corresponding diffreaction pattern[16].

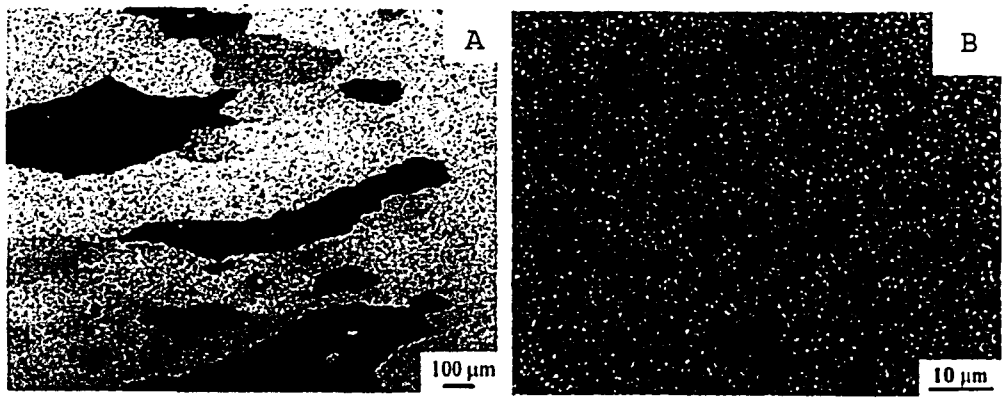

Fig. 2- 11 A) Microstructure of the base metal of a 2024-T4 alloy and B) fine grained nugget of the FS weld[17].

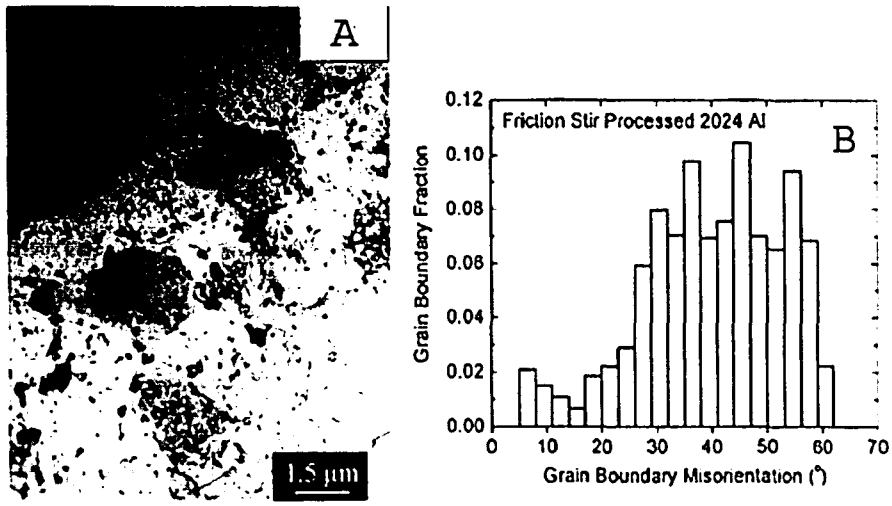

Fig. 2- 12 A)TEM micrograph of the nugget of a 2024-T4 alloy showing recrystallized grains and second phase particles and B) grain boundary misorientation distribution in the nugget[17].

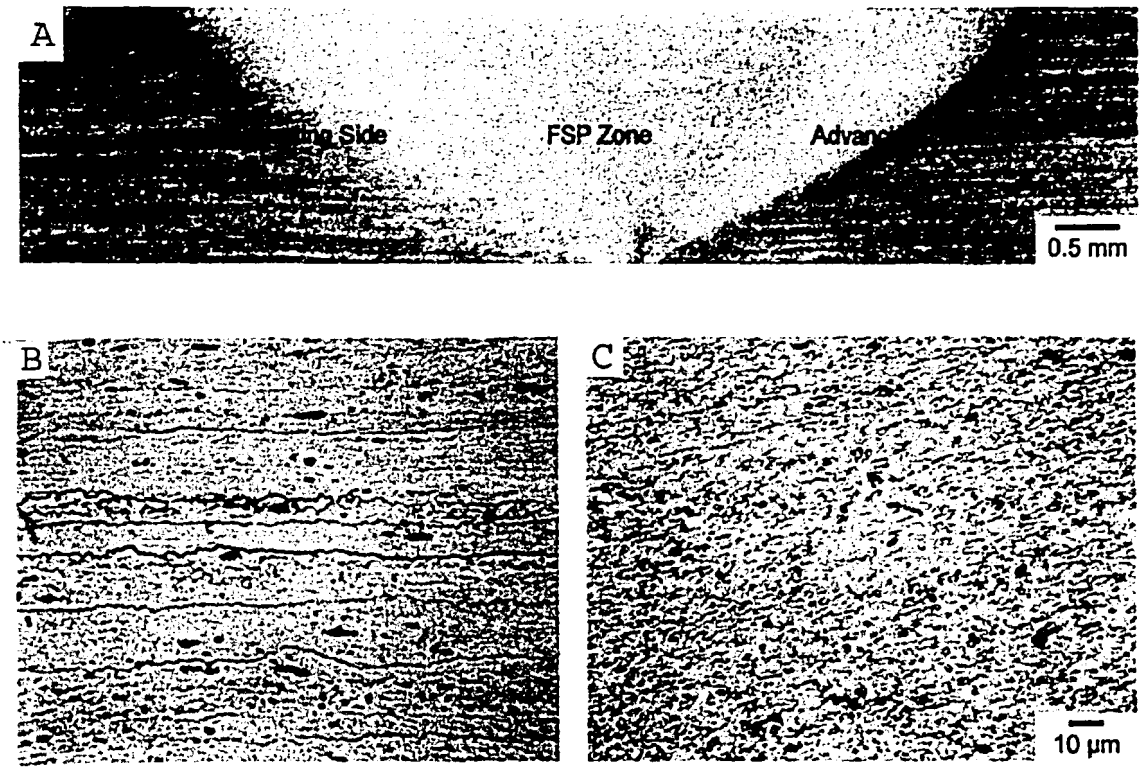

Fig. 2- 13 Light optical images of a 1050 alloy of the A) overall morphology, B) the base metal and the nugget[18].

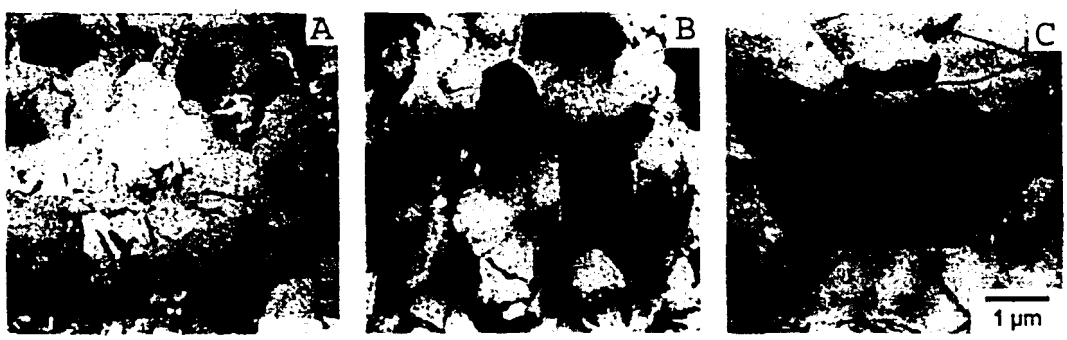

Fig. 2- 14 TEM micrographs of the nugget of a 1050 alloy using a rotational speed of A) 560, B) 980 and C) 1840 rpm and a constant traverse rate of 155mm/min[18].

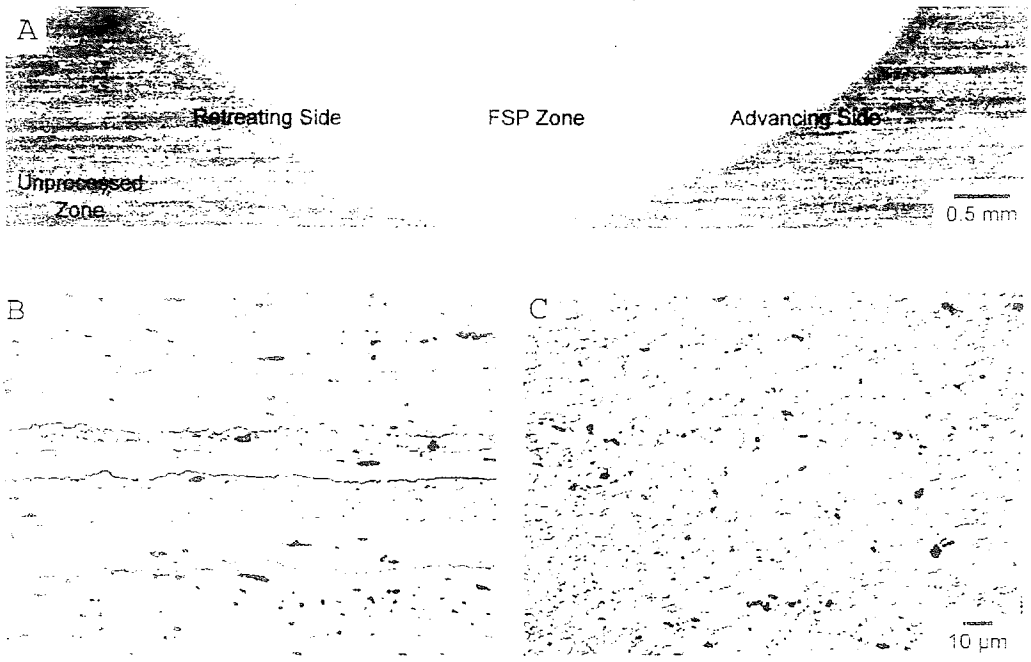

Fig. 2- 13 Light optical images of a 1050 alloy of the A) overall morphology, B) the base metal and the nugget[18].

Fig. 2- 14 TEM micrographs of the nugget of a 1050 alloy using a rotational speed of A) 560, B) 980 and C) 1840 rpm and a constant traverse rate of 155mm/min[18].

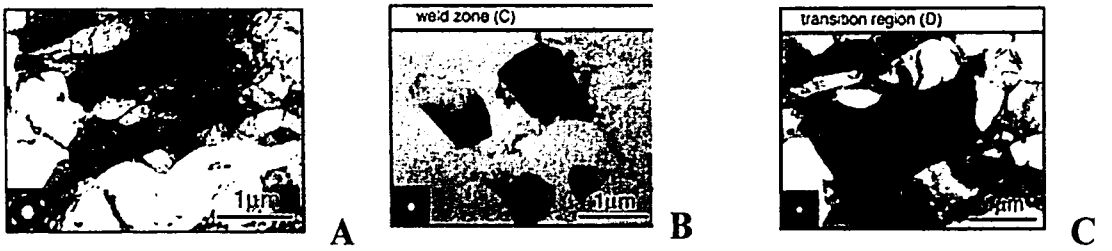

Fig. 2- 15 TEM images of 1050 alloy of A) the base (ECAP) material, B) the nugget and C0 the TMAZ[19].

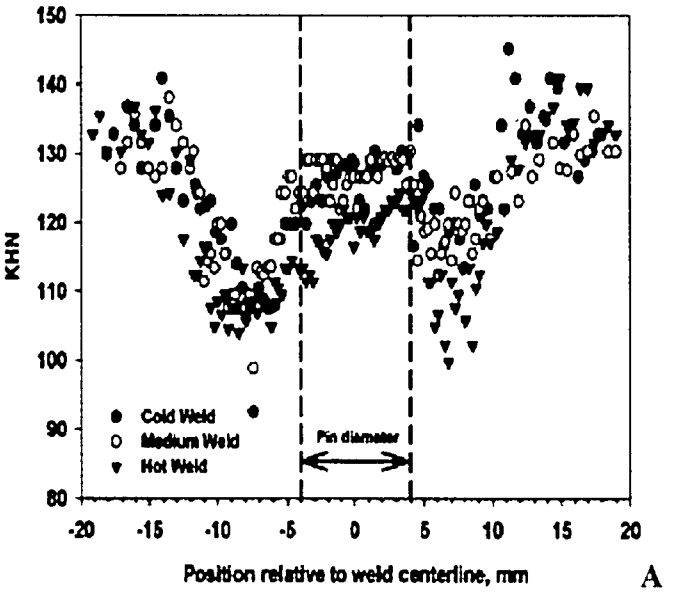

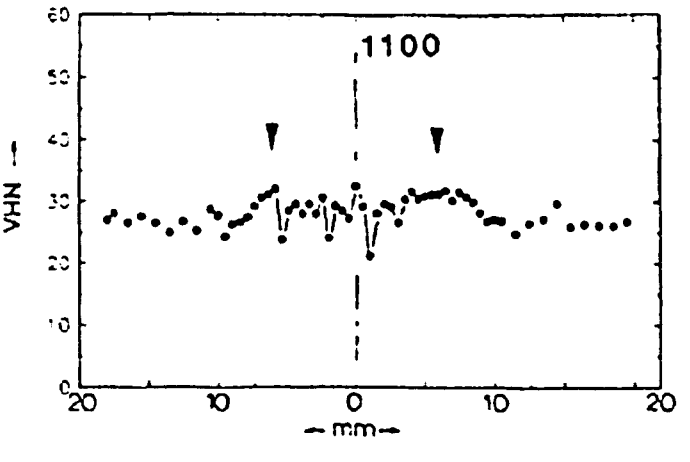

Fig. 2- 16 Microhardness measurements as a function of distance from the weld centerline of a A) 2024-T3 Al alloy[13] and B) 1100 Al alloy[20].

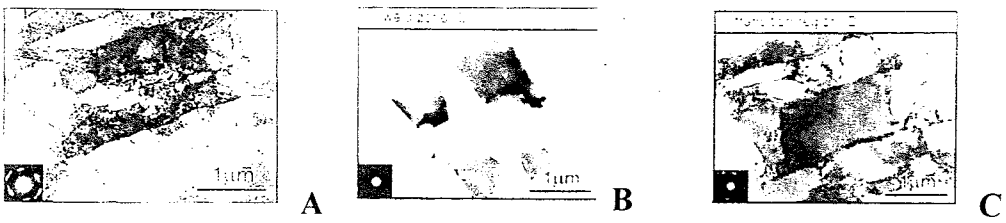

Fig. 2- 15 TEM images of 1050 alloy of A) the base (ECAP) material, B) the nugget and C0 the TMAZ[19].

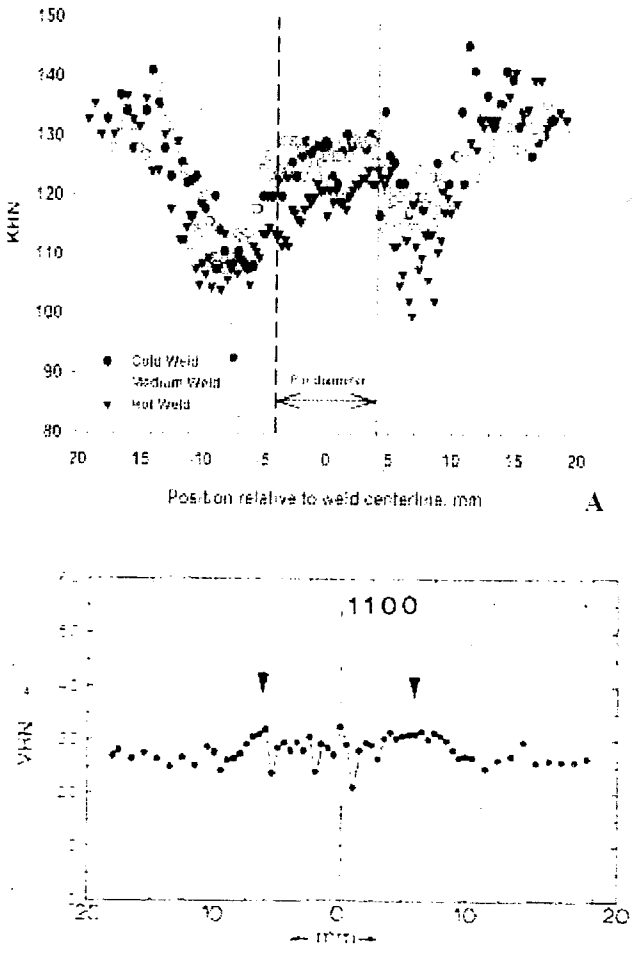

Fig. 2- 16 Microhardness measurements as a function of distance from the weld centerline of a A) 2024-T3 Al alloy[13] and B) 1100 Al alloy[20].

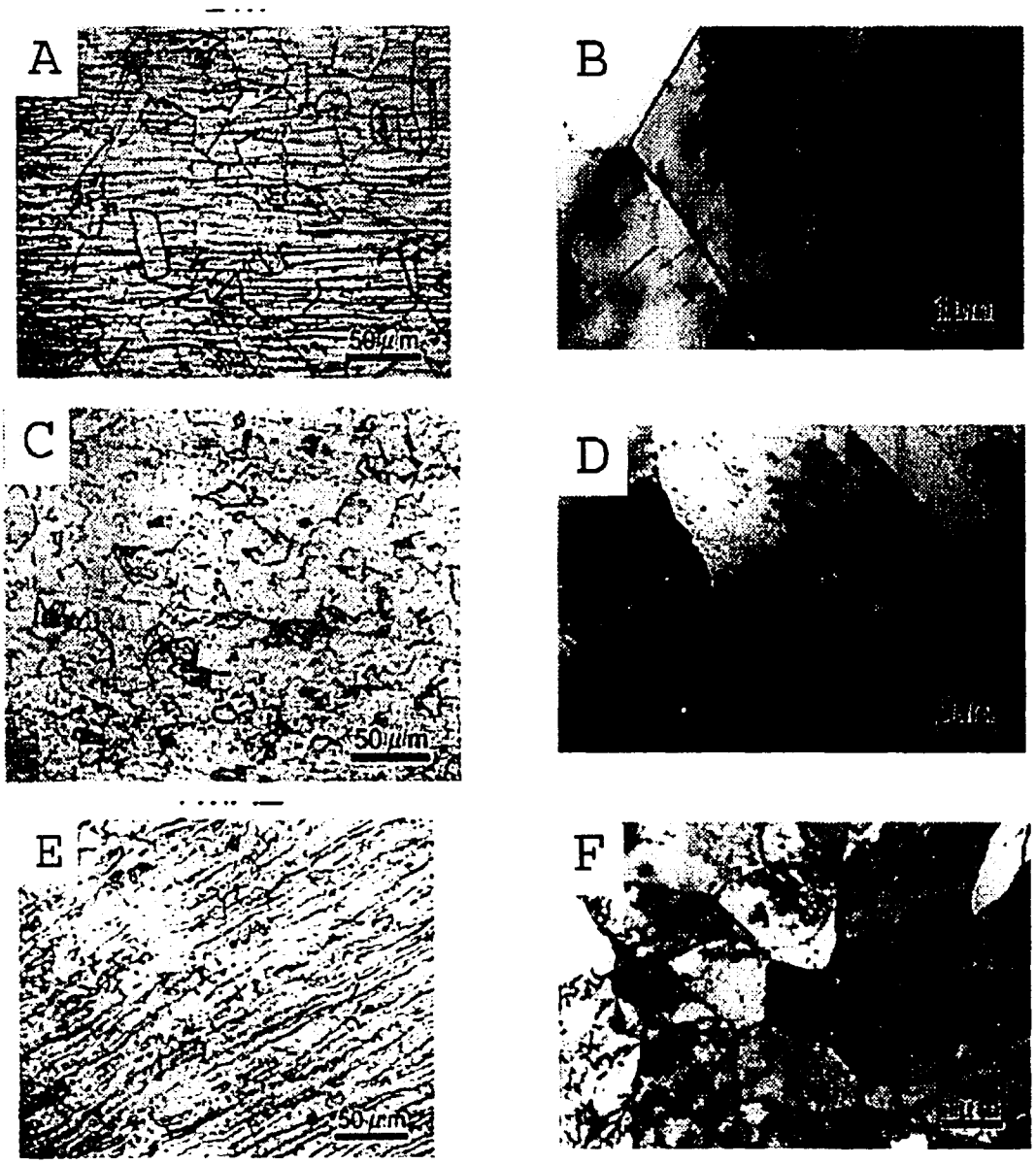

Fig. 2- 17 Optical and TEM images of A) and B) the base metal, C) and D) nugget, and E) and F) the TMAZ of a 304 SS FS weld[25].

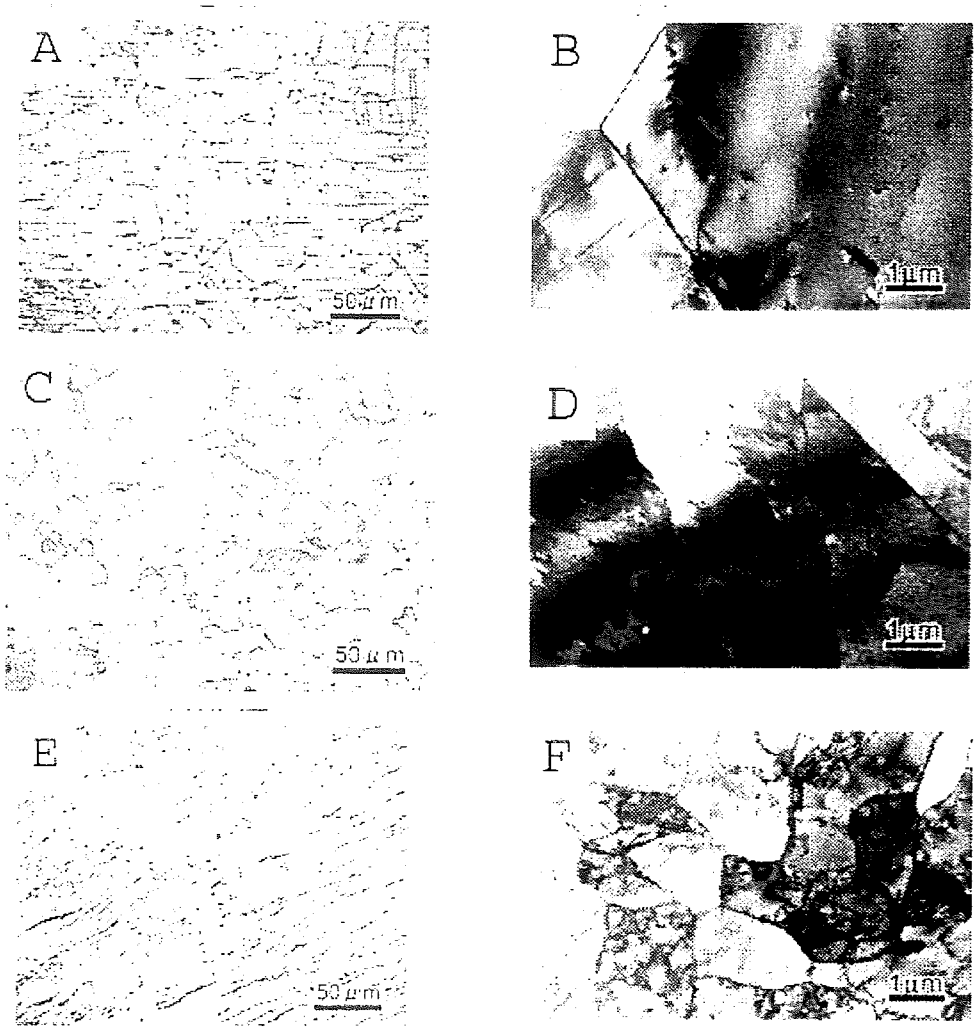

Fig. 2- 17 Optical and TEM images of A) and B) the base metal, C) and D) nugget, and E) and F) the TMAZ of a 304 SS FS weld[25].

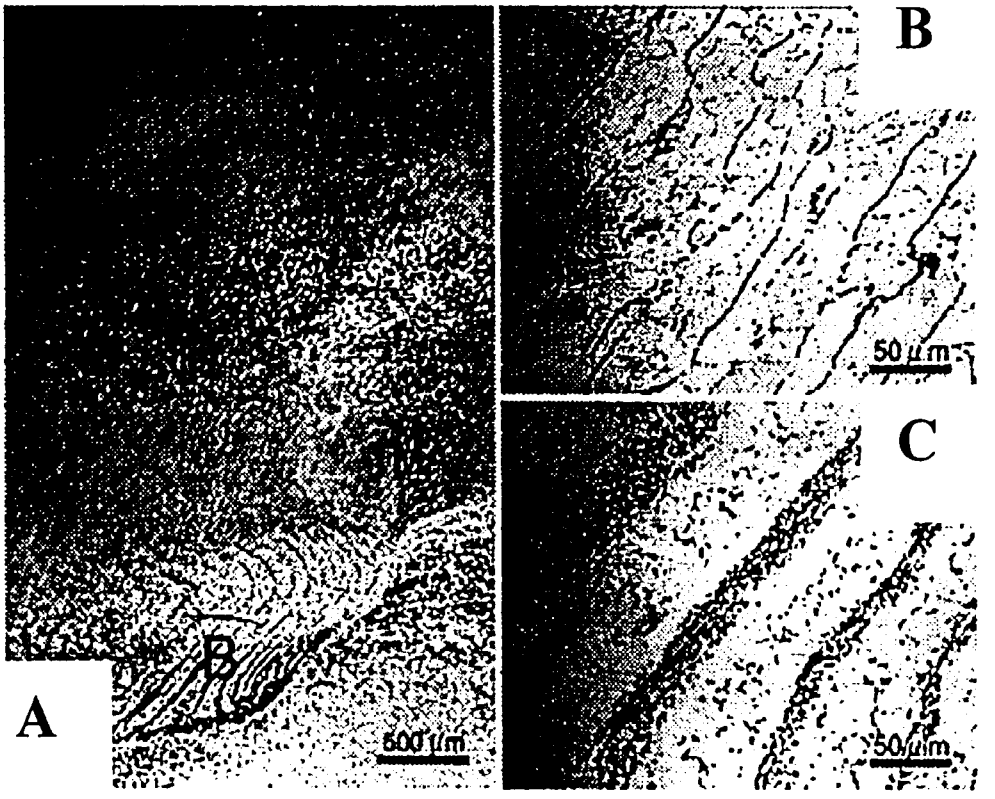

Fig. 2- 18 A) Overall image of the banding seen in the nugget with two different morphologies labeled A and B and the high magnification images of B) the morphology labeled as A and C) the morphology labeled as B[25].

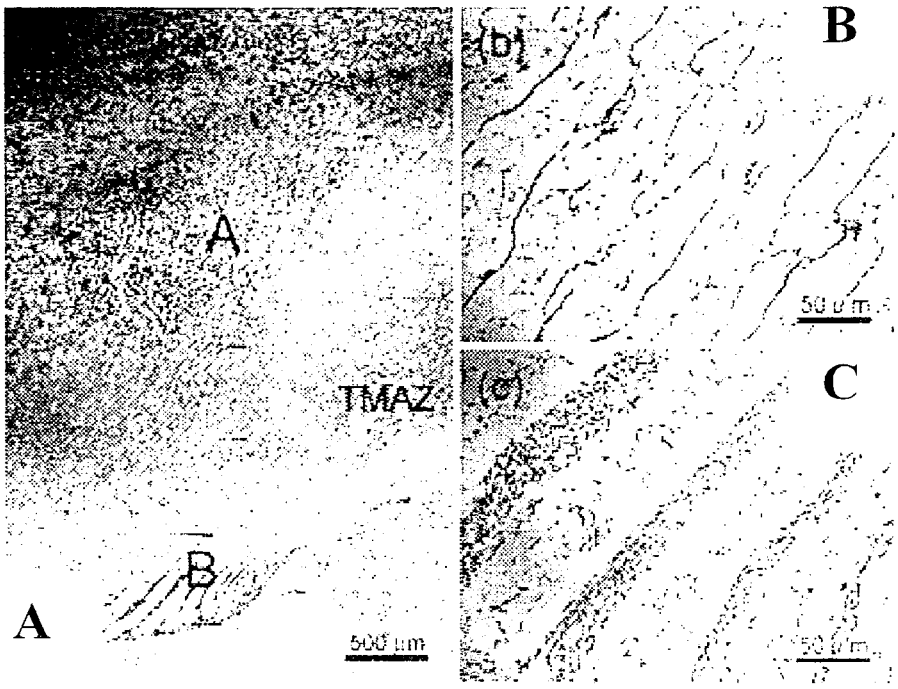

Fig. 2- 18 A) Overall image of the banding seen in the nugget with two different morphologies labeled A and B and the high magnification images of B) the morphology labeled as A and C) the morphology labeled as B[25].

Fig. 2- 19 A) OIM, B) TEM and C) EDS analysis of the banding labeled A in Figure 16A[25].

Fig. 2- 20 A) OIM, B) TEM and C) EDS analysis of the banding labeled B in Figure 16A[25].

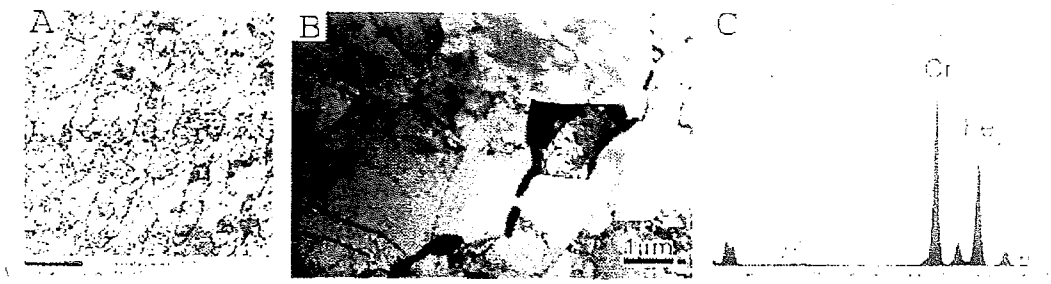

Fig. 2- 19 A) OIM, B) TEM and C) EDS analysis of the banding labeled A in Figure 16A[25].

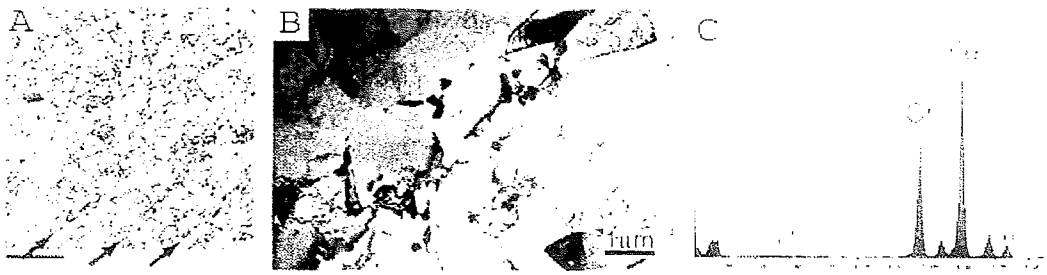

Fig. 2- 20 A) OIM, B) TEM and C) EDS analysis of the banding labeled B in Figure 16A[25].

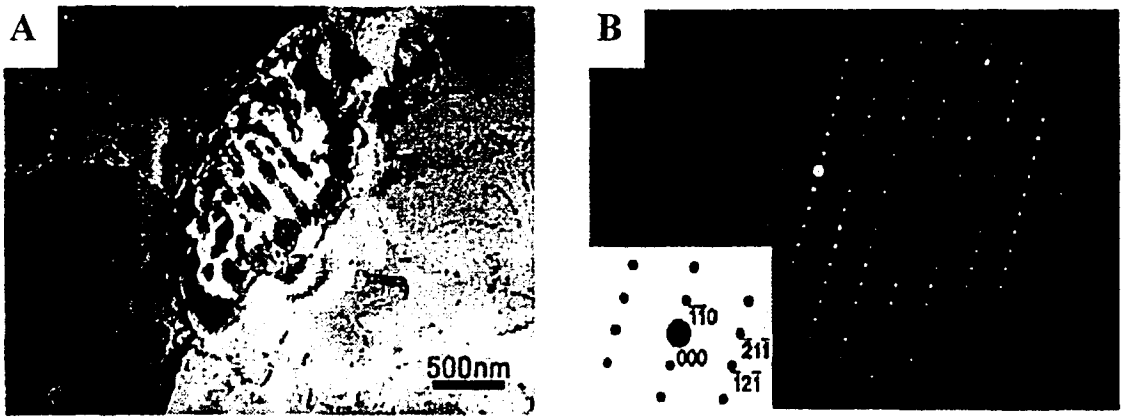

Fig. 2- 21 A) TEM image of the particles labeled as A in Figure 2-18 and B) the corresponding diffraction pattern[25].

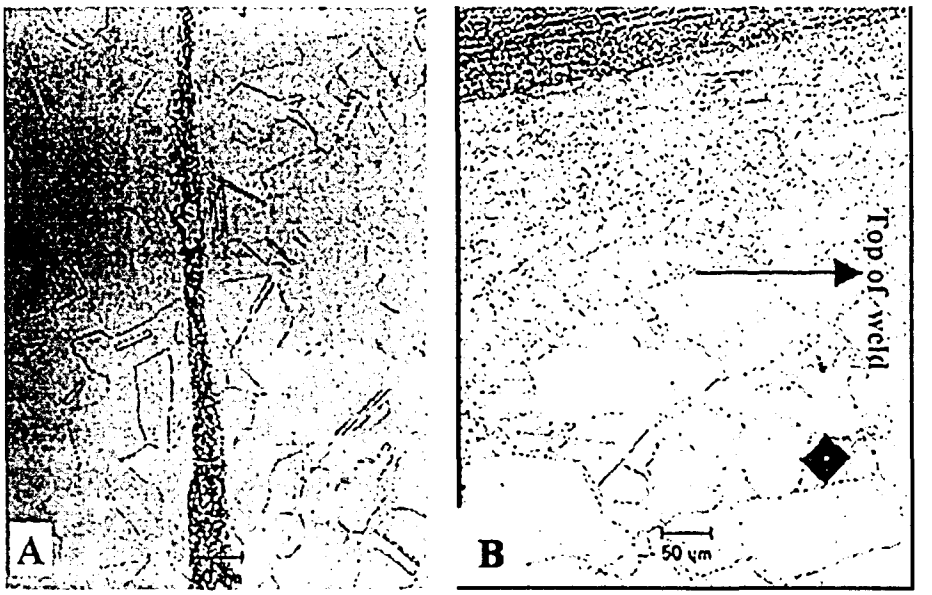

Fig. 2- 22 Microstructure of AL-6XN A) base metal and B) the nugget, TMAZ, and HAZ[27].

Electrode reaction		*Standard potential 25°*
$Au^{2+} + 2e = Au$	Noble	1.70
$Au^{3+} + 3e = Au$		1.50
$Pt^{2+} + 2e = Pt$		1.2
$Pd^{2+} + 2e = Pd$		0.987
$Hg^{2+} + 2e = Hg$		0.854
$Ag^{+} + e = Ag$		0.800
$Cu^{+} + e = Cu$		0.521
$Cu^{2+} + 2e = Cu$		0.337
$2H^{+} + 2e = H_2$		0.000
$Pb^{2+} + 2e = Pb$		−0.126
$Sn^{2+} + 2e = Sn$		−0.136
$Ni^{2+} + 2e = Ni$		−0.250
$Co^{2+} + 2e = Co$		−0.277
$Tl^{+} + e = Tl$		−0.336
$In^{3+} + 3e = In$		−0.342
$Cd^{2+} + 2e = Cd$		−0.403
$Fe^{2+} + 2e = Fe$		−0.440
$Ga^{3+} + 3e = Ga$		−0.53
$Cr^{3+} + 3e = Cr$		−0.74
$Zn^{2+} + 2e = Zn$		−0.763
$Cr^{2+} + 2e = Cr$		−0.91
$Mn^{2+} + 2e = Mn$		−1.18
$Zr^{4+} + 4e = Zr$		−1.53
$Ti^{2+} + 2e = Ti$		−1.63
$Al^{3+} + 3e = Al$		−1.66
$Hf^{4+} + 4e = Hf$		−1.70
$U^{3+} + 3e = U$		−1.80
$Be^{2+} + 2e = Be$		−1.85
$Mg^{2+} + 2e = Mg$		−2.37
$Na^{+} + e = Na$		−2.71
$Ca^{2+} + 2e = Ca$		−2.87
$K + + e = K$		−2.93
$Li^{+} + e = Li$	Active	−3.05

Fig. 2- 23 Electromotive Force Series[35].

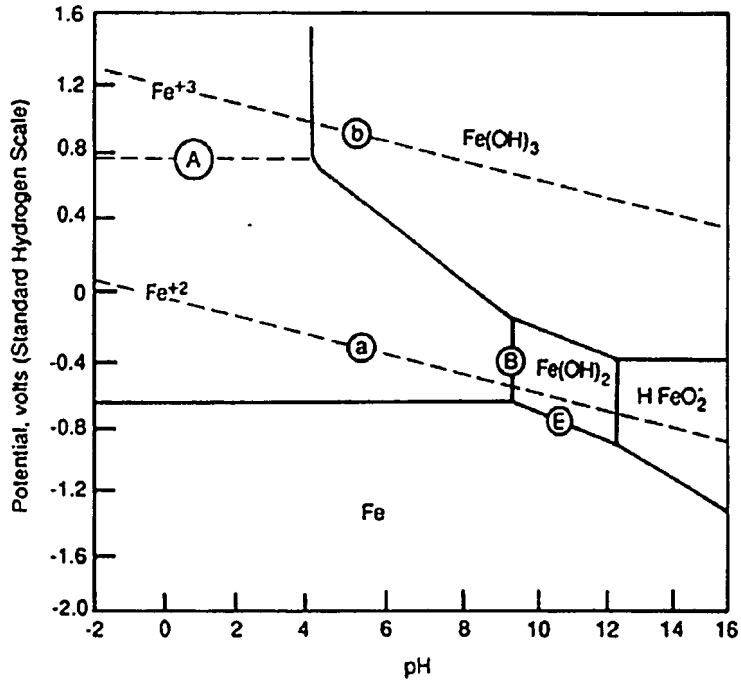

A

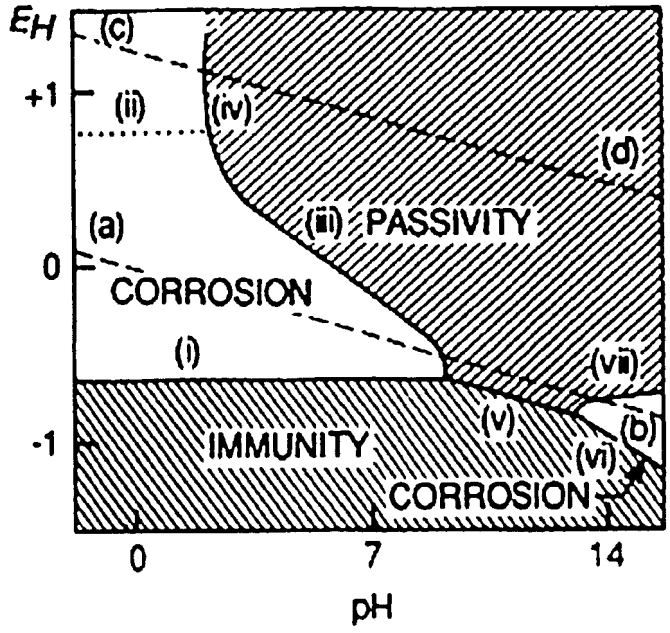

B

Fig. 2- 24 Pourbaix Diagram for Steel in H_2O showing A) stable phases and B) showing behavior of the metal in[36].

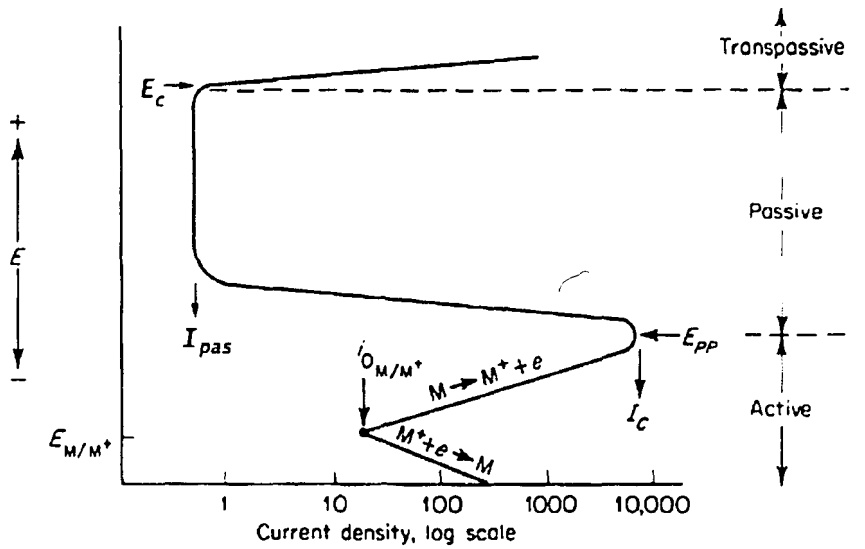

Fig. 2- 25 Typical "s-shaped" polarization curve for metal with an active-passive transition (modified figure)[37].

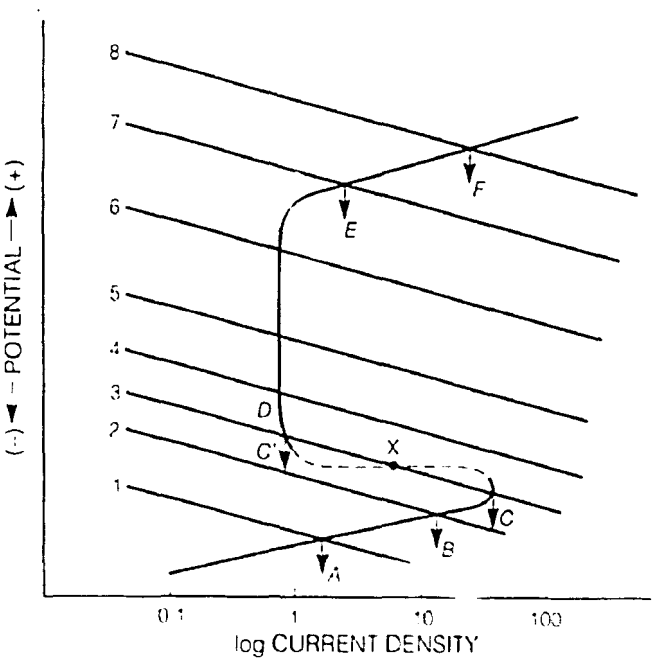

Fig. 2- 26 The oxidation polarization curve of a metal and the reduction polarization curves of different solutions[37].

Fig. 2- 27 Pitting of a Type 430 stainless steel tube showing under cutting[40].

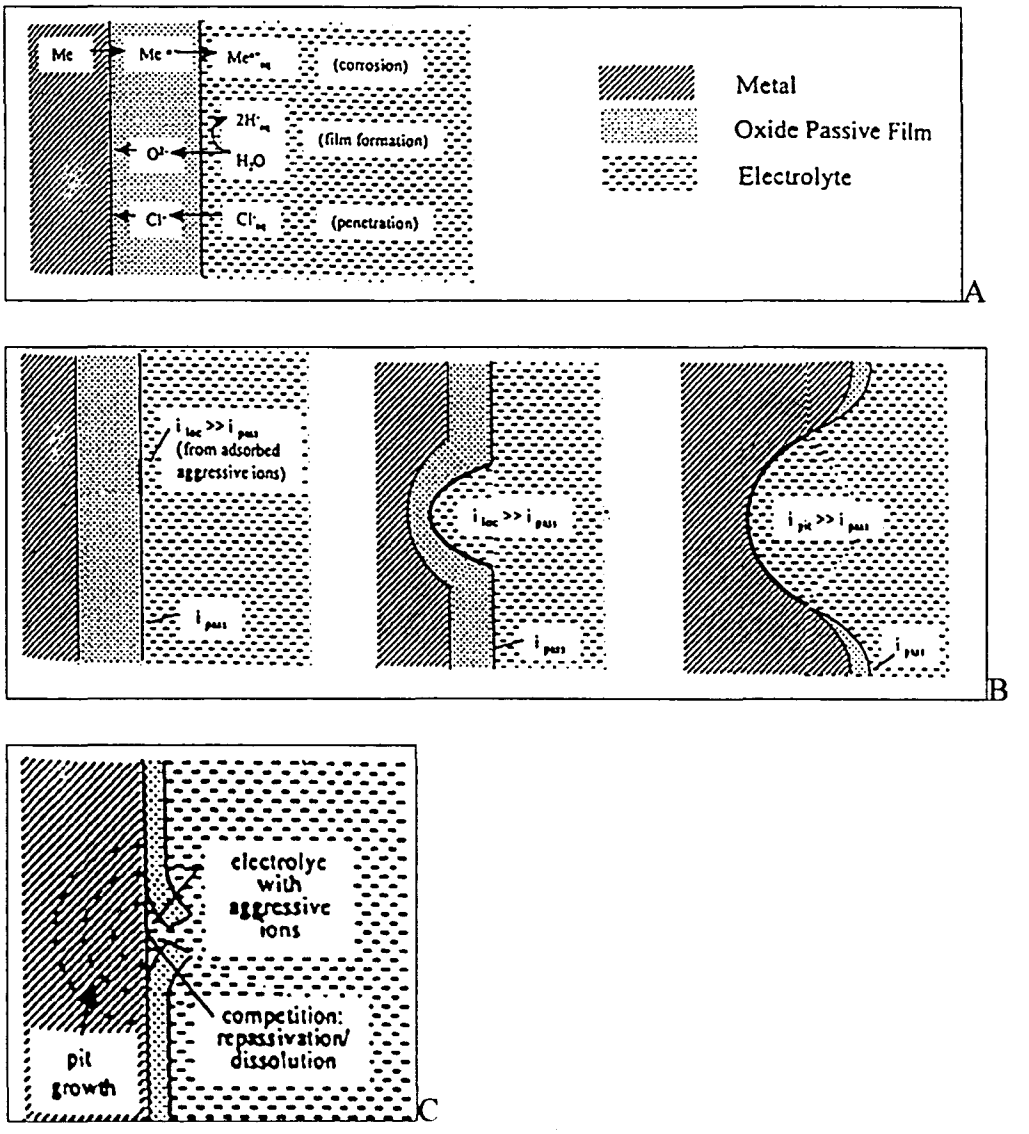

Fig. 2- 28 Illustrations of the passive film breakdown in the A) penetration method B) adsorption mechanisms and C) film breaking mechanism[39].

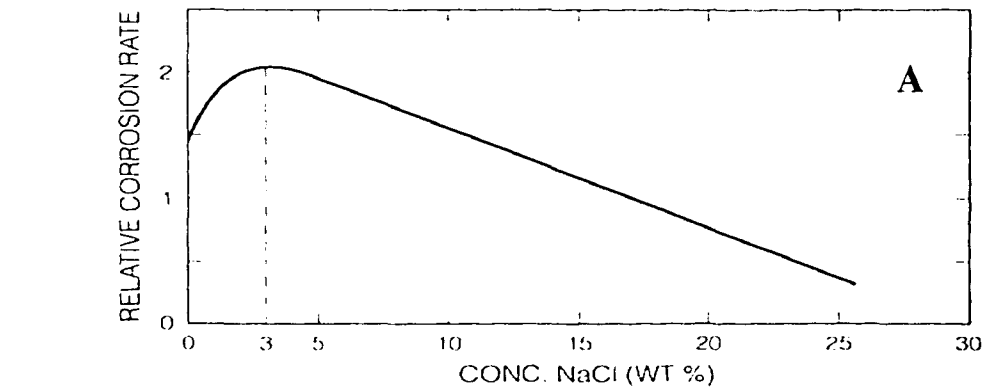

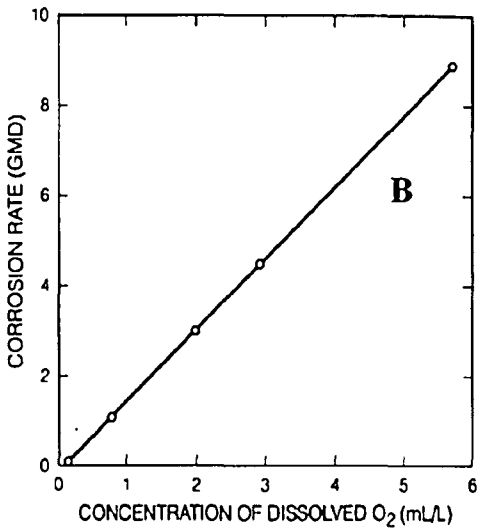

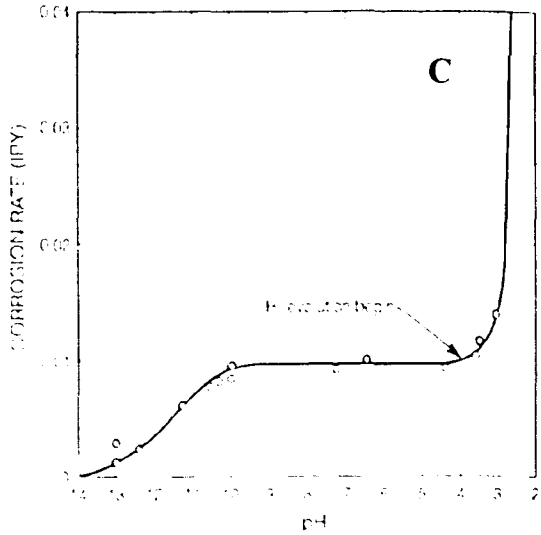

Fig. 2- 29 Effect of A) NaCl concentration, B) dissolved oxygen concentration, and C) pH on the corrosion rate of stainless steel[6].

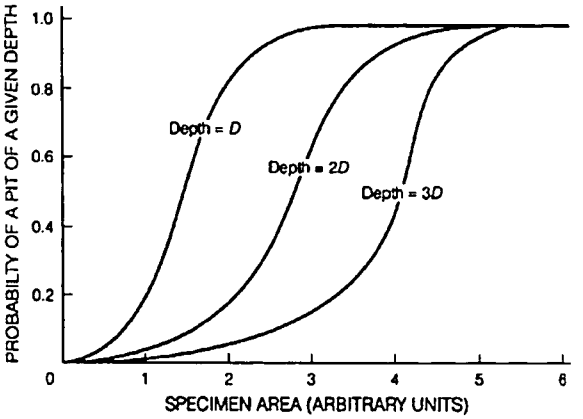

Fig. 2- 30 Pitting probability as a function of exposed area[40].

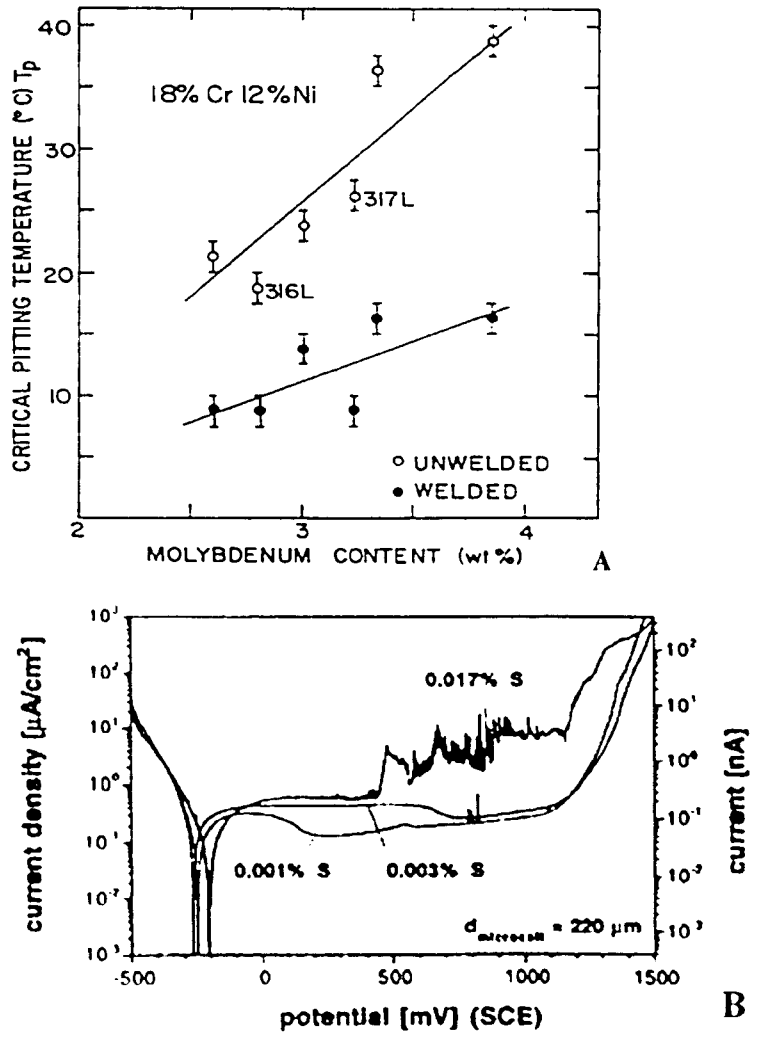

Fig. 2- 31 Effect of A) molybdenum content[53] and B) sulfur content on pitting of stainless steels[55].

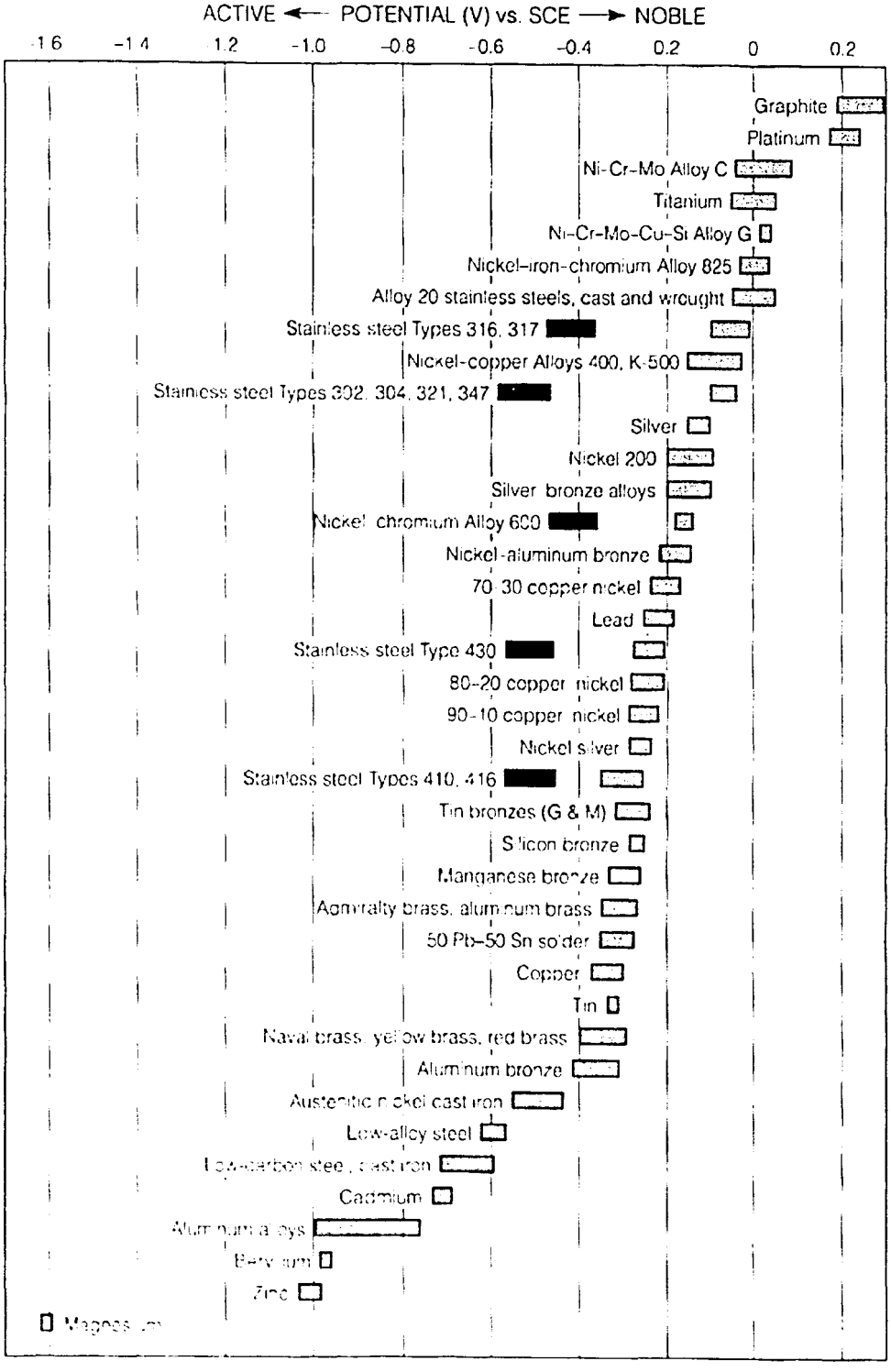

Fig. 2- 32 The gavlvanic series[57].

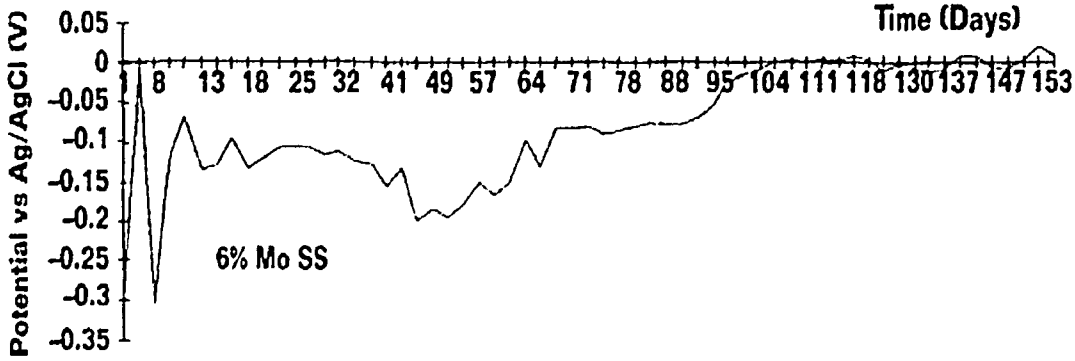

A

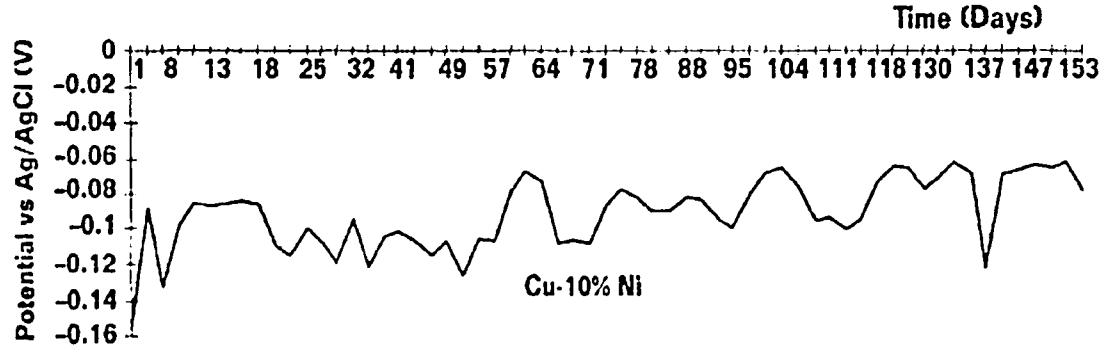

B

Fig. 2- 33 The OCP as a function of time for A) AL-6XN and B) Cu-10%Ni[68].

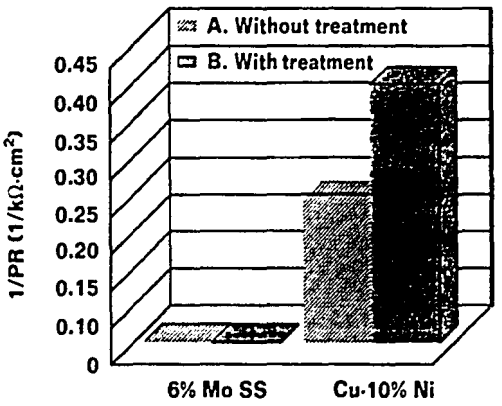

Fig. 2- 34 The results of the polarization resistance for AL-6XN and Cu-10%Ni[68].

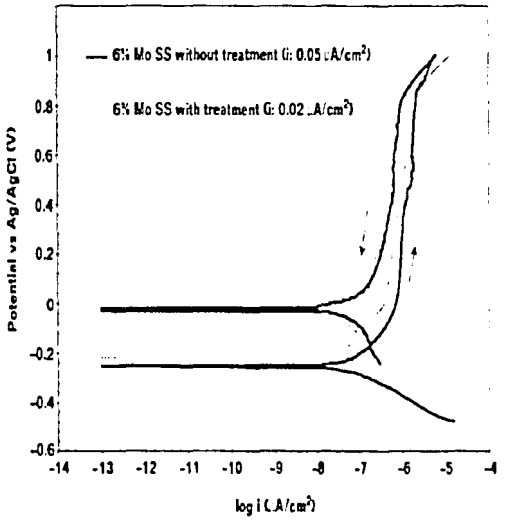

A

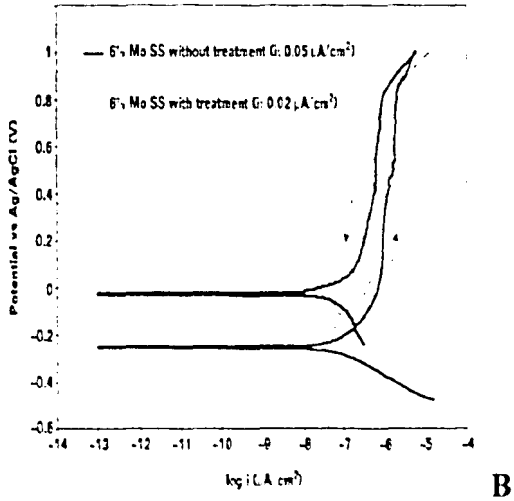

B

Fig. 2- 35 Results of the cyclic polarization tests of A) AL-6XN and B) Cu-10%Ni[68].

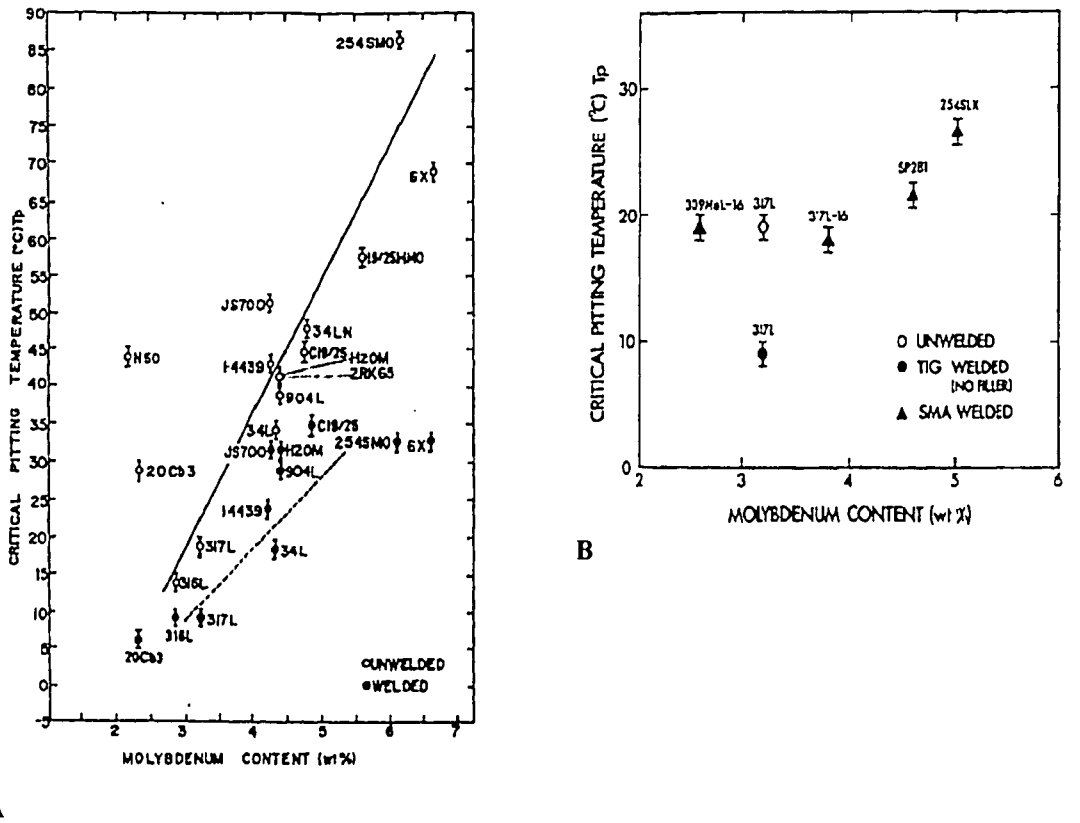

Fig. 2- 36 A plot of CPT versus the molybdenum content A) for a variety of high alloy stainless steels[74] and B) showing the effect of autogenous welding and welding with a high alloy filler metal[75].

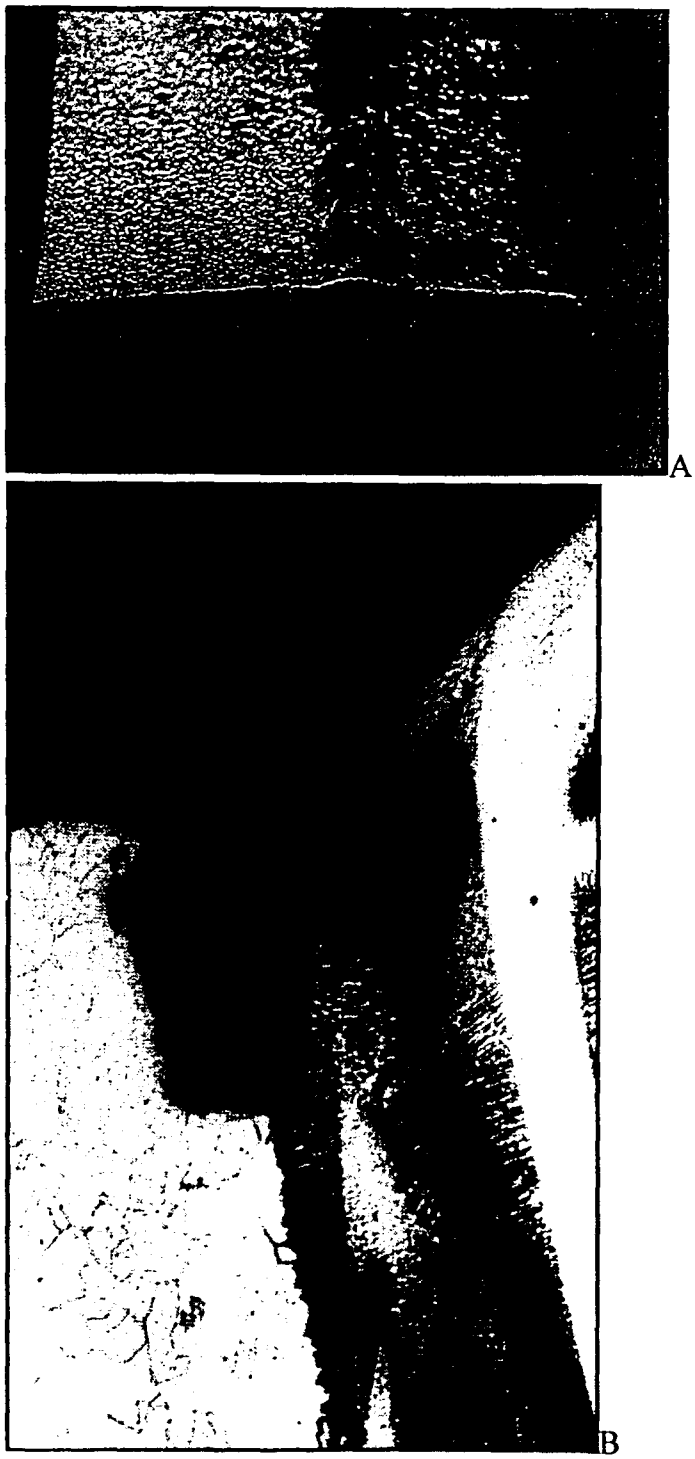

Fig. 2- 37 A) and B) Localized attack in the unmixed region of AL-6XN arc welds using a high alloy filler metal[72].

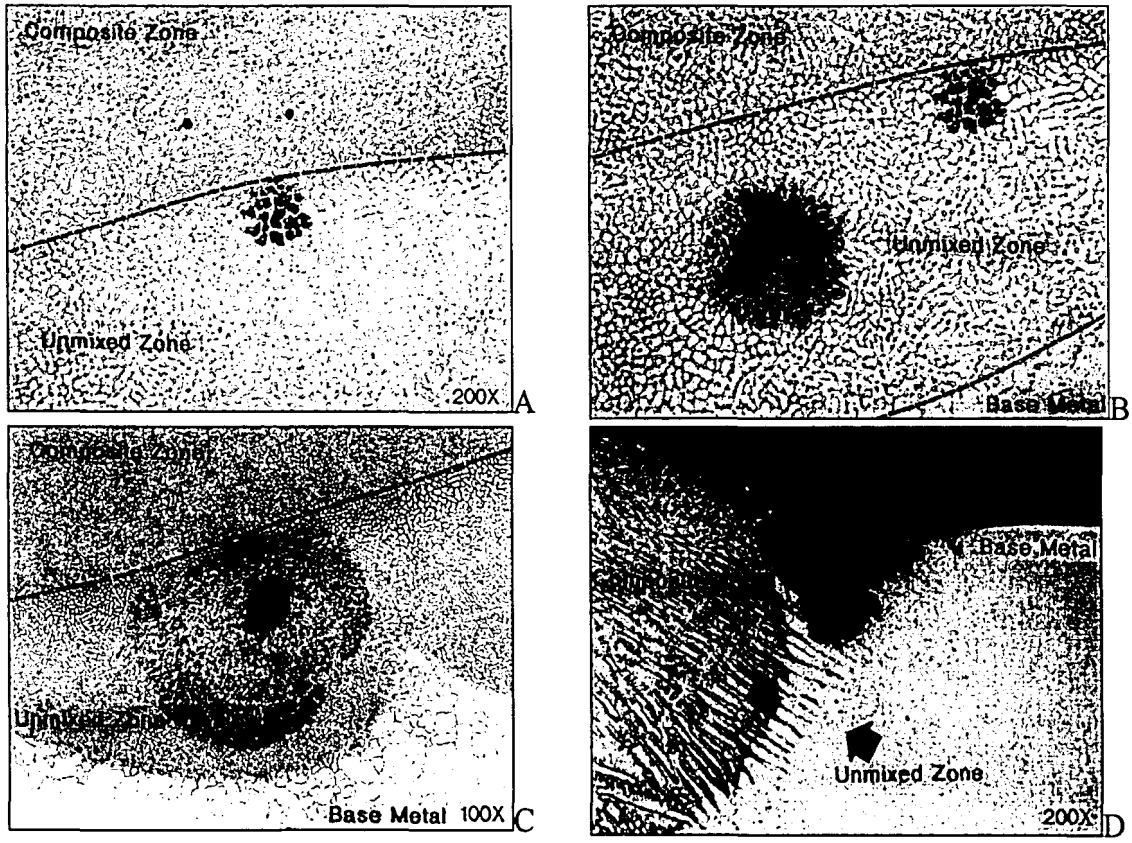

Fig. 2- 38 Pit growth of a dissimilar weld on AL-6XN after immersion in ferric chloride for A) 2 minutes, B) 4 minutes, C) 30 minutes and D) the transverse view of the weld at 30 minutes[76].

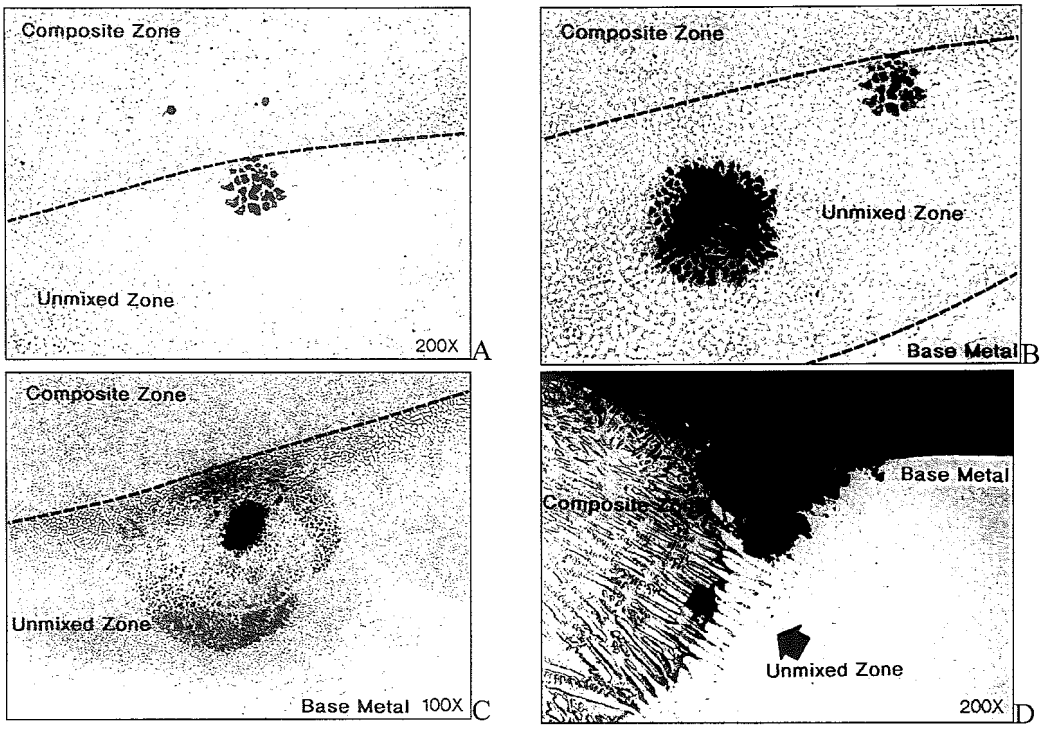

Fig. 2- 38 Pit growth of a dissimilar weld on AL-6XN after immersion in ferric chloride for A) 2 minutes, B) 4 minutes, C) 30 minutes and D) the transverse view of the weld at 30 minutes[76].

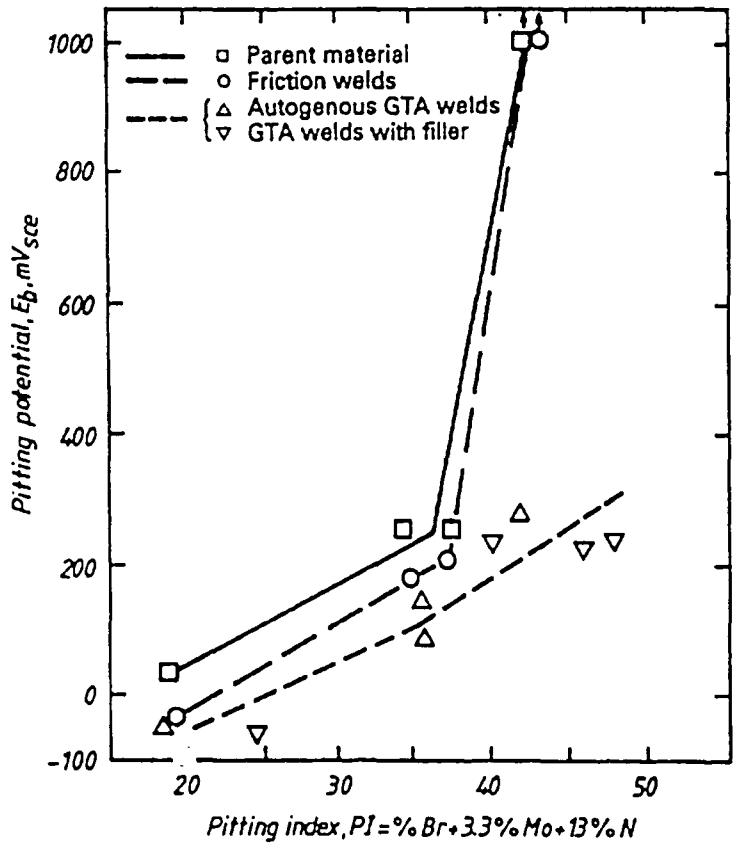

Fig. 2- 39 Pitting potential determined for stainless steel parent material, arc welds and friction welds[79].

3. Experimental Procedure

3.1 Microstructural Characterization of a Double-Sided FS weld.

Two plates of AL-6XN were joined via a double-sided FS weld in a butt-weld configuration. The plate thickness was 6.35 mm (0.25 in). Welds were produced using a travel speed of approximately 0.847 mm/sec (2 in./min), a tool rotational speed of 150 rpm, and a z-axis load of approximately 80 kN (18000 lb_f).

Cross-sections of the transverse view of the welds were cut and prepared for microstructural analysis. The samples were mounted in a thermosetting epoxy and prepared according to standard metallographic preparation techniques. The samples were then electrolitically etched in a 10% oxalic acid solution and analyzed using light optical microscopy (LOM) and scanning electron microscopy (SEM). A JEOL 6300 and an XL30, both operating at an accelerating voltage of 20kV, were the microscopes used for SEM analysis. Grain size measurements were performed in selected areas according to ASTM E112[80]. Four microhardness traces across the welds were performed with a LECO M400FT Hardness tester in accordance with ASTM E384[81] using a Knoop indenter and a load of 300 gm.

Characterization of the elemental distribution across different regions of the weld was performed using electron probe microanalysis (EPMA). Regions of interest were marked and the samples were analyzed in the as-polished condition to avoid any surface relief from etching. EPMA was conducted using a JEOL 733 Superprobe equipped with four independent wavelength dispersive spectrometers. The analysis was completed using an accelerating voltage of 15 kV and a beam current of 32 nA. The K_α lines were

used for elements Fe, Ni, and Cr, while the L_α line was used for Mo[82]. Raw data were converted to weight percentages using an established ZAF algorithm[83]. The base metal and weld zone were probed randomly to acquire representative compositions while four line scans were performed to check for composition changes across various regions of the weld. Two scans traversed from the first weld pass to the second weld pass while two other line scans traversed from the weld zone into the base metal. Data was acquired at 10 μm increments along lines that were approximately 500 μm in length.

In addition, thin specimens approximately 20 x 10 μm^2 for TEM analysis were extracted from the HAZ using a FEI D B235 Focused Ion Beam (FIB) milling machine. All specimens were prepared across the grain boundaries in the HAZ by milling with Ga ion-beam at an accelerating voltage of 30 kV. To protect the thin section during milling, the surface was covered with a 1-μm-thick Pt layer internally deposited before the milling. After rough sectioning, the specimens were cleaned by low-dose Ga ion-beam (beam current of 300 pA) as the last step to avoid significant Ga contamination. After extraction from the HAZ, specimens were mounted on a copper grid with an amorphous holey carbon film.

Microstructural observation and electron-diffraction analysis of the specimens were both performed in a JEOL JEM-2010F TEM operated at 200 kV. Selected-area diffraction (SAD) was used for phase identification and analysis orientation relationship around grain boundaries in the HAZ.

3.2 Microstructural Characterization of a Single-Sided FS weld

Two plates containing single-sided FS welds were analyzed, Figure 3-1. As labeled in the image, each plate contained one full weld and two half welds (originally full welds but sectioned in half). The single-sided FS welds were produced with the same parameters as the double-sided FS weld – a travel speed of approximately 0.847 mm/sec (2 in./min), a tool rotational speed of 150 rpm, and a z-axis load of approximately 80 kN (18000 lb_f). The plate thickness was again 6.35 mm (0.25 in). The double-sided FS weld is made with a weld pass on each side of the plate where as the single-sided FS weld is made with only one weld pass.

A brief microstructural characterization was preformed to compare and contrast the resulting weld microstructures. Planar, as well as cross-sectional views, of the welds were sectioned, mounted, and prepared for microstructural characterization in the same methods as described previously. The microstructures were characterized using a combination of LOM and SEM. For the SEM analysis, an XL 30 operating at 20 kV was used.

3.3 Corrosion Behavior of a Single-Sided FS weld

3.3.1 CPT Testing

The CPT of AL-6XN FSW was determined according to a slightly modified ASTM G48-97, Method C[60]. This testing method involves immersion of test coupons in a 6% ferric chloride solution for a period of 72 hours. Although naval applications for FS

welds require pitting resistance in a marine environment, the ferric chloride solution is used for testing because it accelerates the pitting process. This solution simulates the composition of the electrolyte within the pit. Pitting tests in NaCl-based solutions and in natural seawater have confirmed the superior pitting resistance of AL-6XN. As no pitting was indicated by these test methods a more severe test environment is required[65].

All of the CPT samples were 20 mm x 7 mm 7 mm, Figure 3-2. The two original plates received, as described previously, contained 1 full weld and 2 half welds. One half weld contained the advancing side of a FS weld and the other half weld contained the retreating side of a FS weld. Due to the limited availability of material, only the CPT of the half welds (the advancing and the retreating halves) was determined. Approximately one fourth of the exposed area was consumed by the weld affected region. In addition, the CPT of as-received AL-6XN plate was determined for comparison to the FS weld and also to insure the accuracy of the CPT test.

All of the CPT samples were sectioned from the original plate using a high speed saw and then ground to a 120 grit surface finish on all six faces. The samples were then ultrasonically cleaned in acetone, dried, and allowed to passivate for at least 24 hours prior to testing. Test tubes filled with 150 mL of the ferric chloride solution were placed in a heated oil bath. The bath was given sufficient time before testing (typically an hour) to allow the solution to reach the desired temperature. The temperature of the oil bath was displayed digitally on the bath but was also verified using a thermometer. During the 72 hour testing period, the temperature was periodically checked to insure that it

remained within 1°C of the desired temperature. Two test samples were run simultaneously in an effort to improve the accuracy of the CPT test.

The initial testing temperature was determined using an equation as defined in ASTM G48-97[60] as seen below,

$$CPT = (2.5 \times \% Cr) + (7.6 \times \% Mo) + (31.9 \times \% Ni) - 41.0.$$

In the case of AL-6XN, the calculated CPT based on chemistry was approximately 65°C. This temperature was used as the initial testing temperature for the as-received plates. The initial temperature for the FS welds, however, was lowered to 55°C considering that heavily deformed structures are more prone to corrosive attack. If no pitting occurred at the initial testing temperature, the unattacked samples were re-ground, cleaned and allowed to passivate again. The testing temperature was increased by 5°C and samples were immersed in a new test tube of the ferric chloride solution for 72 hours. This process continued until pitting occurred. On the contrary, if samples pitted during the initial test, the temperature was decreased by 5°C and completely new samples were used.

After testing, the samples were cleaned with a nylon bristle brush using soap and water and then ultrasonically cleaned in acetone. To determine if pitting occurred, visual inspection was performed with the naked eye, a stereoscope, and a light optical microscope. After inspections, some samples were probed with a sharp instrument to reveal the extent of sub-surface pitting. The quality of the 120 grit surface was rough and sometimes created "pit-like" artifacts. Any questionable feature was examined at high magnification to confirm if it was an artifact of the surface finish or if the feature was

actually a pit. During some trials both samples were attacked while in other trials only one sample was attacked. For the purposes of this work, pitting was considered to have occurred when at least one sample exhibited pitting. It should be noted that samples of the advancing side contained a void defect that exposed the interior of the weld which may have created a site for crevice corrosion. When evaluating samples, only surface attack was considered and attack within tunnel was disregarded.

3.3.2 Pitting Kinetics

Although CPT testing provides a way to rank the pitting resistance for materials, the kinetics of pitting may provide insight to the details of pit growth and initiation. Kinetics experiments were run using a similar immersion technique as used for CPT testing. For kinetics experiments, samples were slightly larger to accommodate the area of the full FS weld and were approximately 35 x 3 x 6.35 mm in size. All samples were sectioned using a high speed saw and then ground and polished to a 0.05 μm surface finish on all sides, Figure 3-3. The very fine surface finish was necessary to observe very small pits, retrieve accurate data, and determine pit initiation sites and pit growth patterns with respect to microstructure. After polishing, samples were cleaned in acetone and allowed to passivate for 24 hours. The samples were immersed in a 6% ferric chloride solution at a desired temperature for times of 2, 5, 10, 20, 30, and 60 minutes. The test temperatures were chosen with respect to the CPT of AL-6XN plate to illustrate severe pitting (a test temperature of 95°C) and mild pitting (a test temperature of 70°C). A summary of the test samples is given in Table 3.1.

After testing, all of the samples were analyzed to determine several aspects of pitting behavior including pit growth rate, pit depth distribution, and pit density. The pit depth was measured using a LOM method of focusing on the sample surface surrounding the pit and then focusing on the base of the pit. Using this technique, 30 pits were measured at random to determine the pit depth distribution. To track pit growth as a function of time, the average maximum pit depth was determined by recording the depth of the 10 largest pits on the sample while the absolute maximum pit depth was recorded as the largest of these 10 pits. It should be noted that there is some amount of error in this measurement method. Pitting in stainless steels has been shown to have an undercutting type of morphology[30]. Quite often, the deepest part of the pit may be concealed and the true pit depth cannot be measured. The pit density and the pit area were determined using LOM interfaced with LECO IA3001 image analysis software. In addition, samples were etched using 10% oxalic acid and analyzed using LOM and SEM to relate pitting behavior to the microstructure. For the SEM analysis, a XL 30 operating at an accelerating voltage of 20 keV was used.

3.3.3 Electrochemical Pitting Behavior

In addition to CPT and kinetics testing, electrochemical corrosion testing was performed by Kennedy Space Center in Cocoa Beach Florida. Two types of tests were performed – a galvanic potential test in the laboratory and an open circuit potential (OCP) test in the field.

3.3.3.1 Galvanic Testing

Corrosion testing was performed to establish if a galvanic potential existed between two chosen samples when electrically coupled. Three different metal-metal junctions were tested, Table 3.2. All of the samples were ground to a 600 grit surface finish, cleaned in acetone, and allowed to passivate for at least 24 hours prior to testing. Using an EG&G flat cell, the two desired specimens were electrically coupled and exposed to a 3.55% NaCl/DI water solution. The samples were also connected to a zero resistance ammeter to record current between the two materials. Current measurements were collected every 0.1 seconds over a period of 500 seconds. This procedure was performed three times for each of the metal-metal junctions.

3.3.3.2 Open Circuit Potential

OCP tests were performed to observe long-term pitting behavior in natural seawater. For this experiment a variety of materials, in addition to the FS weld were tested, Table 3.3. As stated, the FS welds were produced using a travel speed of approximately 0.847 mm/sec (2 in./min), a tool rotational speed of 150 rpm, and a z-axis load of approximately 80 kN (18000 lb_f). Both the autogenous and dissimilar metal welds were made using a current of 275 Amp, a travel speed of 2 mm/s and an arc gap of 2.5 mm. For the dissimilar metal weld, IN 622 wire with a diameter of 0.035" was fed into the weld pool at a rate of 190.5 imp. The welding parameters of the dissimilar metal

weld were chosen based on previous work performed at Lehigh University to result in a dilution of 50%[69]. The actual measured dilution, however, was ~39%.

All of the prepared samples were approximately 6.6 x 9 cm^2 and had a milled surface finish with the exception of the AL-6XN autogenous and dissimilar metal welds. Since milling was not possible for these samples, the weld affected surfaces were wire brushed to create a smooth as possible finish comparable to the milled samples. All sample edges and corners were ground to an 80 grit surface finish using a belt grinder. At KSC, a hole was drilled in each specimen to attach a wire that was used to establish electrical connection between the specimen, the reference electrode, and the Gamry potentiostat. The points of electrical attachment were sealed with a marine grade epoxy to prevent a loss of connection during testing. Prior to testing, each of the specimens was cleaned in acetone, weighed, and photographed. Each specimen was inserted into a specially designed support that allowed the electrode probe to be positioned as desired, Figure 3-4A. The probe was positioned over the weld affected region for each of the different welds. The probe placement for the as-received plates of AL-6XN, 304SS and IN 625 was less critical and probes were arbitrary centered on the samples. For the OCP experiment, a silver/silver chloride reference electrode was used. The specimens, in the specially designed coupon supports, were submersed in a flowing seawater crate, Figure 3-4B. The positions, labeled 1-6, identify the samples listed in Table 3.3. This crate was then immersed in a large tank, Figure 3-4C, in which seawater is pumped in continually.

Upon immersion, the electrochemical potential of each specimen, as well as measurements of the saturated oxygen, conductivity, salinity, temperature, pH and

dissolved oxygen of the seawater were collected every 30 seconds for a period of approximately three months. At the duration of the experiment, all data was sent back to Lehigh for interpretation.

Table 3. 1 *Summary of the samples, temperature and exposure times used to investigate pitting kinetics of AL-6XN as-received plate and FS welds.*

	Temperature	Time (minutes)	Temperature	Time (minutes)
As-received AL-6XN	95°C	2	70°C	2
		5		5
		10		10
		20		20
		30		30
		60		60
FS weld	95°C	2	70°C	2
		5		5
		10		10
		20		20
		30		30
		60		60

Table 3. 2 *The three metal-metal couples tested for galvanic corrosion and the resulting equilibrium currents.*

Trial	Metals
1	AL-6XN plate / AA7075 plate
2	AL-6XN plate / AL-6XN autogenous weld
3	AL-6XN plate / AL-6XN FS weld

Table 3. 3 *The samples tested in natural seawater to investigate long-term open circuit potential and positions within the specimen tank.*

Position	Sample
1	AL-6XN autogenous weld
2	AL-6XN as-received plate
3	AL-6XN FS weld
4	AL-6XN dissimilar metal weld
5	304 SS
6	Inconel 625

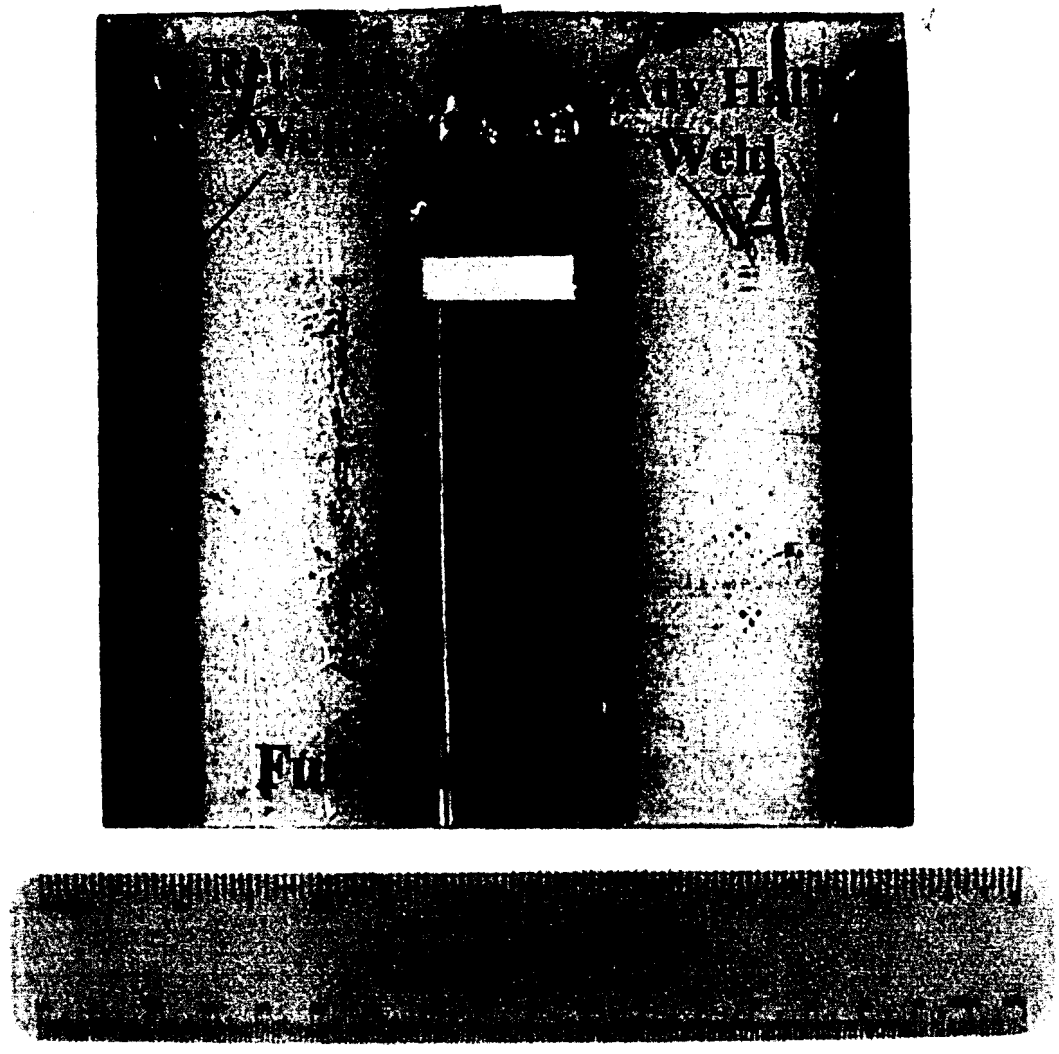

Fig. 3- 1 As-received AL-6XN plate containing a full FS weld, an advancing side half weld, and a retreating side half weld.

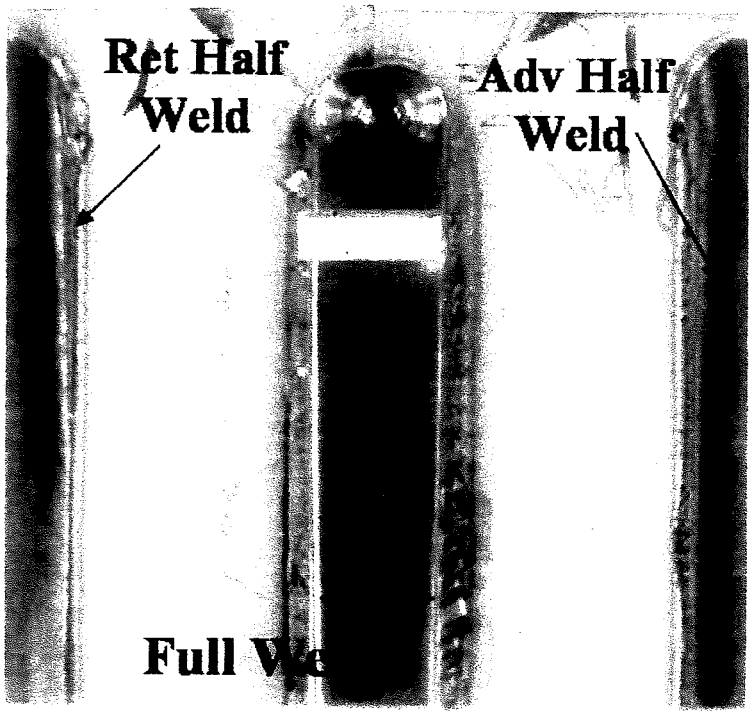

Fig. 3- 1 As-received AL-6XN plate containing a full FS weld, an advancing side half weld, and a retreating side half weld.

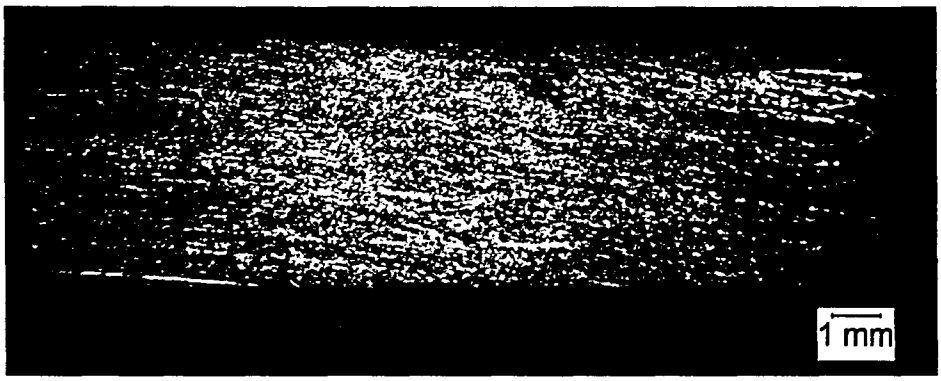

Fig. 3- 2 Representative image of all CPT samples.

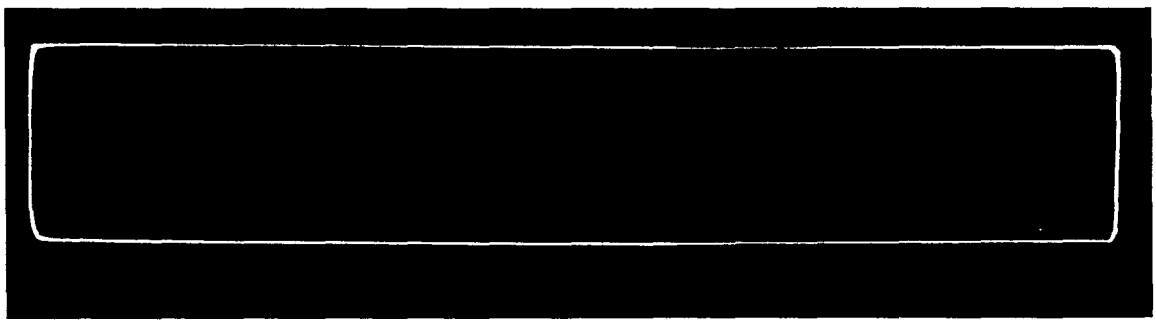

Fig. 3- 3 Representative image of all corrosion kinetic samples.

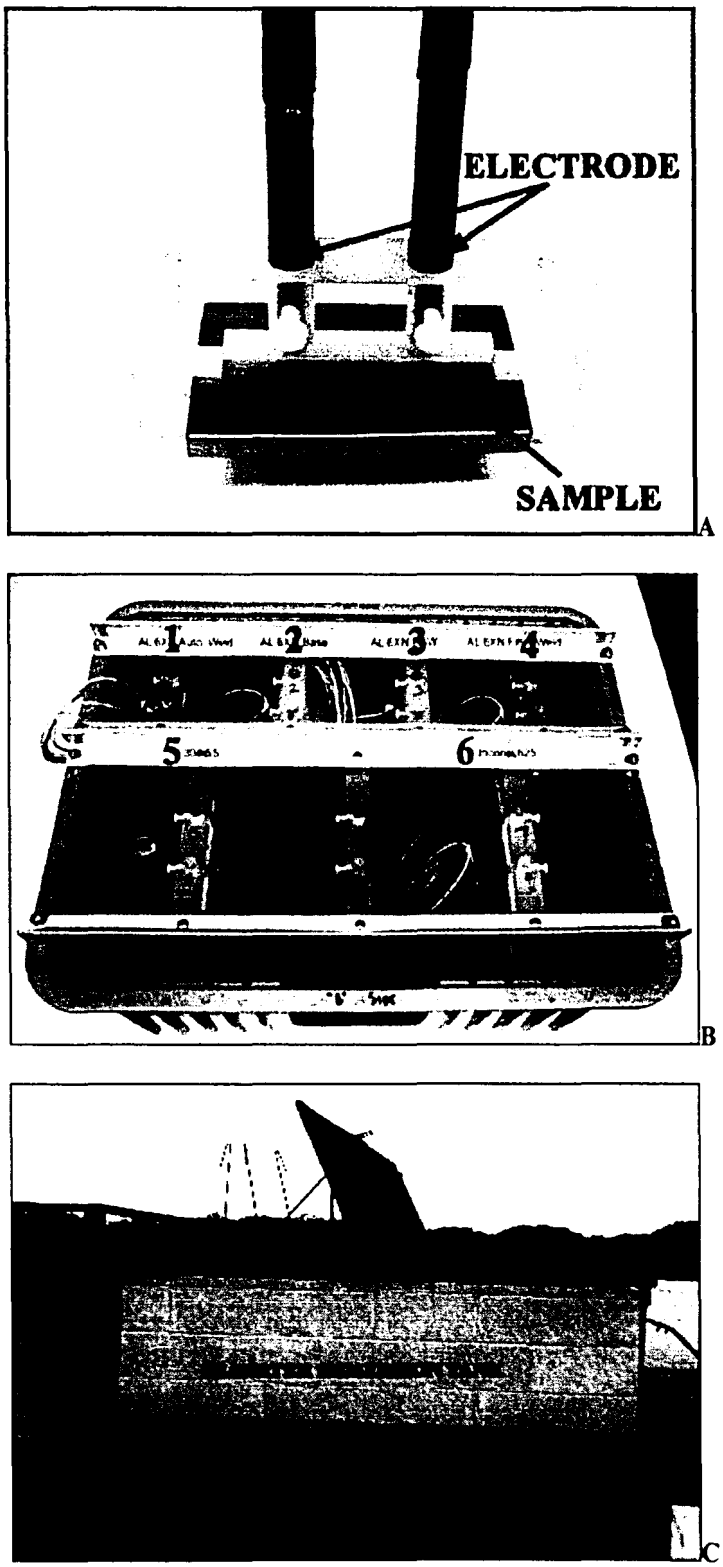

Fig. 3- 4 A) Specimen holder used during the OCP saltwater exposure testing at KSC, B) the crate in which all specimens were contained, and C) the salt water corrosion tank.

4. Results and Discussion

4.1 Double-Sided Friction Stir Weld Microstructure

4.1.1 Base-Metal

The microstructure of the AL-6XN base metal consisted of equiaxed austenite grains with annealing twins, Figure 4-1. The average grain size measured approximately 63 μm ± 5.6 μm. This is a typical microstructure for a rolled and annealed SASS. The composition of the base metal was determined using EPMA techniques. As seen in Table 4.1, the measured composition compares closely to the industrial standard for AL-6XN, with Mo and Ni slightly below the lower limits of the specification.

At higher magnifications, a second phase appearing as streaks was observed near the mid-plane of the as-rolled plate. An SEM image shows this phase is different than the rest of the base metal, Figure 4-2A. The EDS spectra of both the base metal and second phase are seen in Figures 4-2B and C, respectively. Compared to the base metal, the second phase has an increased amount of molybdenum and was previously identified in AL-6XN plate as sigma phase[27,84]. Sigma formation is promoted by microsegregation of molybdenum[70,85] and has been shown to form during solidification of SASS [64,85,26]. In the case of these AL-6XN plates, sigma likely formed at the centerline of the plate due to segregation during initial solidification of the continuous cast product and persisted during subsequent plate processing. Because sigma is a brittle intermetallic, it can be deleterious to mechanical properties of steel structures and should be avoided[86].

4.1.2 Weld Zone Microstructure

Macroscopic views of the double-sided FS weld on the AL-6XN plates are seen in Figures 4-3A and B. Figure 4-3A identifies the nugget, the TMAZ, the retreating (RET) and advancing (ADV) sides of the weld, and some notable features including tungsten swirls (as confirmed later), banding, and the crowns and root overlap of the weld. At the crown (or surface side) of both weld passes, there is a long, shallow region of affected material which is created by the pressure of the rotating shoulder against the plate surface during welding[2]. Below this shallow region, the widths of the first and second pass were approximately 11.5 and 12.7 mm, respectively. At increasing distances from the crown, the weld zone gradually becomes narrower. There is a minimum weld zone thickness of about 6.3 mm near the plate mid-plane, where the roots (or bottom sides) of the weld passes overlap. A slight asymmetry of each weld pass is seen – the retreating side has a more gradual slope than the advancing side. It is suggested that the asymmetry is created by differences in flow between the advancing and the retreating sides of a FS weld[18]. On the advancing side, the tool rotation and plate translation oppose each other causing chaotic flow and complex mixing. Flow on the retreating side, however, is generally not as complex (calmer) – material is simply deformed by tool rotation but no significant mixing takes place[9,10]. Another view of the general shape of the FS weld is seen in Figure 4-3B. In this figure, the approximate locations of the microhardness traces (Trace A-D) and the approximate lines (Lines 1-4) and areas (Area 5 and 6) on which EPMA was performed are indicated.

4.1.2.1 Nugget

As seen in Figure 4-3A, the nugget constitutes the majority of the weld affected zone. No composition change should occur since FSW is an autogenous process requiring no filler metal or flux. The average composition of the nugget, determined by EPMA, was essentially the same as the base metal, Table 4.1. In general, the microstructure of the nugget consisted of very fine grains not clearly visible using LOM. The nugget grain size was measured at several locations to contrast the ~60 μm sized grains of the base metal. The average grain size near the crown of the weld was approximately 5.9 μm ± 0.6 μm. Near the middle of the nugget, grains were slightly smaller with an average size of 5.1 μm ± 0.3 μm. Grains near the weld roots were the smallest at an average of 4.3 μm ± 0.6 μm. Decreasing grain size from the crown to the root is a trend seen in aluminum FS welds[3,13]. The pressure applied by the tool shoulder results in higher peak temperatures and longer exposure times on the plate surface, allowing for greater grain growth[3,13]. It is important to note that the thermal mechanical cycles of FSW decreases grain size by an order of magnitude.

Several distinct features are seen in the nugget. Two of the most prominent features are the swirls in each weld that extend from the advancing side of the weld beyond the centerline, Figures 4-3A and B. At high magnifications, Figures 4-4A and B, it can be seen that the swirls consist of a second phase dispersed in the nugget. Comparing the EDS spectrum from the secondary phase, Figure 4-4C, to the nugget EDS spectrum, Figure 8D, it can be seen that tungsten is detected in the swirl but is absent in the surrounding material. Although tool wear is not significant during FSW of aluminum

alloys, it can be substantial when welding harder materials. For example, during FSW of mild carbon steel using a molybdenum-based tool, wear was shown to result in molybdenum enriched regions in the weld zone[4]. In the present case, a tungsten based alloy tool was used. The temperatures and frictional forces during welding were significant enough to cause tool wear, resulting in tungsten contamination in the nugget. The location of the swirl suggests that tool wear occurs predominantly at the advancing side. There is some evidence that the advancing side may present a slightly harsher environment compared to the retreating side. First, the relative velocities of the tool and work piece are faster on the advancing side. Also, as mentioned previously, material flow is more disruptive on the advancing side because the relative directions of tool rotation and translation. It has also been reported that thermal cycles are more severe at the advancing side than at the retreating side[87].

There is no appearance of "onion rings" in the nugget as seen in some aluminum alloys[13,88] and 304 stainless steel[24], but a "banding" type of phenomenon is seen near the root overlap, Figure 4-3A. Figure 4-5A, an SEM image shows the banding at a higher magnification. In contrast to onion rings in 304 SS FS welds, consisting of alternating layers of ferrite and austenite[24], SEM images of the light and dark layers of the banding in AL-6XN reveal only differences in etching response. The microstructure of the dark layer, Figure 4-5B, consists of fine equiaxed grains. An SEM image of the light layer, Figure 4-5C, reveals a very fine microstructure which is difficult to resolve. EPMA data of Lines 1 and 2 extend through the banding at the root overlap, Figure 4-3B. A plot of this EPMA data, Figure 4-6, shows concentration of the elements in this region remained

constant. Thus, banding is not the result of composition changes. A possible explanation for the banding is the material flow occurring during FSW. When dissimilar metals are joined via FSW, the complex mixing of the two plates is obvious, as etching reveals complex swirls and intercalations throughout the weld zone[5]. When two plates of the same material are joined, however, the swirls and vortex patterns are less evident since there are no real composition differences. In this case, the subtle appearance of intercalations can be the result of variations in deformation regimes[89].

Similar to the base metal, a second phase was found near the mid-plane of the plate in the weld zone, Figure 4-7A. EDS analysis of the second phase, Figure 4-7B, again detects an increased concentration of molybdenum compared to the base metal, Figure 4-2A. Some of the second phase was also found near the edge of the nugget bordering the TMAZ, Figure 4-7C. Only a few, isolated fragments of sigma were seen in the nugget in contrast to the base metal. Before welding, the morphology of the sigma in this region most likely appeared similar to the centerline sigma in the base metal. The intense deformation and complex material flow during welding, however, broke-down the sigma and re-distributed it away from the mid-plane. It is likely that more sigma is distributed throughout the nugget but is very fine and was undetected with the LOM or SEM magnifications used in this study. It should be stressed that the sigma phase found in the nugget originated during plate fabrication and thus existed prior to the welding process. Nevertheless, from Figure 4-6, it is seen that microsegregation, which promotes sigma formation, has been avoided. Thus, it is unlikely that sigma would form during FSW.

4.1.2.2 Heat Affected Zone and Thermal Mechanical Affected Zone

As mentioned previously, the TMAZ surrounds the nugget and the HAZ surrounds the TMAZ. The HAZ consists of the same large equiaxed austenite grains seen in Figure 4-1 of the base metal. Having experienced only the thermal cycles of FSW, grain growth in the HAZ might be expected but is not evident. The difference between the base metal and the HAZ is very subtle and defining the exact boundary between them is difficult. The only distinguishing feature between the two regions is the nucleation of a fine phase at the grain boundaries in the HAZ, Figure 4-8. Posada et al[27] noted the same phenomenon in Al-6XN FS welds and suggests that it is either recrystallized grains or precipitated sigma phase[27] but no further work was performed to identify this phase.

A TEM photomicrograph of the microstructure around a grain boundary in the HAZ is shown in Figure 4-9. This image shows an original austenite grain boundary (indicated by several arrows) and the small features decorating the boundary (indicated by letters). The SAD patterns from the indicated features were obtained for phase identification and to determine their orientation relationship, Figures 4-10A-H.

The SAD pattern at region A was typical for an FCC metal oriented along the (112) plane, Figure 4-10A. Regions B-D produced similar SAD patterns with only slight orientation differences, Figures 4-10B-D. Therefore, regions identified as A-D in Figure 4-10 are subgrains, separated by only low angle grain boundaries. On the opposite side of the grain boundary, regions E-H have a similar orientation to each another, Figures 4-

10E-H, but are different than regions A-D. Again, regions E-H differ in orientation by small angles and are thus sub-grains. Although, these subgrains are not orientated along a major zone axis, their crystal structure is still revealed. The diffraction patterns of Figures 4-10E-H also show an FCC structure, not the tetragonal crystal structure of sigma. The nucleation phenomenon was also investigated at another site in the HAZ yielding similar results. From the TEM analysis, it is confirmed that the grain boundary phenomenon in the HAZ is recrystallization of austenite and not formation of the sigma phase. The driving force causing recrystallization at the grain boundaries is not clear. One possibility is that the combination of residual stress from plate processing and the specific time and temperature environment produced during FSW promoted recrystallization of austenite. It is also possible that, although this microstructure was referred to as the HAZ (implying that only temperature cycles affected the microstructure), strain may have reached the critical minimum to induce recrystallization.

The microstructure of the TMAZ is best described as a transition region from a complete HAZ microstructure to a complete nugget-type of microstructure, Figure 4-11A. The transition is a result of decreasing strain and strain rates and milder thermal cycles with increasing distance from the centerline. Because the changes from the TMAZ and HAZ zone is so gradual, the line drawn in Figure 4-11A defines only an approximate HAZ / TMAZ boundary. Near this boundary, microstructural changes of the TMAZ are mainly the result of thermal cycles – evidence of deformation is minimal here. Moving towards the right in the figure, strain caused by tool rotation begins to dominate the microstructural changes, leading to a more refined structure. As seen in Figure 4-

11A, higher strains deform the original austenite more severely and promote more recrystallization at the original austenite grain boundaries. Adjacent to the weld nugget, most of the TMAZ appears completely refined but several larger austenite grains persist.

In addition, EPMA data along Lines 3 and 4, Figure 4-3B, provided a composition analysis of the different microstructural regions. The data showed no variation in elemental concentration with distance, Figure 4-11B, and appeared essentially the same as data obtained from Lines 1 and 2, Figure 4-6. From all EPMA traces, it can be concluded that there is no form of segregation in the AL-6XN welds.

4.1.2.3 Microhardness

The average microhardness of the base metal was measured at approximately 243 HK ± 9 HK. Four microhardness traces were performed across the welded region, Figure 4-3B. Figures 4-12A, B, and C show plots of microhardness as a function of distance from the centerline for traces A, B, and C, respectively. As labeled on the plots, changes in microhardness are correlated to the microstructural transition from the base metal to the nugget. In all plots, hardness is a maximum in the fine-grained nugget region. All microstructural zones are represented in trace B, Figure 4-12B. Since the TMAZ is narrow, no data points fell within the TMAZ for trace A, Figure 4-12A, and trace C, Figure 4-12C. Despite this, it can clearly be seen that hardness decreases with increasing distance from the weld centerline. As mentioned above, the TMAZ consists of a mix of deformed austenite grains and small nucleated grains at grain boundaries. In general, this microstructure yields hardness values similar to, but slightly lower than the nugget. The

large austenite grains and small nucleated grains of the HAZ yield a range of hardness values between the TMAZ and base metal hardness. In general, the TMAZ and HAZ, both transition zones separating the nugget and the base metal, show a trend of decreasing hardness moving away from the nugget. These two zones exhibit considerable scatter in the data – a result of the nature of the microstructure and of microhardness testing.

Trace D was taken through the plate thickness near the weld centerline, Figure 4-3B. Figure 4-12D shows a plot of microhardness measurements as a function of distance from the mid-plane of the plate. The two maximum data points correspond to the microhardness of the tungsten swirls in the microstructure. There is, however, no other clear relation between hardness and the through-thickness plate location.

4.2 Microstructure of the Single-Sided Friction Stir Weld

The microstructures of the AL-6XN single-sided FS welds were very similar to the double-sided FS welds analyzed. A representative image of both full FS welds, Figure 4-13, shows the single-sided weld has a similar u-shape as one pass of a double-sided FS weld. As mentioned in the procedure, the received weld plates each contained two half welds. Figures 4-14A and B show the advancing and retreating side half welds on plate 1 while 4-14C and D show the advancing and retreating side half welds on plate 2. It appears that the half welds on plate 1, Figures 4-14A and B, did not achieve full penetration.

4.2.1 Base Metal Microstructure

The base metal of both plates consisted of equiaxed austenite grains with significant twinning, Figure 4-15. The grain size of plates 1 and 2 were approximately 50.1 μm ± 4.2 μm and 51.1 μm ± 5.0 μm, respectively. Again, centerline sigma existed in both plates examined. The morphology of sigma varied with location in each plate but in general, there was less sigma in plate 1 compared to plate 2. In plate 2, the sigma decorated the grain boundaries and formed wide bands throughout the length of the plate, Figure 4-16A. The sigma in plate 1 formed much thinner bands which were located only sporadically through the plate length, Figure 4-16B. Some samples from plate 1 were even sigma free.

4.2.2 Weld Affected Microstructure

The same strain and temperature induced microstructural transition from the nugget to the base metal of the double-sided weld was seen in the single-sided welds. The nugget consisted of small somewhat equiaxed grains, Figure 4-17A. Grains were approximately 12.8 μm ± 1.1 μm near the crown and 9.8 μm ± 0.7 μm near the center of the nugget in plate 1. Grains in plate 2 were of similar size measuring 11.1 μm ± 0.5 μm near the crown and 9.5 μm ± 0.7 μm at the nugget center. As mentioned before, larger grain size at the crown results from the higher peak temperatures and longer exposure times. The two transitional zones, the HAZ and the TMAZ, Figures 4-17B and C respectively, show the microstructural effects of the strain and temperature gradients occurring during welding. The HAZ, again, consists of large original austenite grains with nucleation of new austenite grains at the existing grain boundaries, Figure 4-17B.

Not surprisingly, the TMAZ is characterized by a mix of deformed original austenite grains and nucleation at grain boundaries, Figure 4-17C.

4.2.3 Differences Between the Single-Sided and Double-Sided Friction Stir Weld

Although microstructurally similar, there are some notable differences between the double- and single-sided welds besides the obvious. The advancing half welds of both plates 1 and 2, Figures 4-14A and C, contain a large hole. This hole is only a segment of a tunnel (referred to as a worm hole) which spans the length of the weld. A worm hole results from incomplete material consolidation and can be eliminated with optimization of welding parameters. Another difference between the single- and double-sided welds is the distribution of tungsten within the nugget. The tungsten in the double-sided welds is mainly concentrated around on central streak in the nugget running parallel to the plate surfaces, Figures 4-3A and B. Tungsten in both single-sided welds, however, shows an elaborate streaking pattern throughout the nugget, Figures 4-18A and B.

Despite the differences, the microstructures and macrostructures of both the single- and double-sided FS welds are very similar. The notable differences in the structures are likely caused by the required penetration depth. On a plate of a given thickness, the required penetration depth of a double sided-weld is essentially half of the required depth of a single-sided weld. Therefore, more energy is required to successfully join two plates of a given thickness with a single-sided FS. Under different welding parameters, the weld defects in the single-sided FS welds may be avoided.

4.2.4 Planar Cross-section Microstructure

The crown surface of a single-sided weld was also examined revealing a similar microstructure as seen in the cross-section of the FS welds. Again, there was a transformation from the unaffected base metal through the HAZ and the TMAZ to the refined nugget, Figure 4-19A. The microstructural transition, however, was more abrupt at the crown surface than seen in transverse cross-section. In some samples, an interesting banding pattern was noted, Figure 4-19B. A high magnification SEM image, Figure 4-19C, reveals a second phase similar to the tungsten detected in the transverse cross-section of the FS welds. EDS examination, Figure 4-19D, confirmed high levels of tungsten in the second phase creating this banding. Again, the tungsten contamination results from tool wear during the welding process.

4.3 Corrosion Behavior

4.3.1 Critical Pitting Temperature

As mentioned, the CPT was determined by immersion in ferric chloride solution according to ASTM G-48-97[60]. The CPT was determined for five samples: AL-6XN as-received plate and the retreating and advancing side half welds on plates 1 and 2. Table 4.2 lists all CPT test samples and their respective CPT. AL-6XN as-received plate was tested to determine a baseline in which to compare the FS welds. The advancing side and retreating sides of the welds were tested separately to determine any differences in pitting behavior. It might be expected that the advancing side half welds have a lower corrosion

resistance than the retreating side half welds because of the worm hole and the tungsten based inclusions.

4.3.1.1 AL-6XN As-received Plate

It should be noted that "pitting" occurred when localized attack was detected with the naked eye or a stereoscope. The CPT of AL-6XN plate was 70°C, Table 4.2, which is consistent with other literature[76]. The attack at 70°C was not severe – the samples showed a few isolated pits that were less than 1 mm in diameter, Figures 4-20A and B. A number of pits showed evidence of undercutting which is often noted in the corrosion behavior of stainless steels[46]. In Figure 4-20C, an SEM image of a pit formed in the base metal, a thin layer of metal partially conceals the volume of the pit. It might be expected to see preferential pitting at centerline sigma but there is no obvious correlation between the sigma phase and pitting. In general, pits in the AL-6XN as-received plate were randomly located.

Prior to etching, pit surfaces showed two different morphologies. Some pits surfaces had a clear faceted structure, Figure 4-21A. This morphology suggests preferential grain boundary attack and possibly material loss by a wastage mechanism. Other pit surfaces, however, had a finer dimpled surface, Figure 4-21B, which may be a thin layer of corrosion product[90]. Some pits exhibited one surface while others showed a mixture of the two morphologies. Although CPT testing cannot be used to determine pit initiation sites, it may indicate pitting mechanism. High magnification images of the edge of a pit in the as-received plate suggest preferential attack at the grain boundaries.

Figure 4-21C. Preferential attack at the grain boundaries is often noted in the corrosion of stainless steels[50].

4.3.1.2 AL-6XN Advancing Half Welds

The advancing side half welds of plate 1 and 2 both exhibited pitting at 55°C but resisted attack at 50°C yielding a CPT of approximately 55°C, Table 4.2. This is significantly lower than the as-received plate CPT of 70°C. Several examples of the pitted samples are seen in Figures 4-22A-C. For all samples, the attack was concentrated at the worm hole and the surrounding area where a steady stream of tungsten based inclusions is located, Figures 4-22A and B. The severe attack seen at the surface is most likely the result of crevice corrosion in the worm hole. The interface of the AL-6XN matrix and the tungsten inclusions may provide an initiation site or an easy propagation path for corrosion. One sample pitted on the crown side of the weld, Figure 4-22C. As mentioned in the microstructural characterization, tungsten inclusions are located at the crown as well. Again, the tungsten inclusions may serve as a pit initiation site.

4.3.1.3 AL-6XN Retreating Half Welds

The CPT of the retreating side half welds were different in plates 1 and 2, Table 4.2. In all retreating side half welds, the attack was not severe – there were a number of relatively small isolated pits. The CPT of the retreating half weld on plate 1 was 65°C, only slightly lower than the CPT of the as-received plate. It is interesting and significant to note that the pits in the retreating side half weld on plate 1 were located in the base metal, Figure 4-23A. The base metal attack suggests that the pitting behavior of

the as-received plate and the retreating side half weld is very similar. This difference may be the result of the nature of the CPT test.

The CPT of the retreating side half weld on plate 2 was 55°C – the same CPT as the retreating side, Table 4.2. In these tests, only one sample exhibited pitting. On this sample, a single elongated pit was located at the plate centerline where sigma has been shown to exist, Figure 4-23B. SEM images of the pit reveal two slightly different morphologies within the pit, Figure 4-23C. The EDS spectrum of region 2, Figure 4-23D, detects an increased Mo-concentration compared to the base metal, Figure 4-4D, and this second phase is most likely sigma. Because the pit was destroyed during metallographic preparation, the microstructural location of the pit could not be determined. For this sample, preferential pitting at sigma was a factor.

The difference in pitting behavior between the retreating side half welds on plate 1 and 2 may likely be related to the difference in the amounts and distributions of the sigma phase, Figures 4-16A and B. It has been shown that the corrosion resistance of SASS is sacrificed by the presence of the sigma phase and is likely the case for this sample[50,63]. Again, most pit surfaces showed the typical morphology as previously noted in the as-received plate and the advancing side half welds.

4.3.1.4 Improving the CPT

With the exception of the retreating side half weld on weld plate 1, the CPT of all half welds was 55°C. From the tests, it seems that the pitting resistance of the weld is severely sacrificed by the presence of certain avoidable microstructural features. In the

case of the advancing side half welds, elimination of the worm hole – a natural site for crevice corrosion – should have a positive affect on the pitting resistance of the weld. In addition, removal of the tungsten based inclusions, which may promote pitting, should also help to improve the corrosion resistance.

For experimental purposes, the CPT of the AL-6XN FS welds should be considered to be 55°C even though the retreating half weld of on plate 1 had a higher CPT. As shown by previous work at Lehigh University under ONR Grant No. N00014-99-1-0887[84], the CPT is approximately 45°C for AL-6XN autogenous welds. Dissimilar welds made with IN 622 filler metal yielded an increased CPT of 55°C. From CPT data, it appears that FS weld has similar corrosion resistance to the compensated dissimilar weld. It is significant to remember that one FS weld sample, the retreating half weld on plate 1, had a CPT of 65°C. It may be possible to improve the CPT to 65°C for the FS welds if sigma is minimized and the worm hole and tungsten based inclusions are avoided.

Several points should be stressed when reporting the CPT. Although the testing performed helps to determine differences in pitting behavior between the retreating and advancing side, only an *estimation* of the CPT of the full weld can be made. In reality, half welds would not be exposed to the environment. Actual full welds should be tested for a more accurate determination of the CPT but due to limitations in material availability, it was not possible. Also, undesirable microstructural features significantly influence the CPT, making it difficult to determine the true pitting resistance of the FS weld. In addition, all surfaces of the welds – planar as well as transverse cross-sections –

were exposed to the corrosive solution. In reality, it is unlikely that the transverse cross-section of the weld, which pitted most frequently, would be exposed to the environment. All surfaces were ground to 120 grit surface, also not the realistic case. Regardless of the drawbacks of the test procedure, the CPT of AL-6XN FS welds was determined. When using the CPT to compare the pitting behavior of a FS weld to other materials, however, the above points should be considered.

4.3.2 Pitting Kinetics

Kinetic testing was performed on AL-6XN as-received plate and FS welds in 6% ferric chloride solution at 70°C and 95°C. The maximum pit depth can be modeled by the following equation

$$d = kt^n$$

where
d = maximum pit depth
t = time
k and n = alloy and environment dependent constants.

The n-constant relates pit depth to time and it has previously been determined that n is 0.5 or 1 for mild carbon steel and 0.75 for stainless steels[91]. It should be noted that these n-constants were obtained using a different corrosive media and much longer testing times so they are not directly comparable to the results in this study. The *absolute* maximum pit depth (the single deepest pit) and the *average* maximum pit depth (an average of the 10 deepest pits) were recorded. Ultimately the deepest pit leads to failure but using the average maximum pit depth is more accurate and precise.

4.3.2.1 Severe Pitting - 95°C

4.3.2.1.1 Pit Growth Rate

Tables 4.3 and 4.4 list the 10 deepest pits found in AL-6XN plate and the FS welds for the various exposure times at a test temperature of 95°C. Tables 4.5 and 4.6 compare the *absolute* maximum pit depth and the *average* maximum pit depth for these samples. The maximum depths of the as-received plate and the FS compare closely at each exposure time and neither material consistently yields the deepest maximum pit.

When the raw data is plotted on a linear scale, Figure 4-24A, the average and the absolute maximum pit depth in samples tested at 95°C follows a logarithmic growth pattern. A plot of the natural log of the pit depth as a function of the natural log of time yields a straight line, Figure 4-24B. The slope of which, n, yields an approximation of pit growth rate. Using the absolute maximum pit depth, n_{abs} (calculated n value for the *absolute* pit depths) was approximately 0.47 for the as-received plate and 0.42 for the FS weld. Although it appears that the pitting rate is slightly higher for the as-received plate, the difference in the respective n_{abs} is experimentally insignificant and the pit growth rates are essentially equal. Using the average maximum pit depth, n_{ave} (calculated n value for the *average* maximum pit depths) was approximately 0.40 for the as-received plate and 0.45 for the FS weld. It is interesting to note that the pit growth rate of the as-received plate is higher than the FS weld but, again, the difference in n_{ave} is insignificant and should be disregarded. Due to the intense deformation and strain, it might be expected that pits grow faster in the FS welds. From this data, however, is appears that

the pit growth rates in as-received plate and the FS welds are relatively equal. Therefore, in regards to results of the kinetics corrosion test, AL-6XN FS welds may offer superior corrosion resistance compared to AL-6XN fusion welds. It is important to remember that the kinetics tests were performed using a very corrosive ferric chloride media and only short exposure times. This test is, therefore, not a realistic approximation to the in-service environment of AL-6XN FS welds.

4.3.2.1.2. Pit Depth Distribution and Density

Figures 4-25A-F and 4-26A-F, show the general pit depth distribution in the as-received plate and the FS weld tested at 95°C for the various exposure times. When comparing the as-received plate and the FS weld distributions, they are very similar. In general, as time passes, the histograms tend to "spread out". At times of 2 minutes, Figures 4-25A and 4-26A, there is a tighter distribution of pit depths than seen at a time of 5 minutes, Figures 4-25B and 4-26B. At 60 minutes, Figures 4-25F and 4-26F, the distribution broadens even further. In most histograms, regardless of exposure times, 60% of the pits measured are less than 50 μm deep. As time increases a small number of pits begin to deepen, surpassing depths of 100, 200, and eventually 300 μm. The concentrated attack at these growing pits may provide cathodic protection for the surrounding smaller pits which do not deepen significantly. Therefore, the number of shallow pits remains high[91]. In addition, because new pits are continually nucleating as time passes, it would be expected that the majority of pits are shallow. From the

similarity in pit depth distribution, there is no clear difference between the as-received plate and the FS weld.

The average pit density of the FS weld and the as-received plate, Figure 4-27, has no correlation to the exposure time. As seen, the average pit density in the FS weld ranges from 3 – 6 pits/mm^2 and average pit density in the as-received plate ranges from 4 – 6 pits/mm^2. The pit density is greater for the as-received plate in all but the 60 minute exposure samples. The difference between the densities at each exposure time, however, are small – typically less than 1 pit/mm^2. This difference is within experimental error and should be disregarded. Similar to the pitting rates and depth distributions at 95°C, the pit density suggests no real difference in corrosion behavior of the two materials.

4.3.2.1.3. Pitting and Microstructure

When etched, the kinetics samples reveal an unexpected preference for pit growth in the base metal as opposed to the weld affected region in the FS welds. Figures 4-28A, B, and C show the FS weld at 2, 5, and 60 minutes. At 2 minutes, Figure 4-28A, there are only small pits. At 5 minutes, Figure 4-28B, pits are larger and more frequent in the base metal than in the weld zone. After 60 minutes, Figure 4-28C, the preference for pits to grow in the base metal is emphasized even further.

Considering this preference for the deepest pits in the base metal, the prior calculation of pit growth rate for the FS weld is actually an estimation of the pit growth rate in the base metal not the weld. The pit growth rate for the actual weld affected region is slower. As discussed in the literature, 304 SS showed a tendency to

preferentially corrode at highly deformed regions[56]. Although FSW involves extreme strains, the resulting microstructure is relatively low in strain. The intense deformation and thermal cycles during FSW cause nucleation of *strain-free* austenite grains. Therefore, the preferential corrosion phenomenon seen in 304 SS, is not seen in AL-6XN FS welds.

The base metal, having a uniform structure, showed no preference for pit initiation. Figures 4-28D, E, and F show the as-received plate tested at 95°C for 2, 5, and 60 minutes respectively. At 2 minutes, Figure 4-28D, there are a number of small pits, indicated by arrows, located over the whole sample. At 5 minutes, Figure 4-28E, the pits have grown in size and are more visible. At a 60 minute exposure time, Figure 4-28F, the pits which have grown substantially are randomly located.

There are obvious differences in the pitting behavior of the as-received plate and the FS weld from the kinetics tests. The combination of the refined weld structure and the unaffected base metal forces preferential corrosion of the base metal while the weld zone is cathodically protected. It seems that there is a galvanic type of corrosion occurring in the FS weld samples.

4.3.2.2 Mild Pitting - 70°C

4.3.2.2.1 Pit Growth Rate

Tables 4.7 and 4.8 list the ten deepest pits in the as-received plate and the FS weld tested at 70°C respectively. Tables 4.5 and 4.6 compare the absolute maximum and the average maximum pit depths for the kinetics samples tested at 70°C as well as 95°C.

Figures 4-29A and B show the maximum pit depth plotted as a function of time for the AL-6XN FS weld and for the as-received plate tested at 70°C. Similar to the results of testing at 95°C, the absolute and average maximum pit depth for the FS weld increases logarithmically with time, Figure 4-29A. Again, the pit depth shows a linear dependence with time when the natural log of the data is plotted, Figure 4-29B. In this case n_{abs} = 0.58 and n_{ave} = 0.54 for the FS weld. Referring back to the calculated n values for the FS weld tested at 95°C, n_{abs} = 0.47 and n_{ave} = 0.45. The pitting rate at 70°C is slightly higher than experienced at 95°C. As will be discussed, the higher pitting rate at the lower temperature is logical

The AL-6XN as-received plate tested at 70°C does not show the same pit depth dependence on time as seen in the other samples. For the first five data points (times of 2, 5, 10, 20 and 30 minutes), pit dept does not significantly change with time, Figure 4-29A and Table 4.5. But from 30 minutes to 60 minutes, the absolute maximum pit depth jumps from 56 μm to 267 μm. From a plot of the logarithmic values of the data, Figure 4-29B, n_{abs} = 0.42 and n_{ave} = 0.24. The poor linear fit of the data is revealed by the low R^2 values calculated for the trend lines of the as-received plate data tested at 70°C. For this test, R^2 was approximately 0.44 when other tests yielded R^2 values approaching unity. From the raw data plot, Figure 4-29A, the pit depth and exposure time for the AL-6XN plate show exponential growth as opposed to logarithmic growth. Additional tests of the AL-6XN plate at 70°C were run for exposure times of 30 and 60 minutes to check the accuracy and precision of the data. The absolute maximum pit depth after 30 minutes was 72 μm which is similar to the results of the initial test which yielded a maximum of

depth of 56 μm. At 60 minutes the maximum pit depth was 124 μm, less than half of the pit depth recorded in the initial test.

Since 70°C is the CPT of the AL-6XN plate, the driving force behind pit growth may be minimal and may be the reason why the AL-6XN shows sporadic behavior at this temperature. By this reasoning and the previous similarity in pitting behavior at 95°C, it might be expected that the FS weld should have behaved similarly to the as-received plate tested at 70°C. As discussed, some type of galvanic corrosion may have occurred in the FS weld sample such that the base metal corroded preferentially to the weld zone when tested at 95°C. At 70°C this galvanic junction on the FS weld sample is the driving force for pit growth. As for the as-received plate, there is no galvanic junction to force corrosion and pit growth is minimal. Another possibility is the questionable test precision which was demonstrated by the additional testing at 70°C. At this time, further work is required to investigate the kinetics of the AL-6XN as-received plate at 70°C.

4.3.2.2.2 Pit Depth Distribution and Density

Figures 4-30A-C, show the pit depth distribution of the FS weld tested at 70°C for the times of 2, 5 and 60 minutes. The pit depth distribution of the FS weld tested at 70°C shows a similar "spreading out" behavior as seen at 95°C with a small number of pits deepening significantly while most pits remain shallow. Figures 4-31A and B show the general pit depth distribution of the AL-6XN plate tested at 70°C for exposure times of 2 and 60 minutes. Although, these histograms show a broadening in the pit depth distribution from 2 to 60 minutes, it is not as evident as seen in other samples. At 2

minutes, the majority of the pits (97%) are 30 μm or less, Figure 4-31A. At 60 minutes, Figure 4-31B, just 4 pits measured were deeper than 30 μm, only two of which were deeper than 100 μm. These results further reflect the abnormal pitting behavior of AL-6XN plate at 70°C.

Again, the average pit density of the FS weld and the as-received plate, Figure 4-32, show no correlation to the exposure time. Pit densities of the two materials are similar where the average pit density ranges from 1 – 3 pits/mm^2 in the FS weld and from 1 – 2 pits/mm^2 in the as-received plate. As opposed to the 95°C test, the FS welds have a greater pit density at this lower temperature. Again, the differences in pit density at each exposure time are within experimental error and should be disregarded. Also, it is important to remember that the pitting behavior of the as-received plate was abnormal and the results may not be a good indicator of the true pitting behavior. The pit densities are notably lower at 70°C, Figure 4-32, than at 95°C Figure 4-27. At lower temperatures, the passive film is more stable and it is harder for pits to nucleate. Since fewer pits initiate at lower temperatures, attack is concentrated at these pits and corrosion rates, n, are faster for samples tested at 70°C[91]. It is important to note that data was acquired from only one sample at each test condition. For a better estimation of the maximum pit depth, data from more samples is necessary. Again, due to the limited material availability more samples were not possible.

4.3.2.2.3 Pitting and Microstructure

Kinetic samples of the FS weld tested at 70°C for an exposure time of 2 minutes were etched and analyzed to determine the pit initiation sites. Pits initiated throughout the sample in both the base metal and FS weld. In the base metal, small pits were found at grain boundaries, Figure 4-33. In the HAZ, a region similar to the base metal, many pits appeared to have initiated at the grain boundaries as well, Figure 4-34A. A low and high magnification SEM image of two pits in the HAZ, Figures 4-34B and C, again shows the preference for pits to initiate at grain boundaries. In the TMAZ, there was some evidence of pit initiation at the grain boundaries. Figure 4-35A shows one large and several very small pits located in the TMAZ. A higher magnification of the two smaller pits along the grain boundary is shown in Figure 4-35B. Due to the response in etching, pit initiation sites in other regions of the TMAZ cannot be clearly identified. The etching response was also a problem in the nugget. At the regions in the nugget where the microstructure was visible, some larger pits were imaged using LOM, Figure 4-36A. These pits were so large compared to the microstructure that pit initiation cannot be determined. Using SEM, some small pit-like features were found at the grain boundaries, Figure 4-36B. Although these features look like pits, they are so small it is possible that they are artifacts of metallographic preparation.

Since there is no obvious preference for pit initiation in any one of the microstructural regions (base metal, HAZ, TMAZ, and nugget), it might be expected that pits tend to initiate in the same manner regardless of microstructure. Evidence of pit initiation consistently at the grain boundaries confirms this, Figures 4-33, 4-34A-C, and

4-36B. With respect to the microstructure of the welded and as-received plates, grain boundaries are the sites of highest energy and are therefore attacked preferentially. Although the worm hole, tungsten base inclusions, and sigma phase were features associated with corrosion in CPT testing, there was no clear preference for initiation at these features in the kinetic tests. The worm hole in the CPT samples was relatively large, reaching sizes of 1 mm in diameter, Figure 4-14A and C. Kinetic samples, however, contained a few worm holes an order of magnitude smaller in size. The extremely small size of the worm holes in the FS weld appears to prevent the crevice corrosion seen in the CPT samples. Preference for attack at the tungsten based inclusions may be related to the worm hole. Although the interface between AL-6XN and the inclusions may be an easy path for corrosion, it only seems to be significant when attack is first concentrated at the worm hole. When there is no attack at the worm hole, the inclusions show no preference for attack. Also, the difference in exposure times for the CPT and kinetics tests may also play a role. CPT testing lasted 72 hours while the longest exposure time in kinetics testing was 60 minutes. At the long exposure times of the CPT test, the grain boundary attack seen in the kinetics tests is minimized by the concentrated attack at the worm hole.

As the AL-6XN plate has the same structure as the base metal in the FS weld samples, it would be expected that grain boundaries serve as pit initiation sites. The small pits in the as-received plate were found at grain boundaries. Figure 4-37 shows a small pit in the as-received plate that appears to have initiated at the intersection of two grain boundaries and a twin. Therefore, in kinetic testing, the as-received plate and the

FS welds showed the same pit behavior. In both samples regardless of microstructure, pits initiated at the grain boundaries.

The welds and as-received plate showed similar pit propagation mechanisms at 70°C at extended exposure times. Figure 4-38A shows a large pit formed in the base metal after 60 minutes. As indicated, grain boundaries are preferentially attacked. This has been noted as the typical corrosion behavior of stainless steels. Pits in the weld zone showed some preference for propagation along grain boundaries. In Figure 4-38B, the large pit partially in the TMAZ and HAZ does not show an obvious pit propagation preference. Another pit in the TMAZ, Figure 4-38C, however, shows pit propagation along grain boundaries. As discussed before, although pits may initiate at the sigma phase, there was no strong preference for pits to initiate here versus other spots in the microstructure. Once initiated at the sigma, pits propagate either at grain boundaries of two austenite grains or at the sigma phase/austenite interface, Figure 4-38D. Even though some aspects of pitting behavior were unique for the as-received plate, pit propagation was still similar as seen in the weld. Pits of the as-received plate primarily propagated along the grain boundaries of the austenite grains, Figure 4-39. Propagation of pits, either in the as-received plate or the FS weld, occurs by the same mechanism – attack at the grain boundaries. Again, the grain boundaries are high energy sites.

4.3.3 Pitting Electrochemistry

4.3.3.1 Galvanic Potentials

When two metals are electronically coupled, a current may exist between them and one metal will corrode at the expense of the other. As stated, three different metal-metal couples were evaluated to determine if galvanic corrosion would occur, Table 3.2.

Initially, a galvanic test was performed on AL-6XN as-received plate coupled to 7075 aluminum. Referring to the Galvanic series, Figure 2-32, aluminum is more active with respect to common stainless steels such as type 316 and 304 and will thus corrode preferentially. Since the corrosion resistance of AL-6XN is superior to 316 and 304 SS, it is expected that the 7075 aluminum alloy is also active compared to AL-6XN. The equilibrium galvanic potential ranges from 30-35 $\mu A/cm^2$, Figure 4-40A, and indicates that aluminum will corrode at the expense of the AL-6XN. By default, the Gamry potentiostat follows the corrosion convention in which positive currents are anodic and negative currents are cathodic

It is known that the corrosion resistance of autogenous welds on SASS is poor and the weld zone will be preferentially attacked. The results of the galvanic test between the AL-6XN autogenous weld and the as-received plate couple, Figure 4-40B, shows an equilibrium current ranging from $100 - 250\ nA/cm^2$ in all three trials. Again, the positive current indicates that the weld is the anode and it will preferentially corrode as expected. The current and therefore the driving force for galvanic corrosion is over 2 orders of magnitude smaller in this couple than the aluminum-AL-6XN couple.

Three trials indicated that a positive current also existed between the AL-6XN as-received plate and the AL-6XN FS weld, Figure 4-40C. The equilibrium current for this couple remains less then 5 nA/cm^2 indicating a low driving force for galvanic corrosion. It is more important to note that the magnitude of this current is easily within the experimental error of electrochemical testing and should be disregarded. These results differ with the kinetics testing where the base metal was seen to corrode at the expense of the weld region of the FS welds. The difference is most likely the result of changing pitting behavior with different test electrolyte. The NaCl solution may be a closer approximation to the marine environment when compared to a ferric chloride solution and it can be concluded that galvanic corrosion is unlikely in a realistic environment.

4.3.3.2. Open Circuit Potential

All data thus far has been acquired in a laboratory using a superficial electrolyte to simulate a marine environment. The open circuit potential (OCP) test performed in open seawater is a more realistic simulation. Also, compared to laboratory testing, the OCP experiments run for a much longer time period – 150 days compared to a few days or hours for laboratory testing. The OCP data therefore may be more useful in determining lifetime corrosion behavior of the samples in actual use.

The OCP of a FS weld, an autogenous weld, and a dissimilar weld on AL-6XN was determined. In addition, the OCP of as-received plates of AL-6XN, 304 SS, and IN625 were determined for comparison, Table 3.3. Results from approximately 3 months of testing are shown in Figure 4-41A. In general, all of the materials initially have a

negative potential which increases with time. For all materials, this trend is associated with the formation of a layer of corrosion product that may or may not be passive. If the equilibrium potential is positive, the layer is passive but if the equilibrium potential is negative, the layer is not protective and corrosion continues. As mentioned in the background, sharp fluctuations in the potential indicate localized corrosion and was the case for the a Cu-10%Ni alloy in brackish water, Figure 2-33. When the passive layer breaks down, the OCP drops but then will increase upon pit repassivation. It should be noted that there are three sites indicated on the graph where the potential of all samples drops. These anomalies resulted from a disruption in testing and should be disregarded. For example, the first interruption occurred at approximately 15 days and was caused by a failure in the pump system circulating fresh seawater into and out of the tank.

As expected, IN 625 exhibits the most positive or most noble potential and should experience the least attack. Compared to the other materials, however, IN 625 exhibits numerous fluctuations in the potential suggesting that the passive layer is continually breaking down but quickly repairing itself.

As expected, the potential of as-received AL-6XN base metal is noble to all welds as well as the 304 SS plate, Figure 4-41A. Initially, the potential of the FS weld is active when compared to the AL-6XN autogenous and filler metal welds. With increasing time, the potential of the autogenous weld and the filler metal weld steadily decreases (becoming more active) and the potential of the FS weld steadily increases (becoming more noble). At about 35 days, the potentials of the three welds are essentially the same. After this time, the potential of the FS weld continues to increase and approaches a

neutral potential suggesting that the corrosion rate is minimal. The corrosion of the filler metal weld and the autogenous weld, however, continues to decrease suggesting that the passive layer is breaking down and the samples are corroding. The fusion welds appear to have acceptable corrosion resistance initially but, with time, these metals experience attack. As discussed, the microsegregation in the welds is responsible for the poor corrosion resistance. On the contrary, the potential of the FS weld is initially low but increases with time and eventually becomes noble. Although the FS weld may take a longer time to equilibrate, its steady state behavior suggests a lower corrosion rate and therefore superior corrosion behavior compared to fusion welds.

It should be noted that a difference of more than 25 mV suggests different corrosion behavior. Although the equilibrium current of the FS weld is essentially zero mV, it is approximately 50 mV active with respect to the equilibrium potential of the as-received AL-6XN plate. Therefore the corrosion resistance of AL-6XN is degraded by FSW but the performance of this joining technique is better than fusion welding. It is interesting to note that the potential of the AL-6XN plate and all of the welds does not change erratically suggesting general corrosion as opposed to localized attack.

The oxygen content, conductivity, the salinity, temperature, pH, and dissolved oxygen were monitored during the OCP testing, Figure 4-41B. Each of these parameters can affect the potential of a sample. As seen in the figure with the exception of saturated oxygen, all parameters remain relatively constant over time. None of the all samples show a correlation between potential and the saturated oxygen. Therefore, the changing

saturated oxygen concentration does not significantly affect the long-term corrosion behavior of the samples.

Table 4. 1 *Composition analysis of a doubled-sided friction stir weld on AL-6XN obtained using EPMA.*

Element	Cr wt %	Mo wt %	Fe wt %	Ni wt %
UNS N08367 Tolerances	20.00-22.00	6.00-7.00	Balance	23.50-25.50
Base Metal	20.47	5.97	Balance	23.40
Nugget	20.53	5.95	Balance	23.41

Table 4. 2 *The CPTs of the various samples tested.*

Material	CPT (°C)
AL-6XN plate	70
RET side, plate 1	65
ADV side, plate 1	55
RET side, plate 2	55
ADV side, plate 2	55

Table 4. 3 *The ten deepest pits measured on as-received AL-6XN plate tested at 95°C.*

Pit #	2 min pit depth (μm)	5 min pit depth (μm)	10 min pit depth (μm)	20 min pit depth (μm)	30 min pit depth (μm)	60 min pit depth (μm)
1	80	123	176	246	287	395
2	80	122	153	240	239	328
3	79	122	140	235	232	319
4	74	120	134	220	230	284
5	72	119	133	212	227	277
6	72	112	132	204	214	273
7	71	111	124	197	213	255
8	70	101	122	193	201	232
9	69	101	119	190	198	220
10	65	99	115	186	197	174

Table 4. 4 *The ten deepest pits present on a AL-6XN FS weld tested at 95°C.*

Pit #	2 min pit depth (μm)	5 min pit depth (μm)	10 min pit depth (μm)	20 min pit depth (μm)	30 min pit depth (μm)	60 min pit depth (μm)
1	93	114	167	171	309	333
2	78	111	155	216	279	316
3	67	109	154	172	267	306
4	66	108	147	262	262	285
5	65	104	144	190	258	273
6	63	101	137	234	244	271
7	60	96	127	212	239	253
8	60	93	122	175	237	252
9	59	91	122	227	221	242
10	56	89	121	234	211	240

Table 4. 5 *The absolute maximum pit depth recorded for all exposure times in the AL-6XN as-received plate and FS weld.*

Time (min)	FS weld 95°C pit depth (μm)	As-received plate 95°C pit depth (μm)	FS weld 70°C pit depth (μm)	As-received plate 70°C pit depth (μm)
2	93	80	49	31
5	114	123	87	72
10	167	176	122	36
20	262	246	185	41
30	309	287	263	56
60	333	345	351	267

Table 4. 6 *The average maximum pit depth recorded for all exposure times in the AL-6XN as-received plate and FS weld.*

Time (min)	FS weld 95°C pit depth (μm)	As-received plate 95°C pit depth (μm)	FS weld 70°C pit depth (μm)	As-received plate 70°C pit depth (μm)
2	66.7	73.2	36.4	22.8
5	101.6	113	57.9	43.8
10	139.6	134.8	93.5	28.5
20	209.3	212.3	131.1	35.1
30	252.7	223.8	179.2	30.6
60	277.1	270.7	209.6	83.2

Table 4. 7 *The ten deepest pits present on as-received AL-6XN plate tested at 70°C.*

Pit #	2 min pit depth (μm)	5 min pit depth (μm)	10 min pit depth (μm)	20 min pit depth (μm)	30 min pit depth (μm)	60 min pit depth (μm)
1	31	72	36	41	56	49
2	28	54	28	39	39	58
3	26	45	26	39	32	160
4	24	45	24	39	29	28
5	23	41	23	35	28	127
6	23	38	20	33	27	36
7	21	37	30	32	26	267
8	21	36	29	31	25	31
9	16	35	33	31	22	34
10	15	35	36	31	22	42

Table 4. 8 *The ten deepest pits present on a AL-6XN friction stir weld tested at 70°C.*

Pit #	2 min pit depth (μm)	5 min pit depth (μm)	10 min pit depth (μm)	20 min pit depth (μm)	30 min pit depth (μm)	60 min pit depth (μm)
1	49	87	122	185	263	351
2	45	68	114	179	262	271
3	38	61	107	168	238	170
4	38	59	104	150	218	249
5	36	57	101	143	181	209
6	34	56	88	122	152	142
7	33	54	78	110	151	246
8	32	48	77	110	116	232
9	30	45	73	78	106	115
10	29	44	71	66	105	111

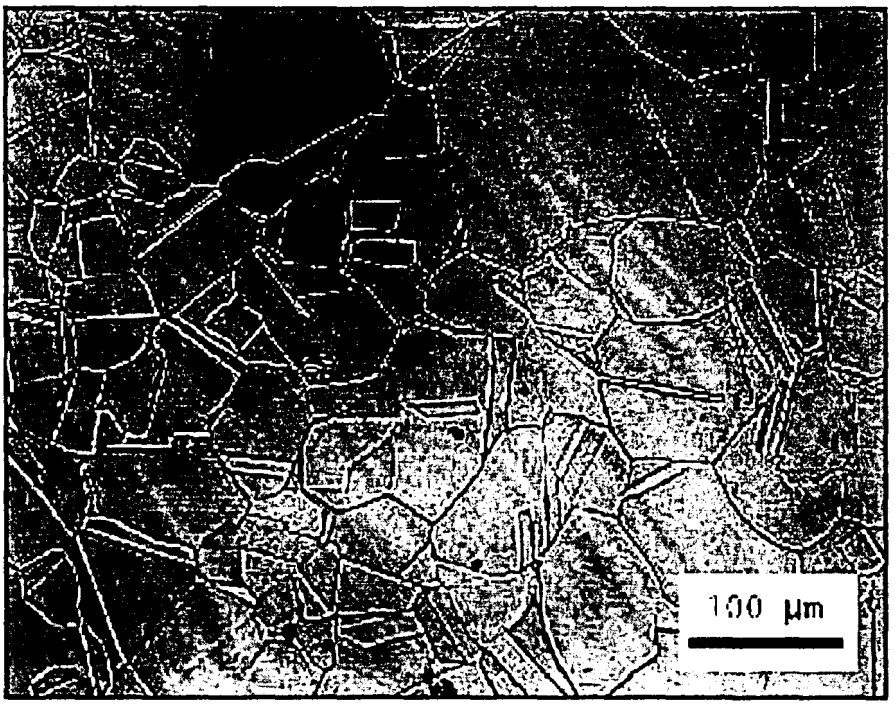

Fig. 4-1 Base metal microstructure, consisting of large equiaxed austenite grains with annealing twins.

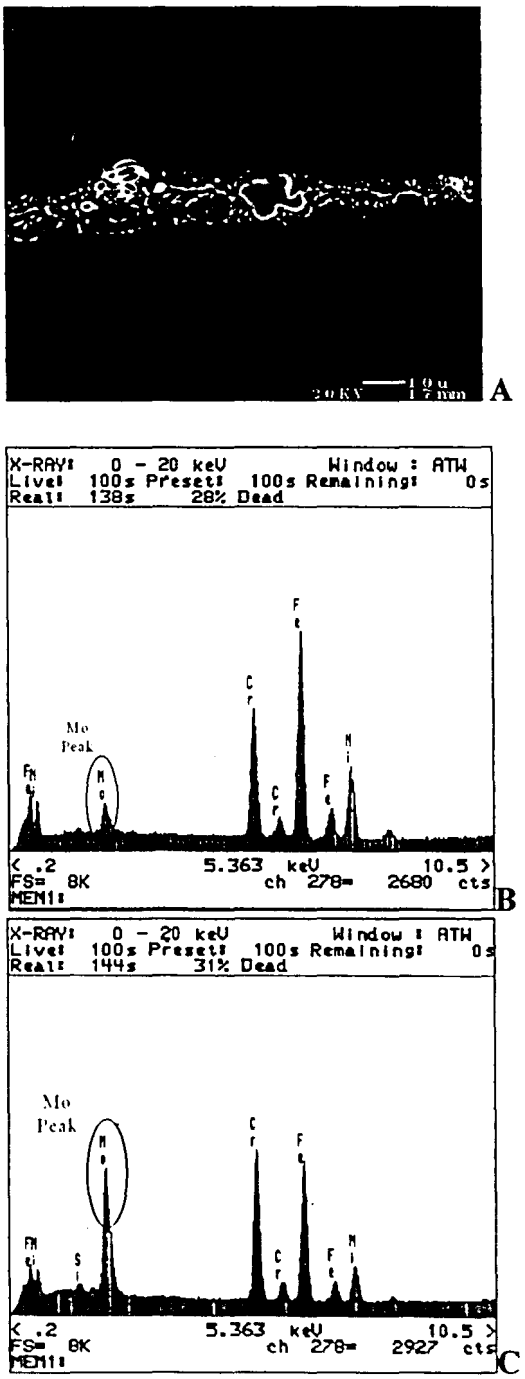

Fig. 4-2 A) SEM image of the secondary phase located at mid-plate thickness in the base metal and the EDS spectra of the B) base metal and C) second phase.

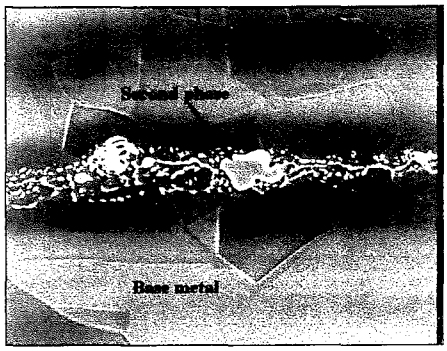

A

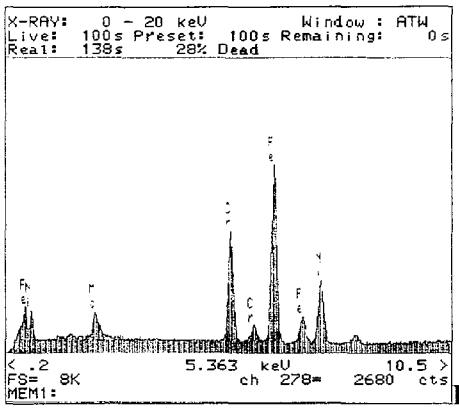

B

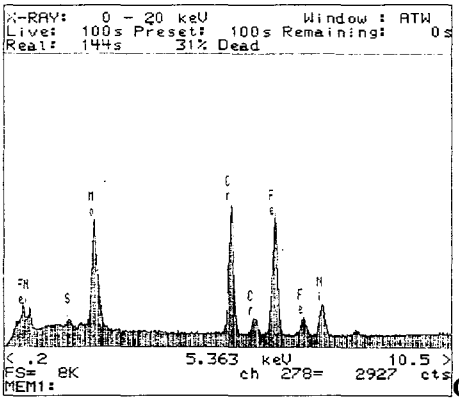

C

Fig. 4-2 A) SEM image of the secondary phase located at mid-plate thickness in the base metal and the EDS spectra of the B) base metal and C) second phase.

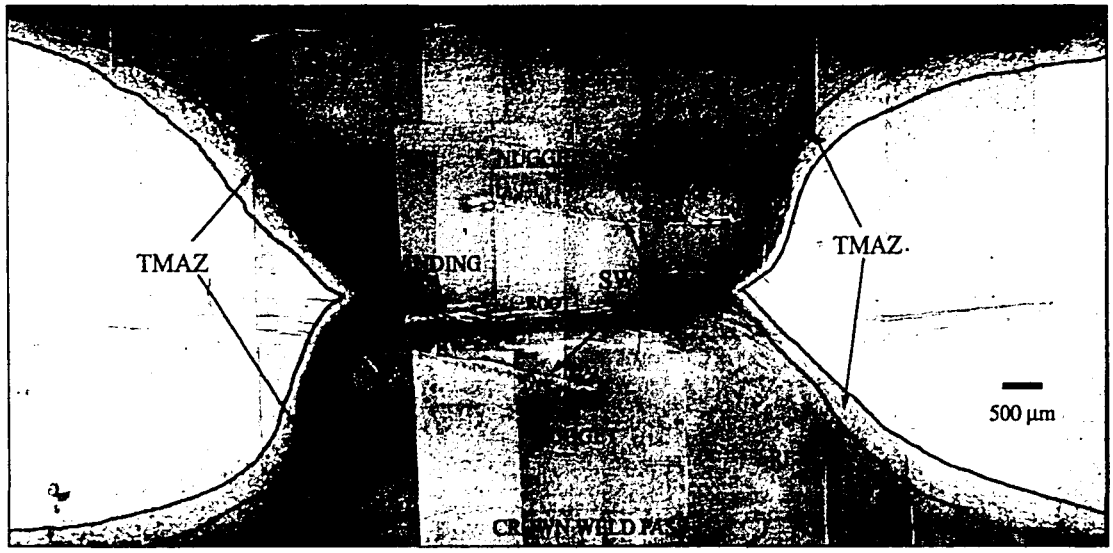

A

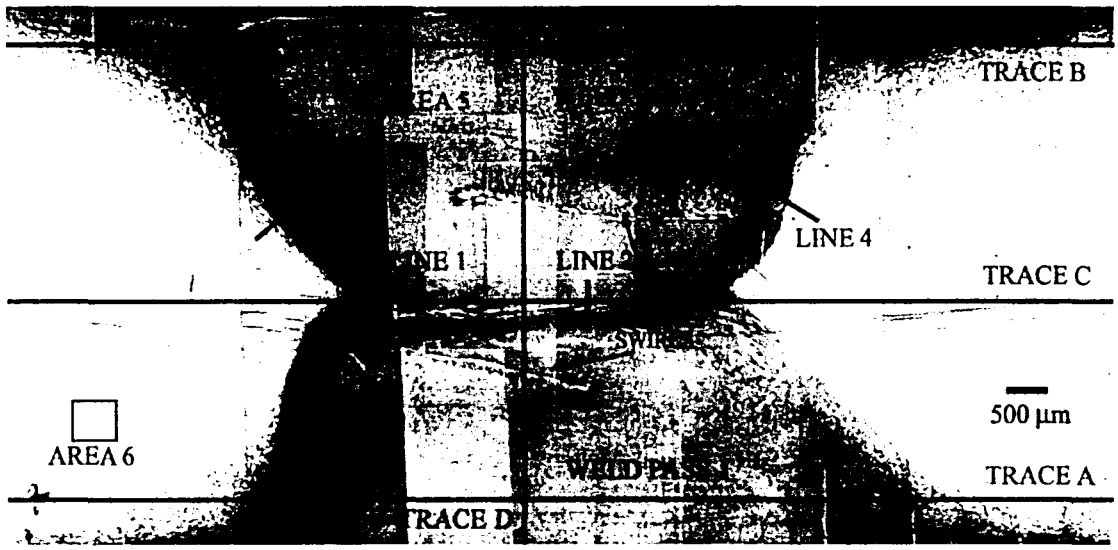

B

Fig. 4-3 Light optical micrograph of a cross-section of the FSW: A) defining microstructural regions in the weld and B) showing location of microhardness and EPMA traces and several microstructural features.

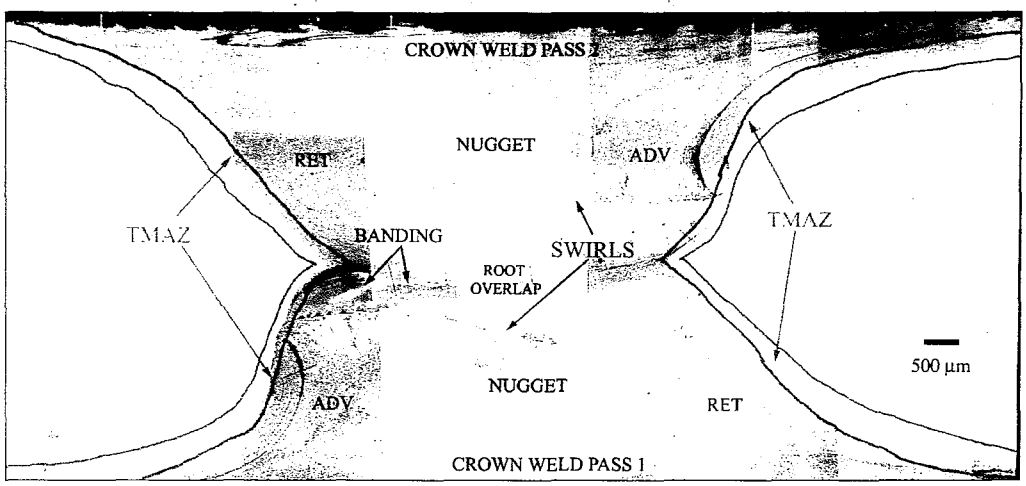

A

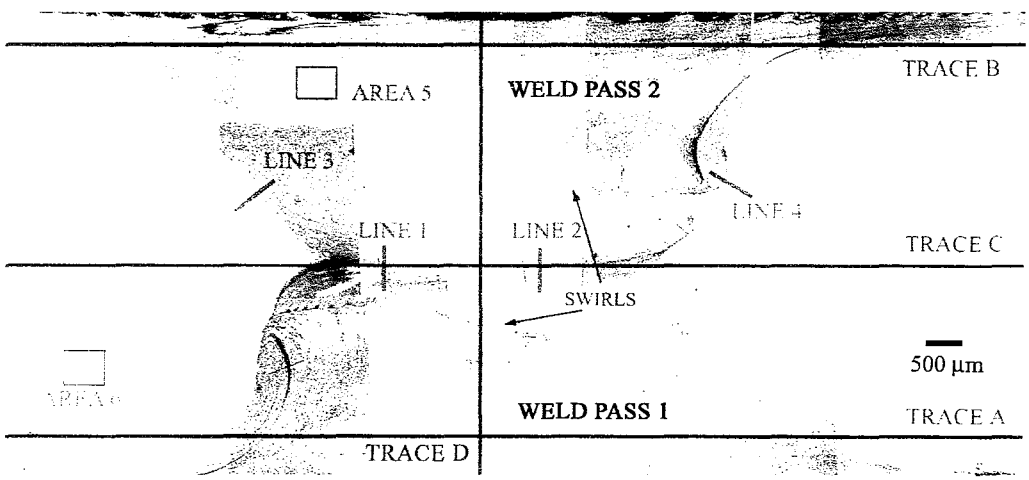

B

Fig. 4-3 Light optical micrograph of a cross-section of the FSW: A) defining microstructural regions in the weld and B) showing location of microhardness and EPMA traces and several microstructural features.

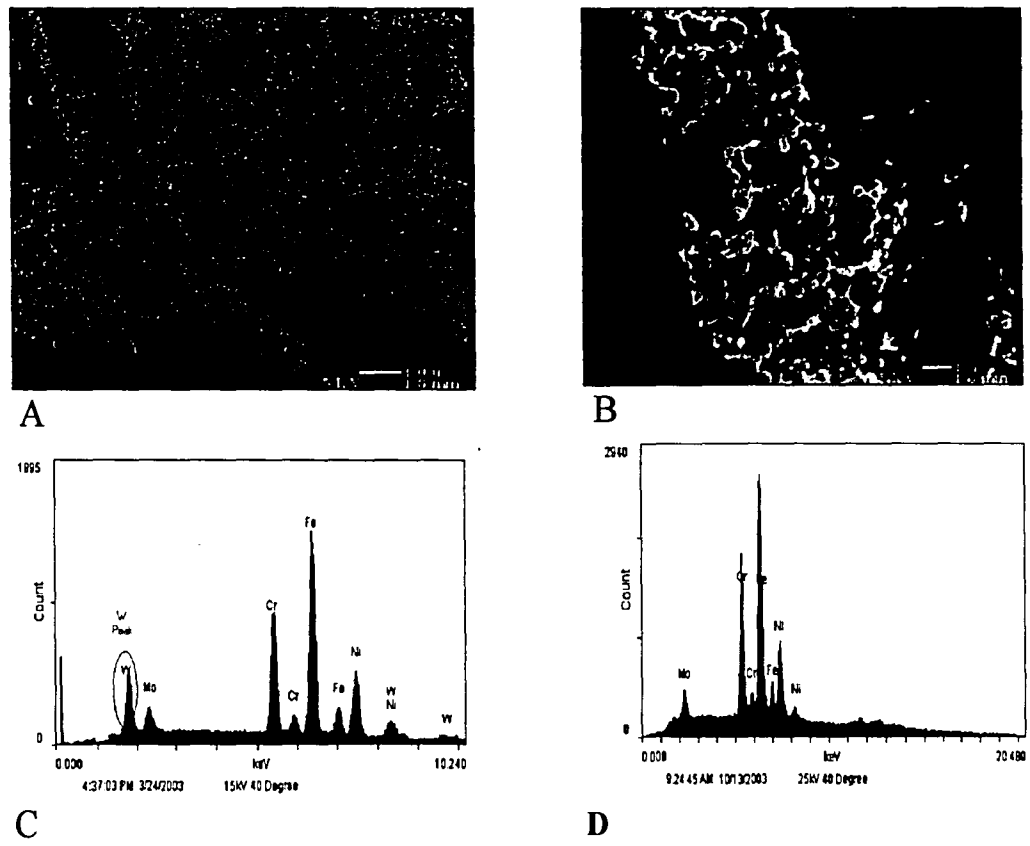

Fig. 4-4 A) and B) SEM images of the swirl found in the nugget and the EDS spectra obtained from C) the swirl and D) the nugget matrix

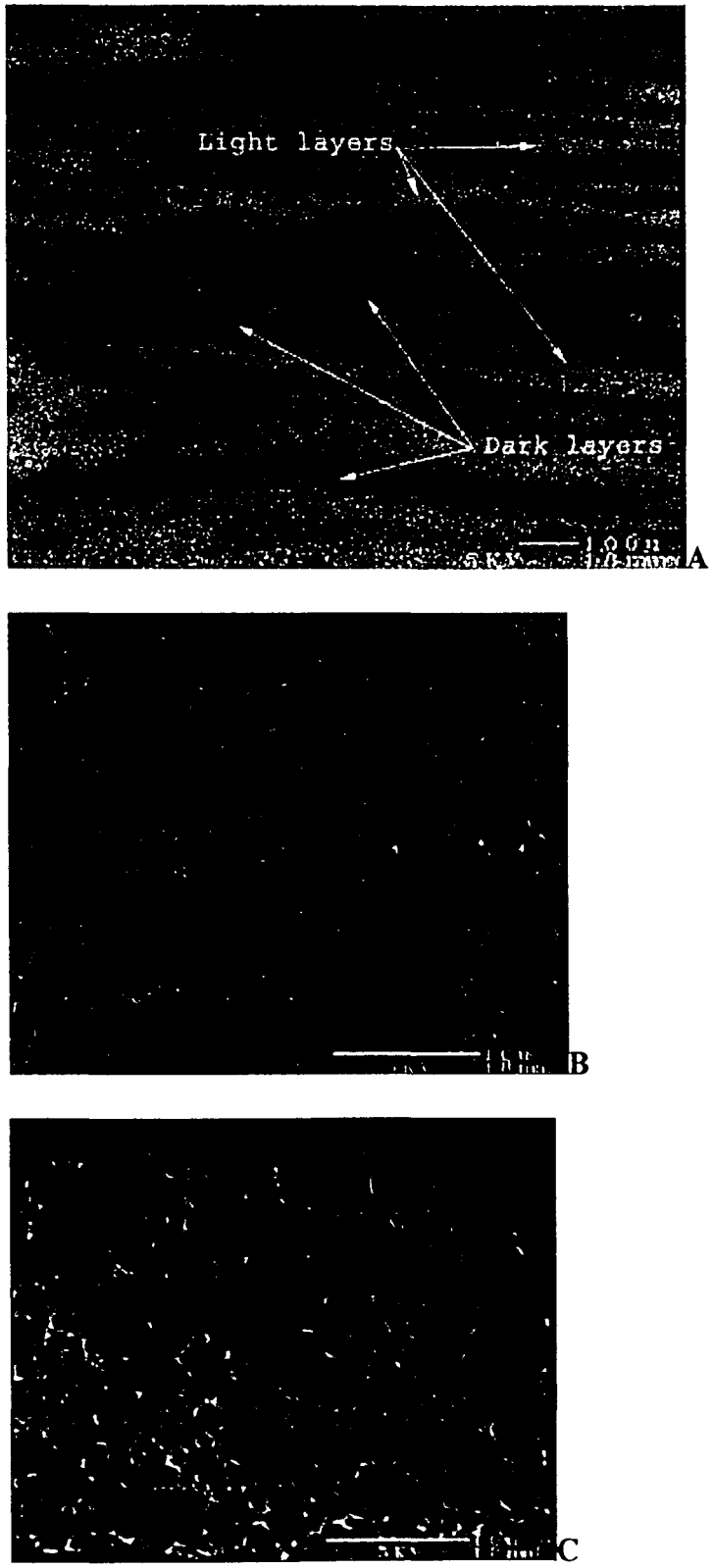

Fig. 4-5 A) SEM image of the banding seen at the boundary of weld pass 1 and 2 and high magnification SEM images of the B) dark and C) light bands seen in A).

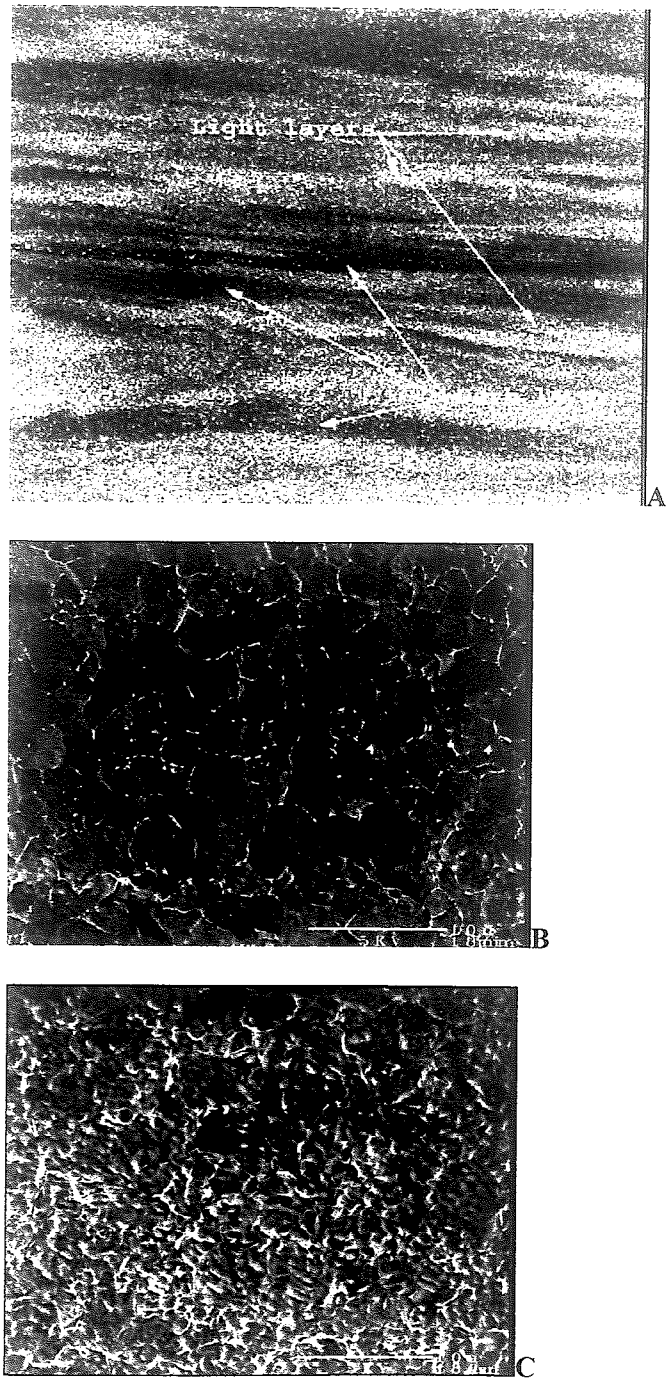

Fig. 4-5 A) SEM image of the banding seen at the boundary of weld pass 1 and 2 and high magnification SEM images of the B) dark and C) light bands seen in A).

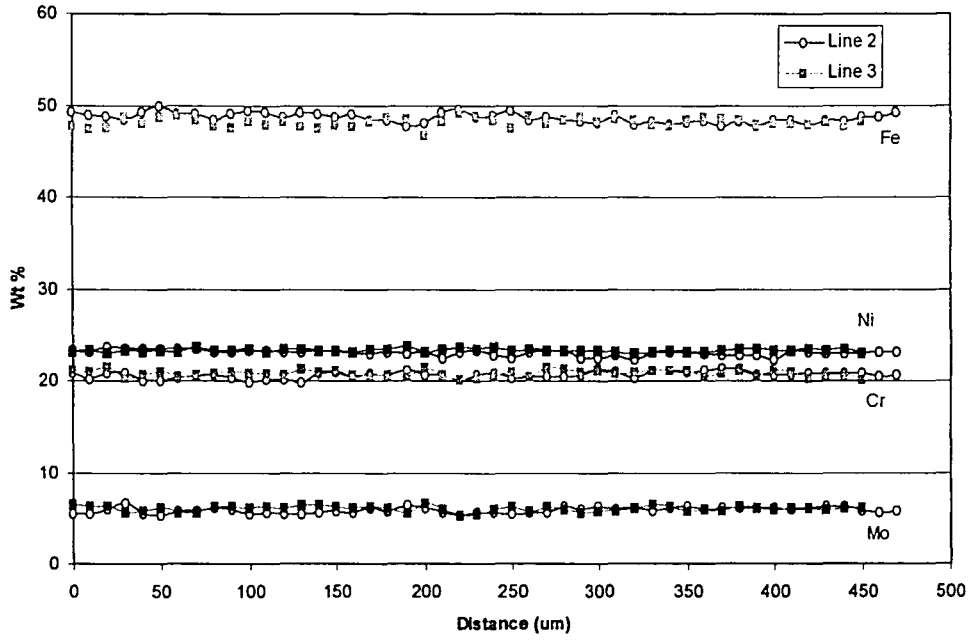

Fig. 4-6 EPMA data of lines 1 and 2, both of which extend across the boundary of weld pass 1 and 2.

A

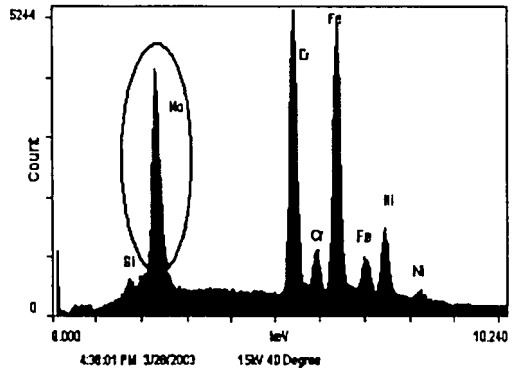

B

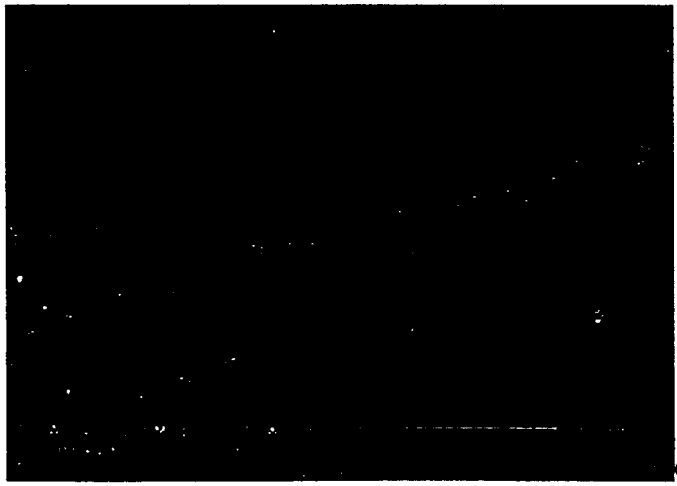

C

Fig. 4-7 A) SEM image of the secondary phase in the nugget similar to the sigma phase in the base metal, B) the EDS spectrum of that phase and C) additional sigma located throughout the nugget.

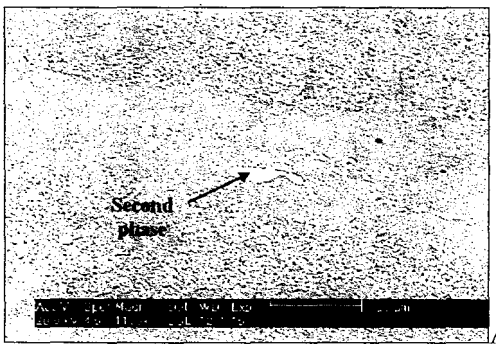

A

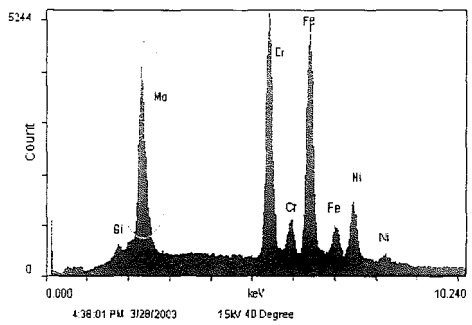

B

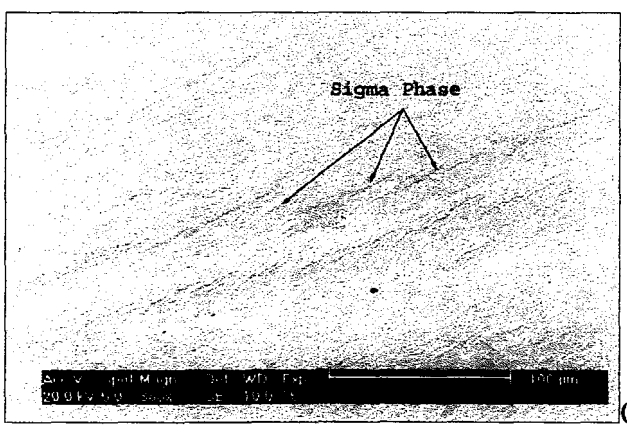

C

Fig. 4-7 A) SEM image of the secondary phase in the nugget similar to the sigma phase in the base metal, B) the EDS spectrum of that phase and C) additional sigma located throughout the nugget.

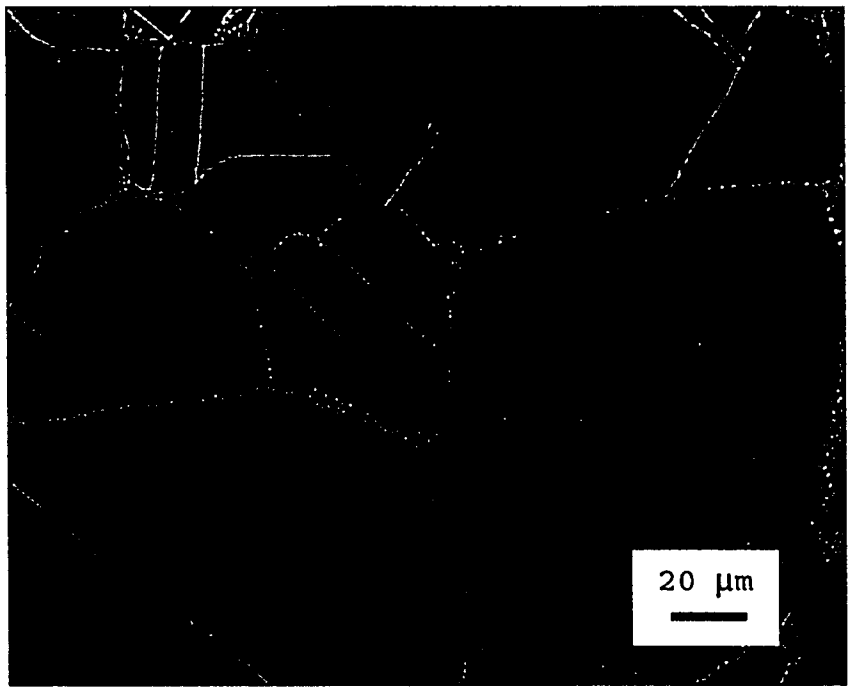

Fig. 4-8 Light optical micrograph of nucleation phenomena see in the grain boundaries of the HAZ.

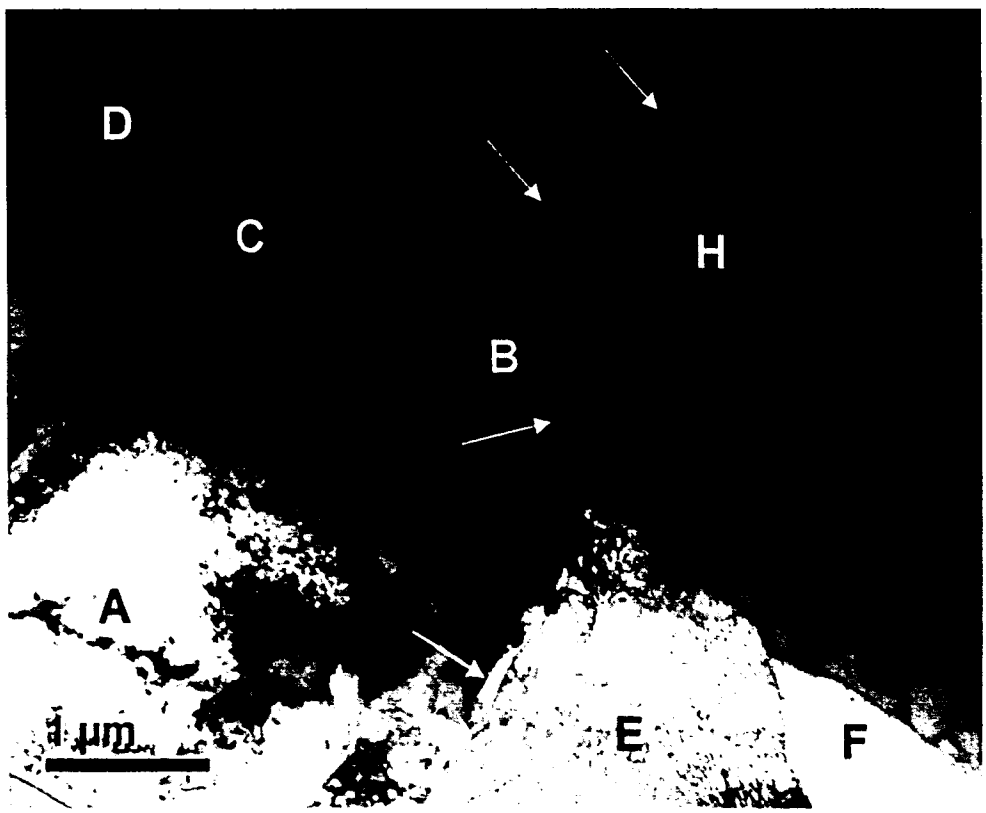

Fig. 4-9 Microstructure at the original austenite grain boundaries of the HAZ.

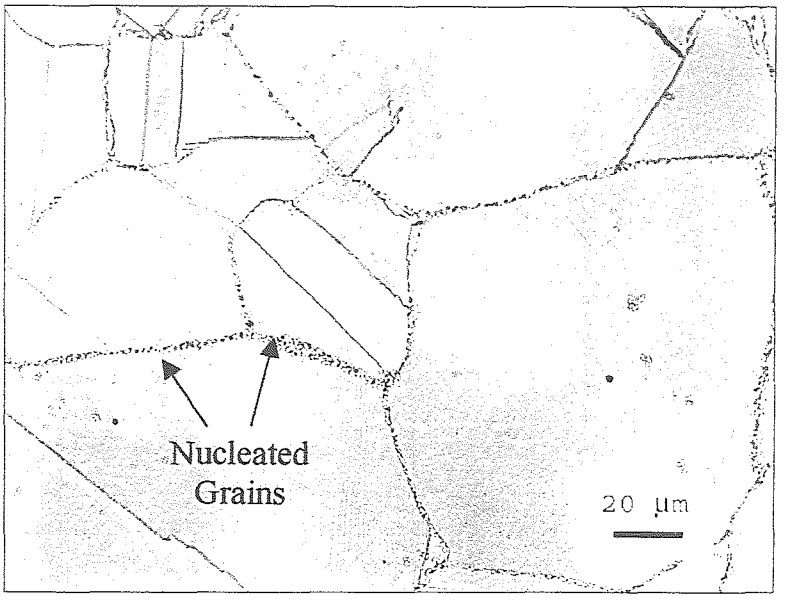

Fig. 4-8 Light optical micrograph of nucleation phenomena see in the grain boundaries of the HAZ.

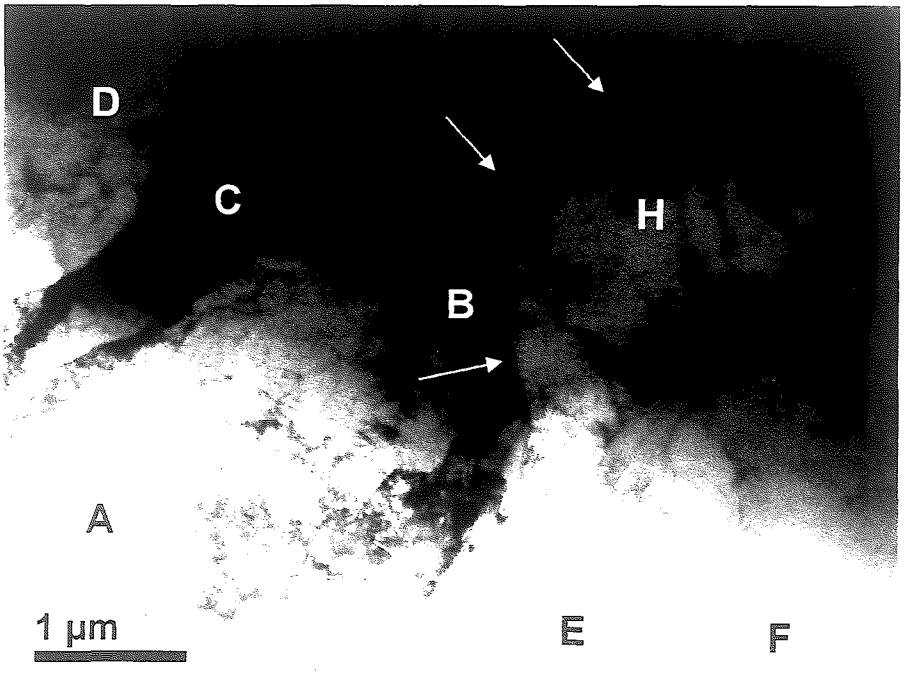

Fig. 4-9 Microstructure at the original austenite grain boundaries of the HAZ.

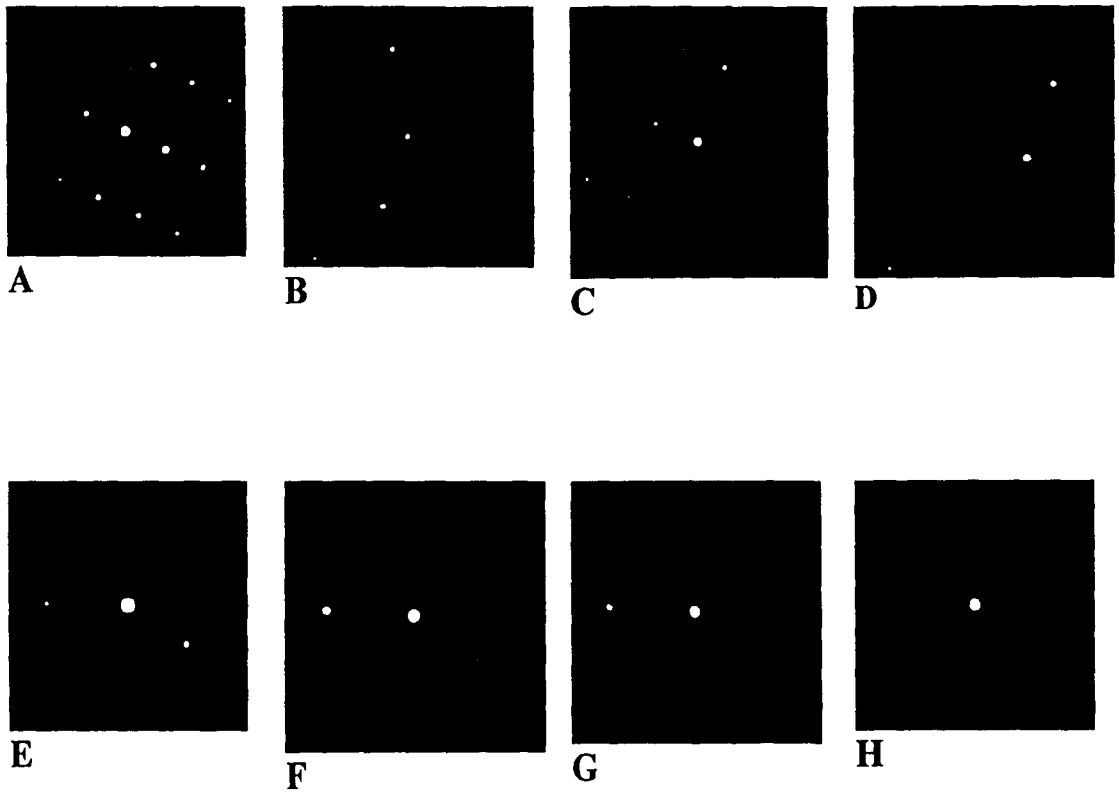

Fig. 4-10 A-F) SAD patterns obtained from regions A-H, respectively, as labeled in Figure 4-9.

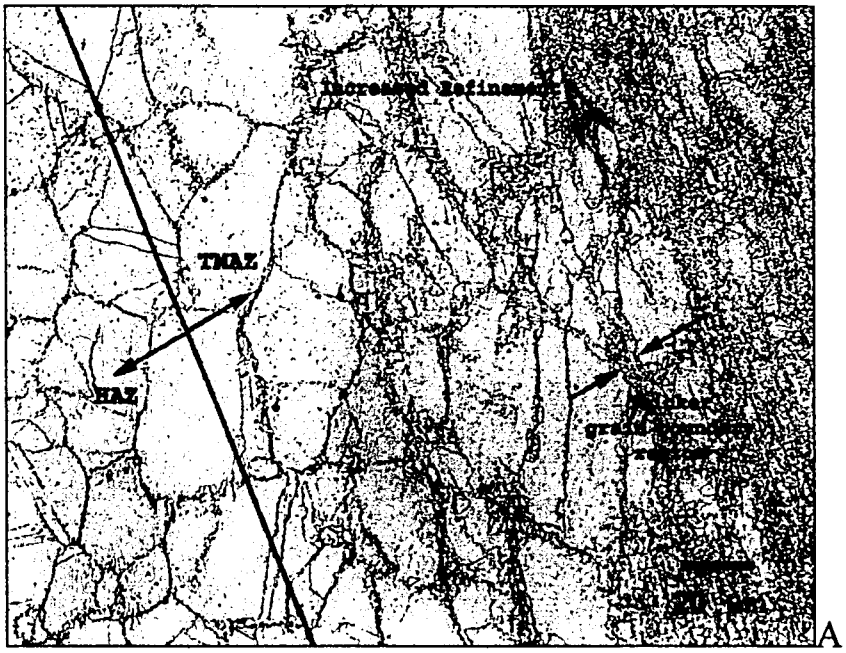

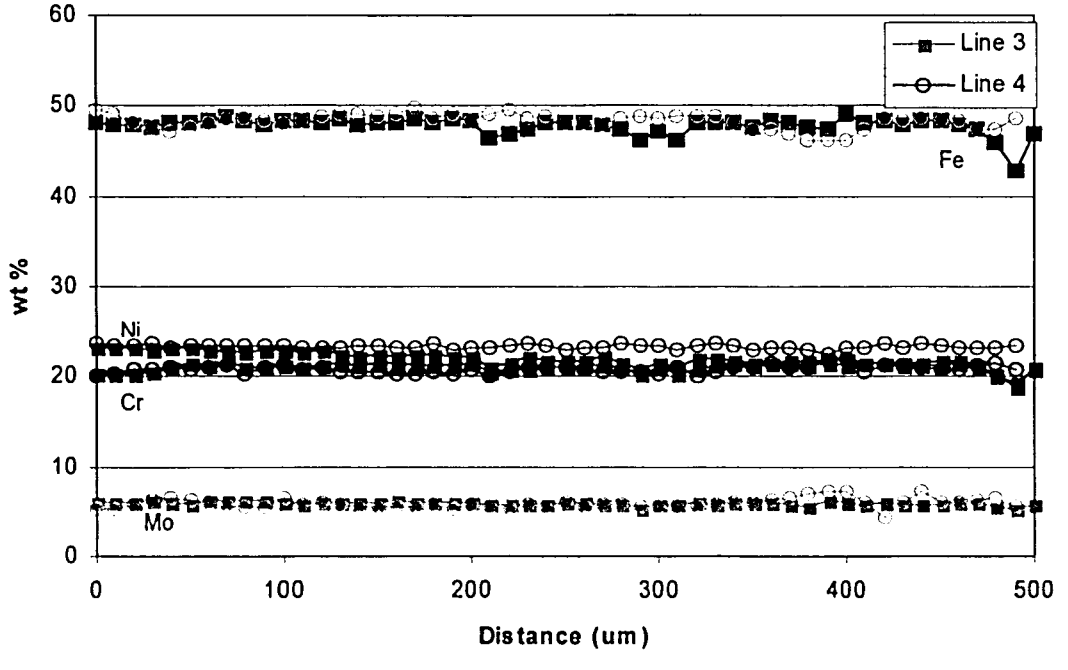

Fig. 4-11 A) Light optical image of the TMAZ where a transition from a pure HAZ microstructure to a nugget-type of microstructure is seen and B) the EPMA data of lines 3 and 4, both of which extend through the different microstructural regions of the FSW.

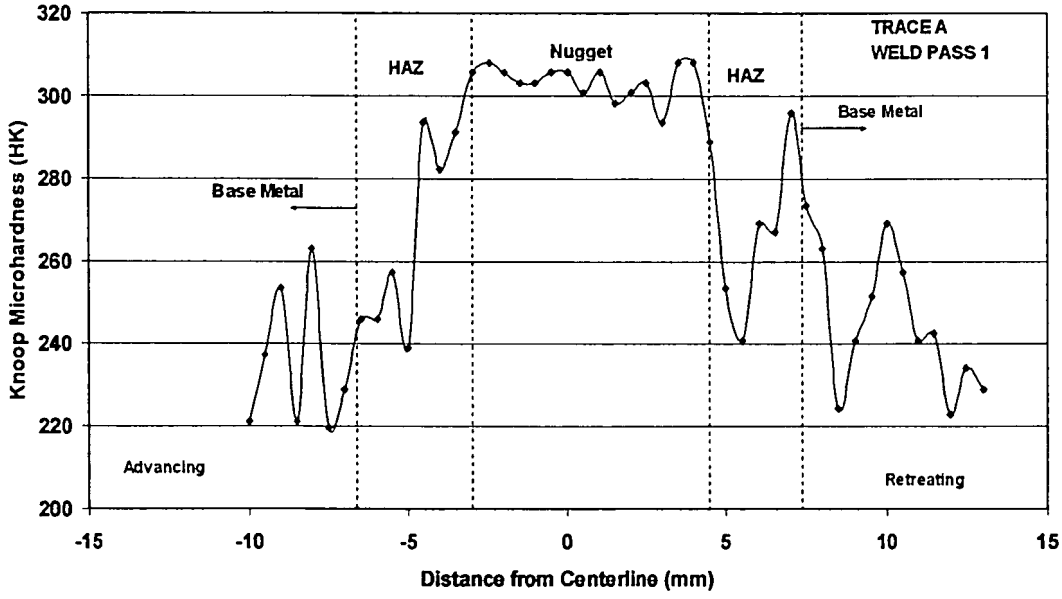

A

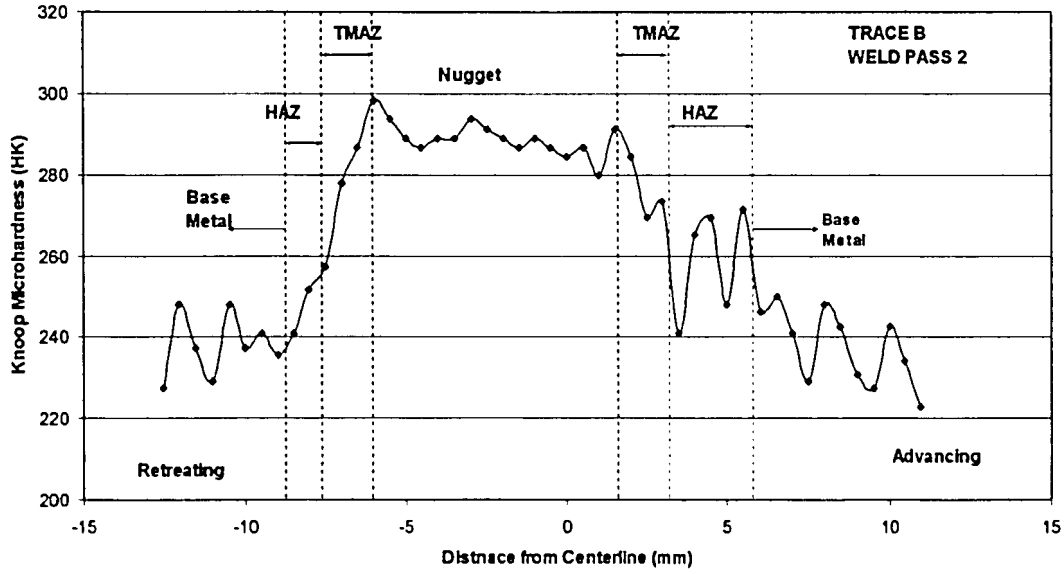

B

Fig. 4-12 Microhardness traces as a function of distance A) from the centerline across weld pass 1 B) from the centerline across weld pass 2.

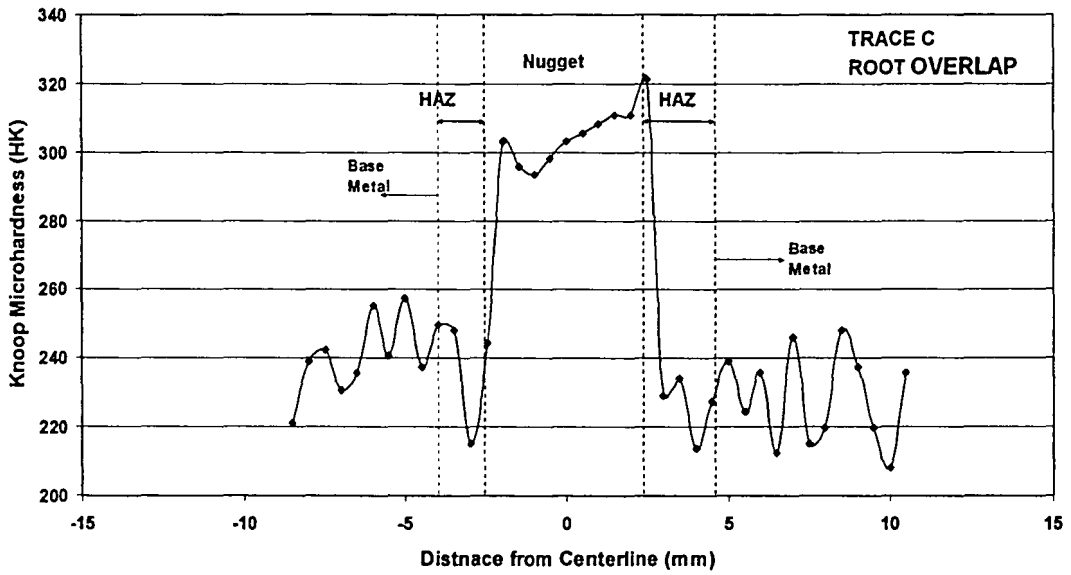

C

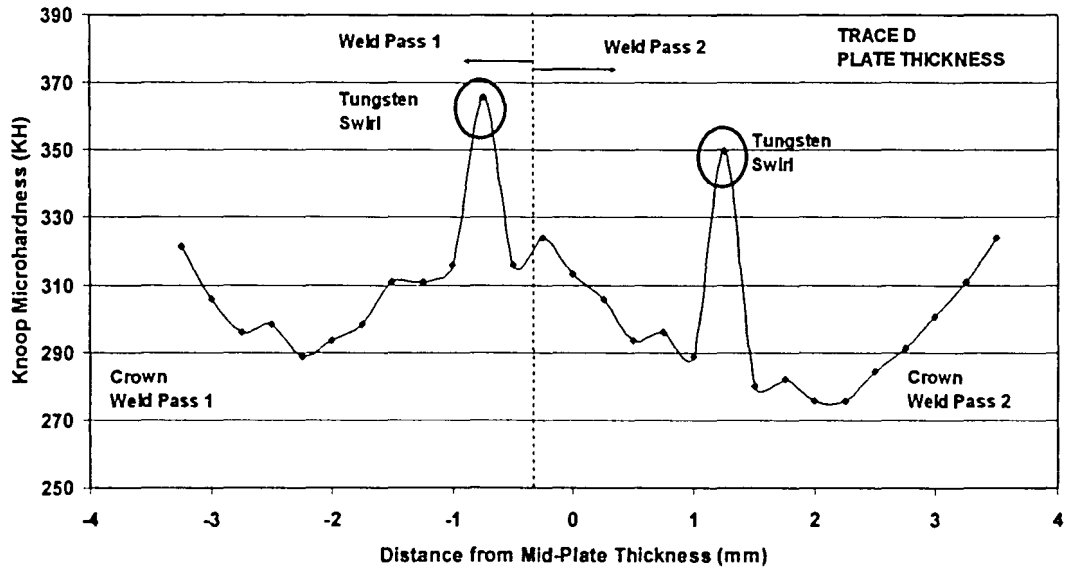

D

Fig. 4-12 Microhardness traces as a function of distance C) from the centerline across the weld pass overlap, and D) from the plate mid-plane along the weld centerline.

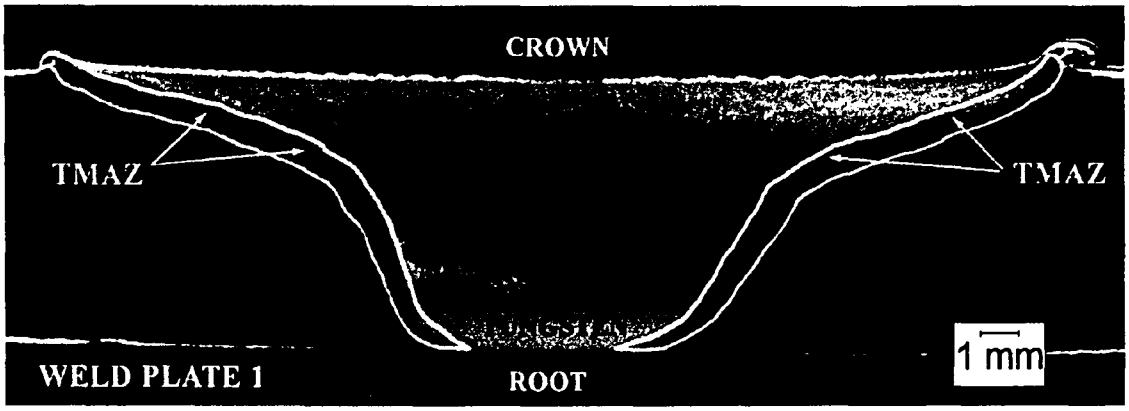

Fig. 4- 13 Representative image of a single-sided FS weld on AL-6XN plate.

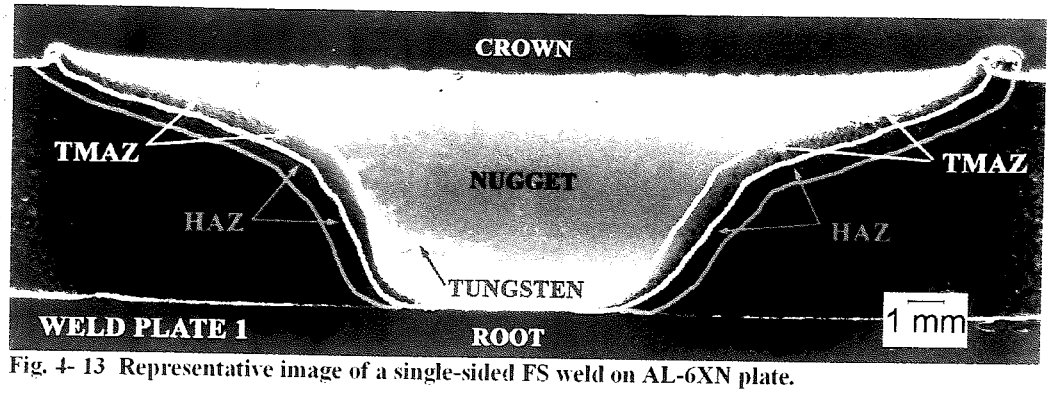

Fig. 4- 13 Representative image of a single-sided FS weld on AL-6XN plate.

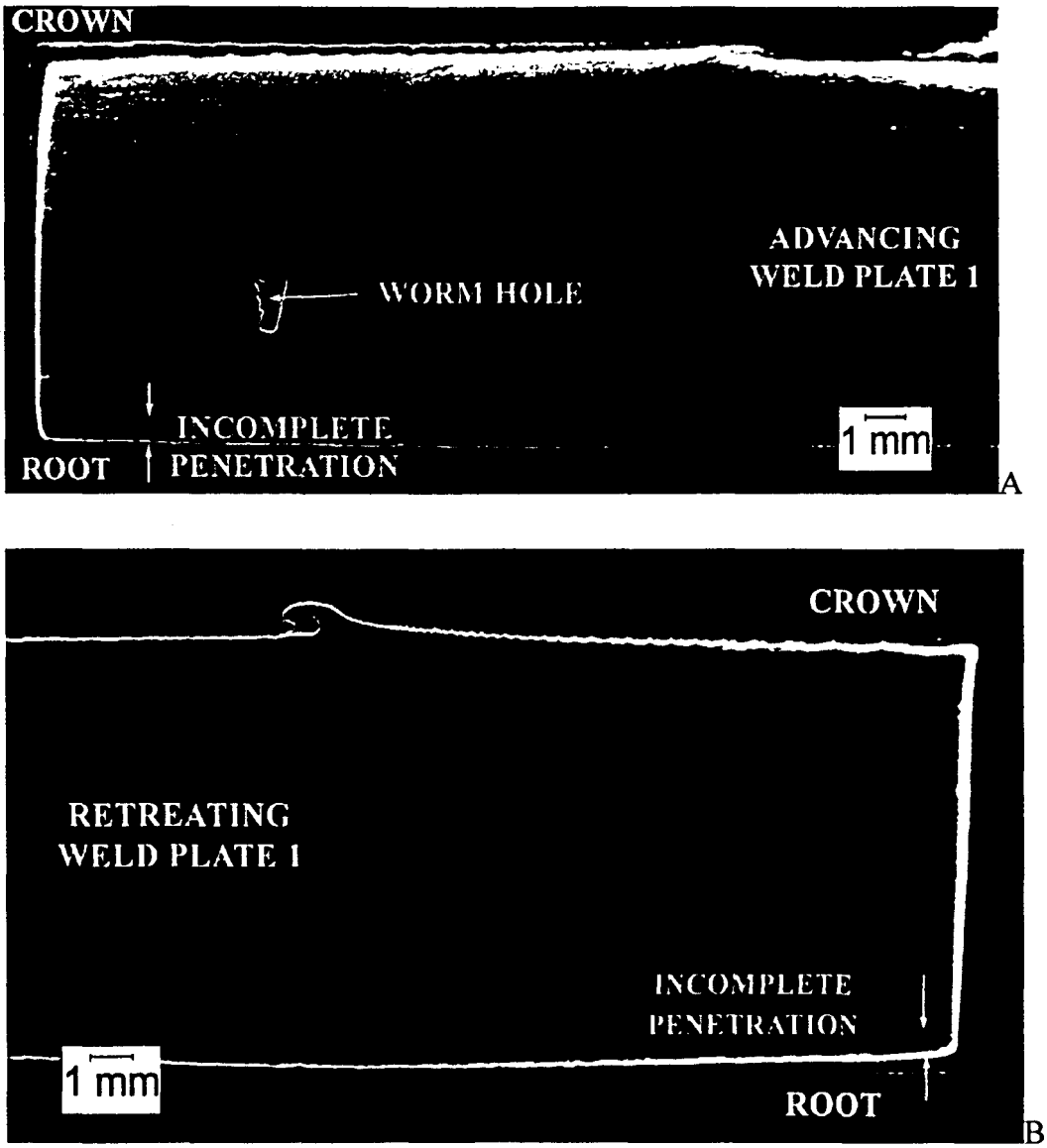

Fig. 4-14 Macrostructure of the half-welds on plate 1 of A) the advancing and B) the retreating sides.

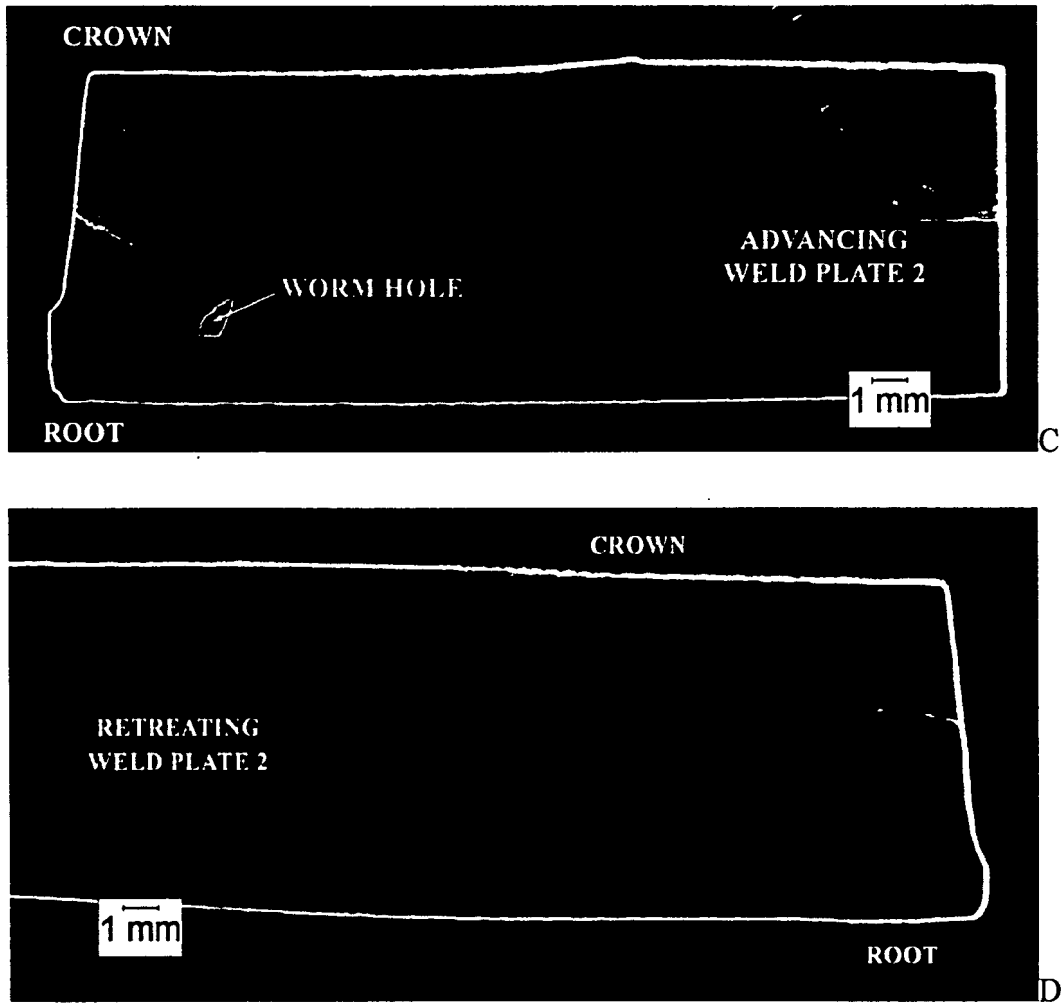

Fig. 4-14 Macrostructure of the half-welds on plate 2 of C) the advancing and D) the retreating sides.

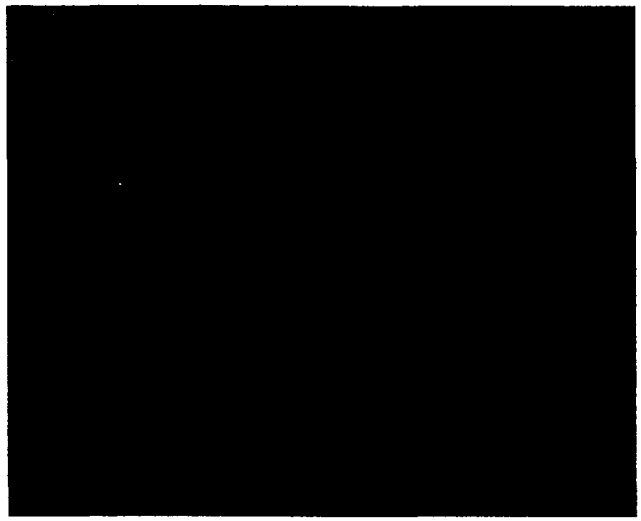

Fig. 4-15 Representative image of the AL-6XN base metal in both weld plate 1 and 2.

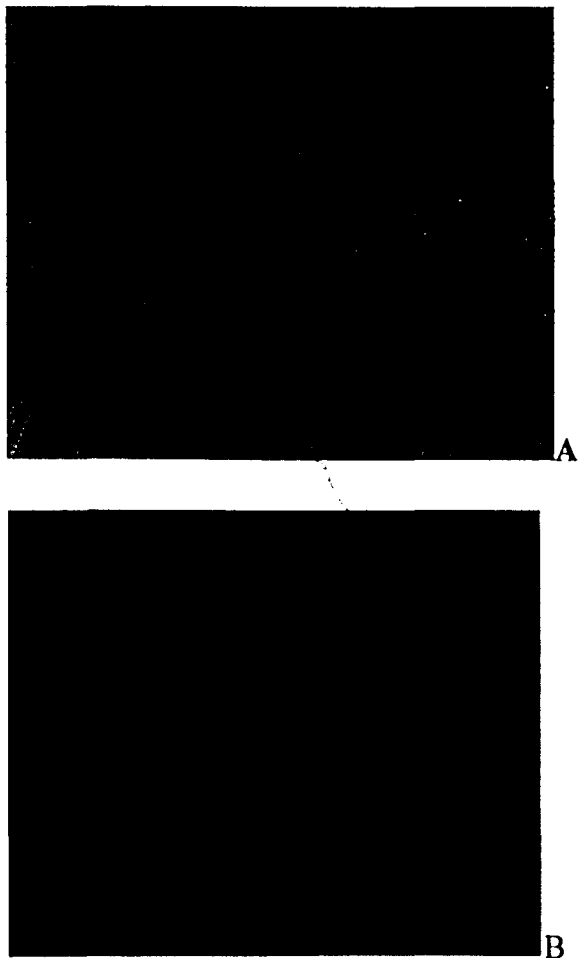

Fig. 4-16 Centerline sigma present in A) plate 2 in larger quantities compared to B) the amounts of sigma phase in plate 1.

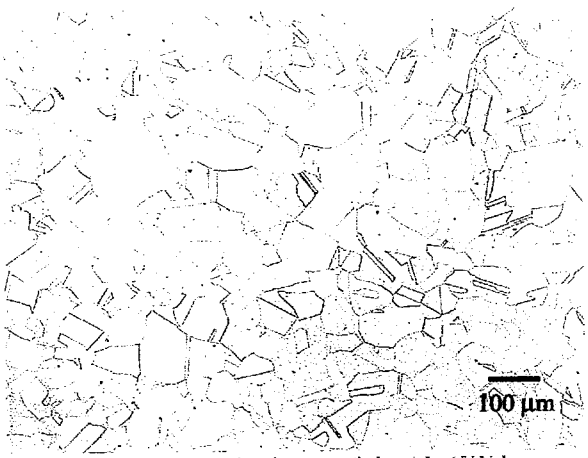

Fig. 4-15 Representative image of the AL-6XN base metal in both weld plate 1 and 2.

A

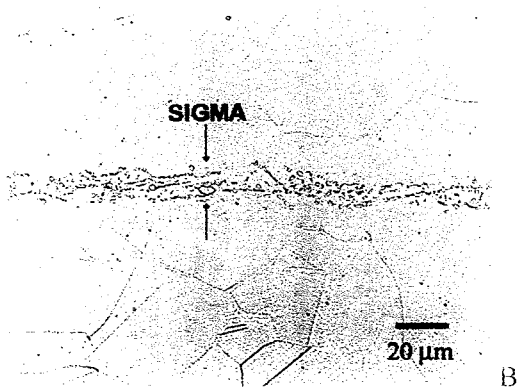

B

Fig. 4-16 Centerline sigma present in A) plate 2 in larger quantities compared to B) the amounts of sigma phase in plate 1.

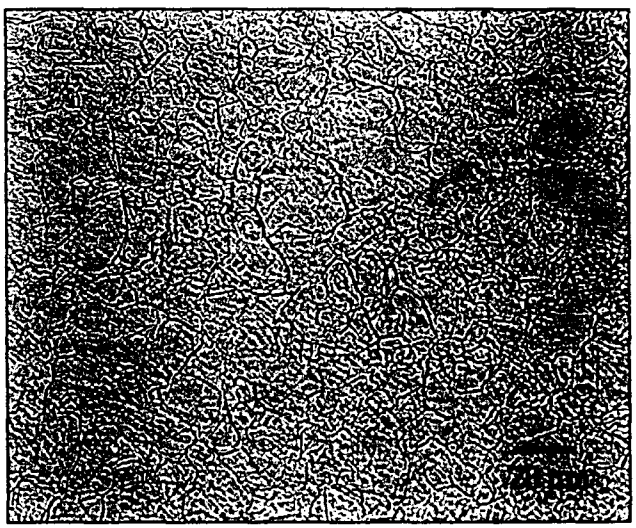

A

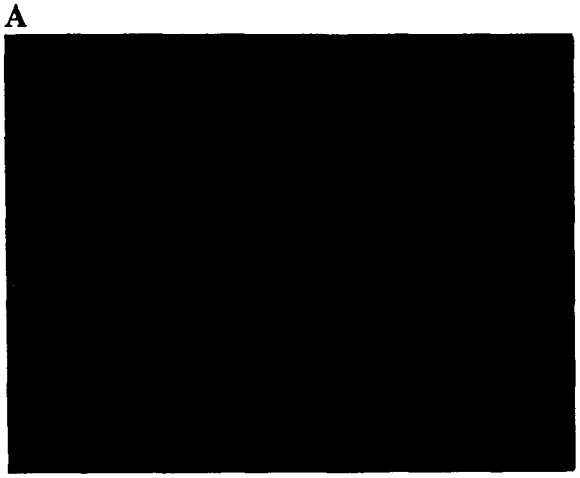

B

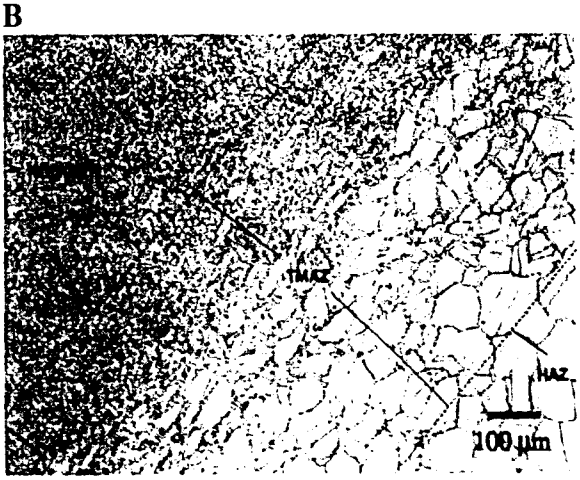

C

Fig. 4-17 Representative images of A) the nugget, B) the HAZ, and C) the TMAZ in a single-sided FS welds on plate 1 and 2.

A

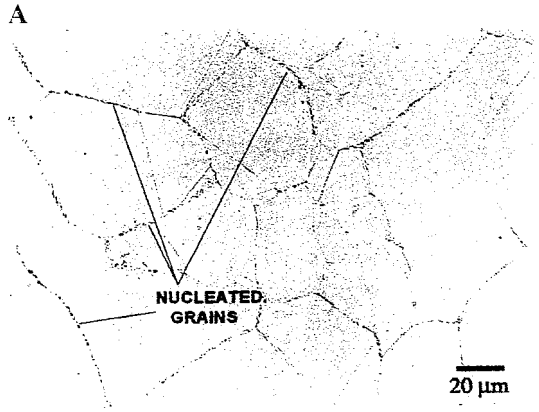

B

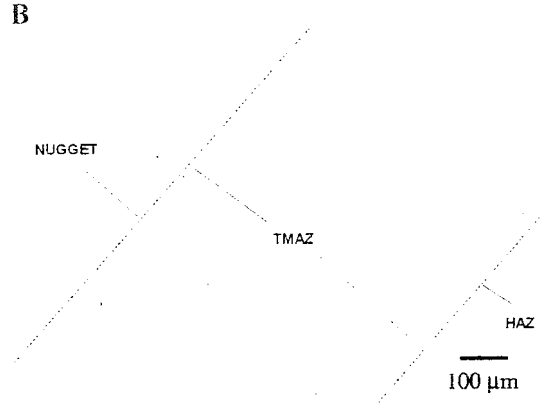

C

Fig. 4-17 Representative images of A) the nugget, B) the HAZ, and C) the TMAZ in a single-sided FS welds on plate 1 and 2.

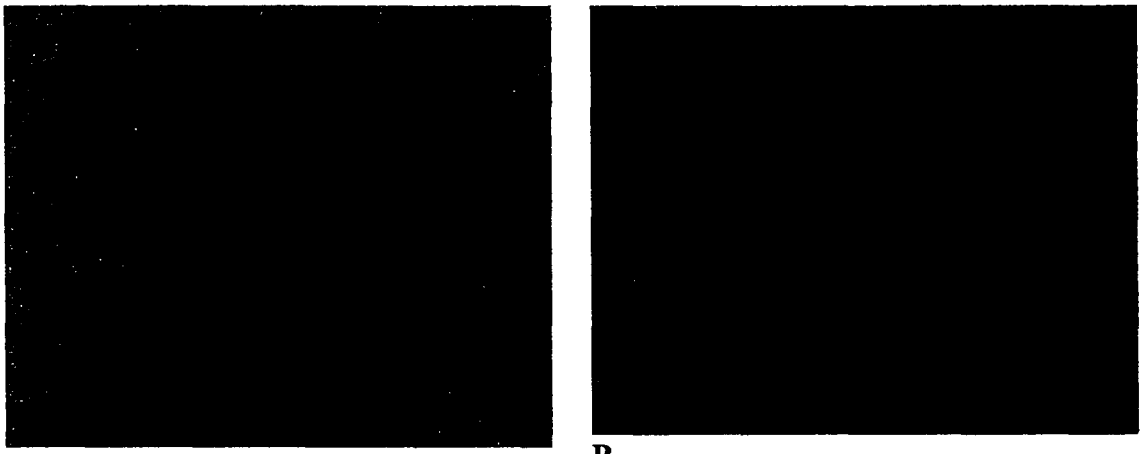

Fig. 4-18 The elaborate tungsten swirls present in the nugget of the single-sided FS welds of A) plate 1 and B) plate 2.

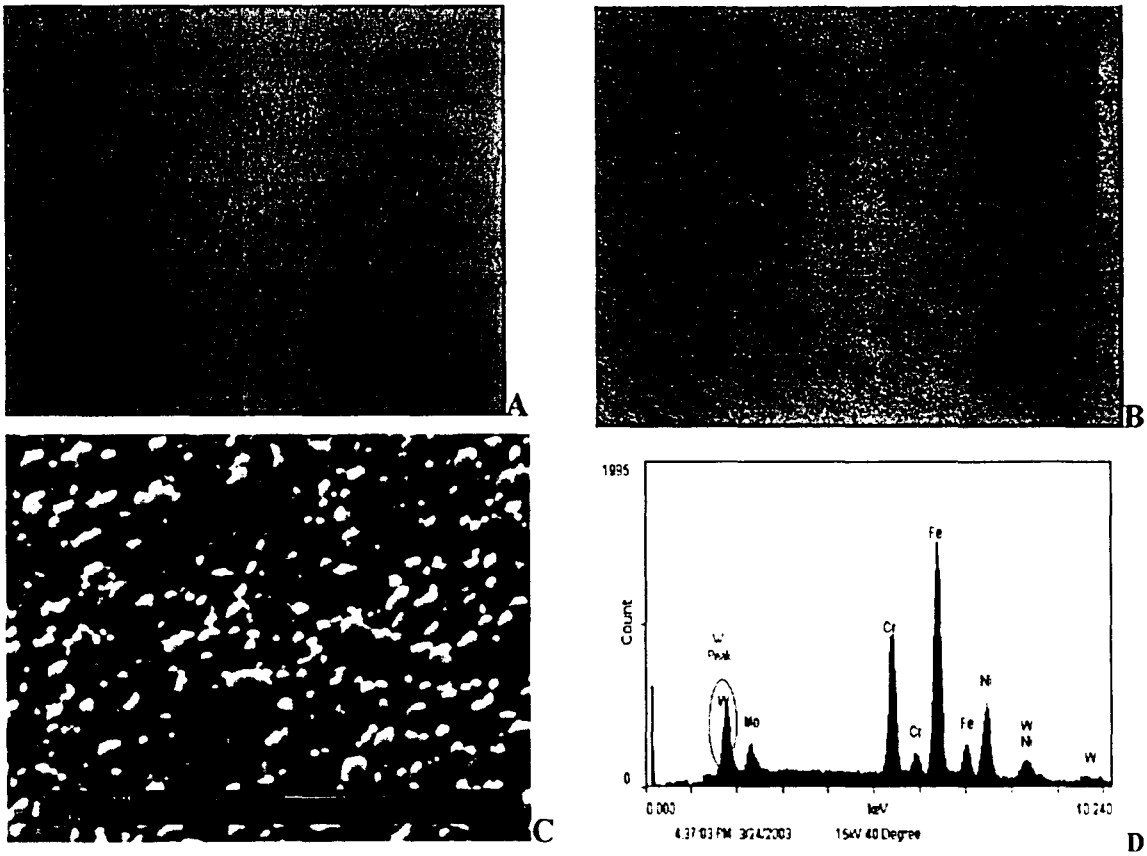

Fig. 4-19 The microstructure of the crown side of the FS weld showing A) the microstructural transition from the base metal to the nugget and also B) the tungsten banding using LOM. The tungsten is further seen in C) a high magnification SEM image of the tungsten and D) the EDS spectra from this region.

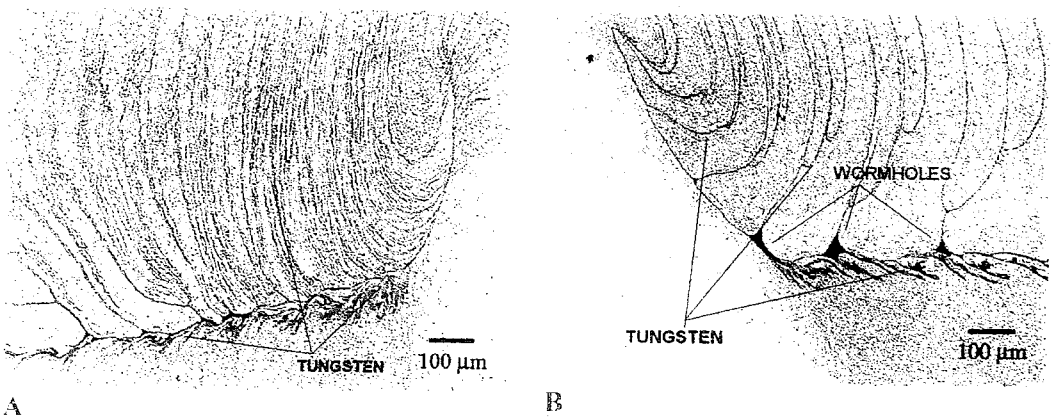

Fig. 4-18 The elaborate tungsten swirls present in the nugget of the single-sided FS welds of A) plate 1 and B) plate 2.

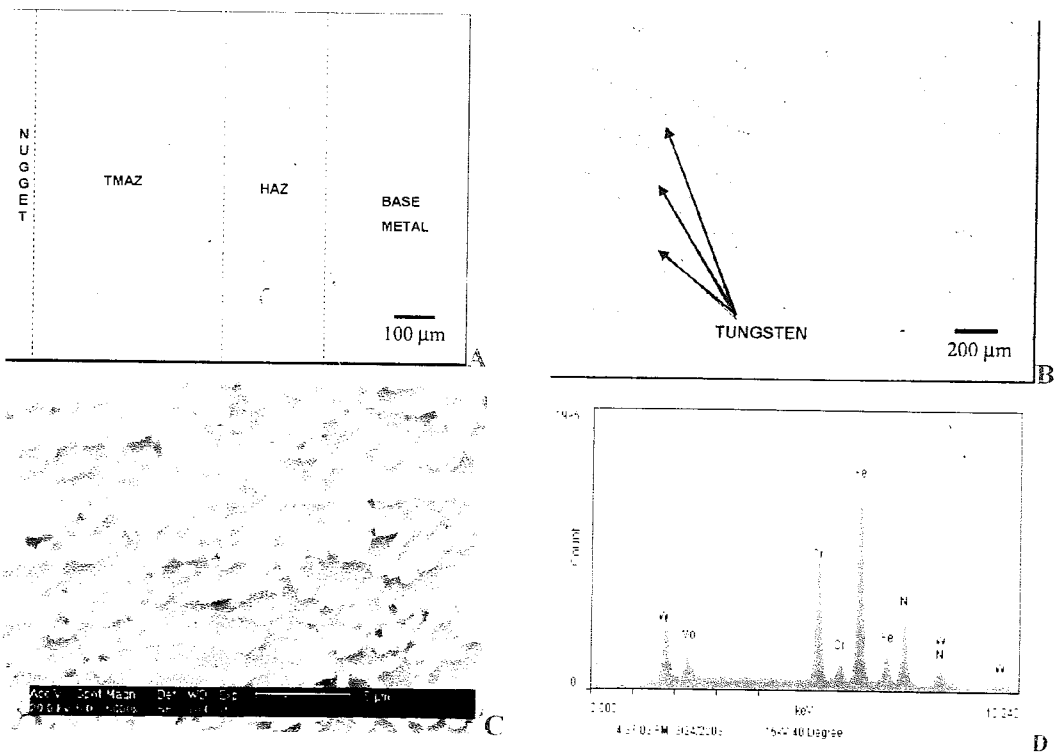

Fig. 4-19 The microstructure of the crown side of the FS weld showing A) the microstructural transition from the base metal to the nugget and also B) the tungsten banding using LOM. The tungsten is further seen in C) a high magnification SEM image of the tungsten and D) the EDS spectra from this region.

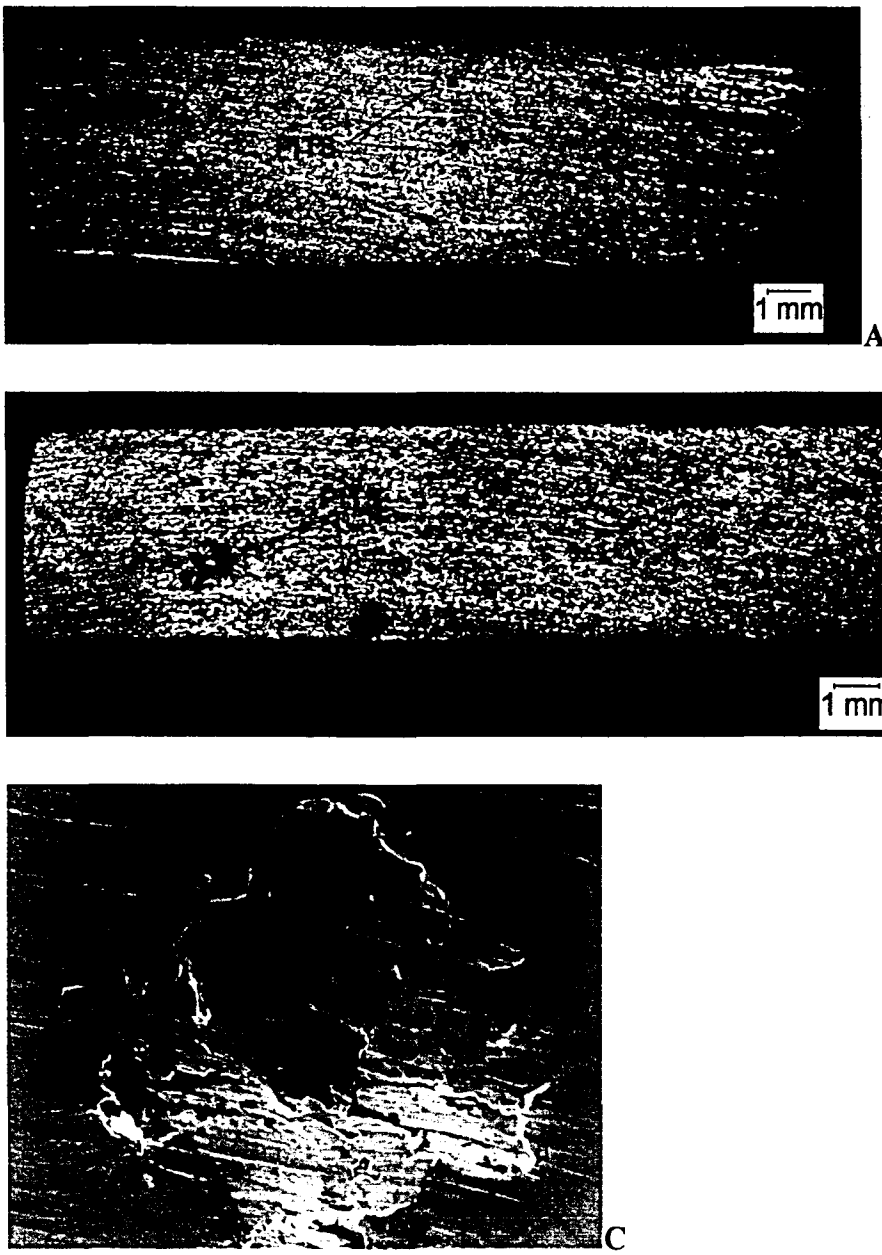

Fig. 4-20 A and B) Pits in AL-6XN base metal occurring at 70°C and C) a higher magnification of the pit seen in B) showing evidence of undercutting.

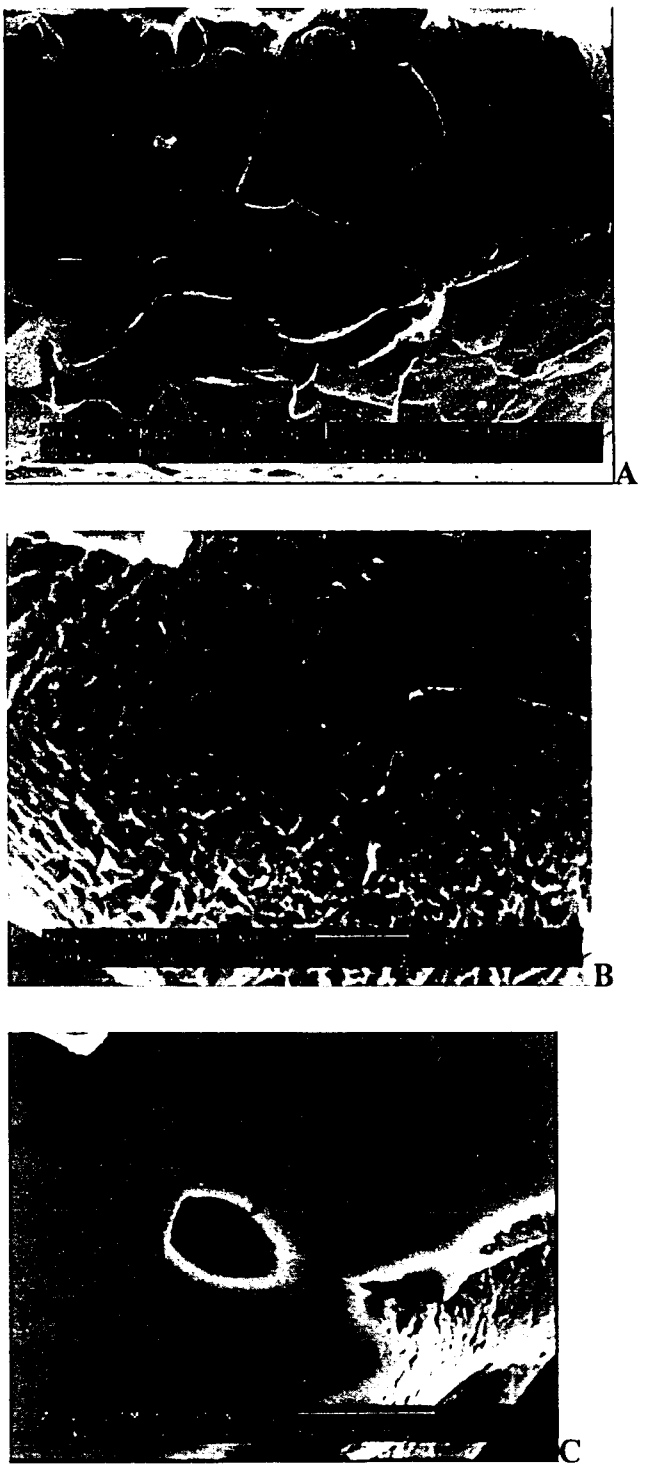

Fig. 4-21 The surface of the pits in AL-6XN plate showing A) faceted morphology and B) a dimpled morphology and C) a higher magnification of grain boundary attack at the pit edge.

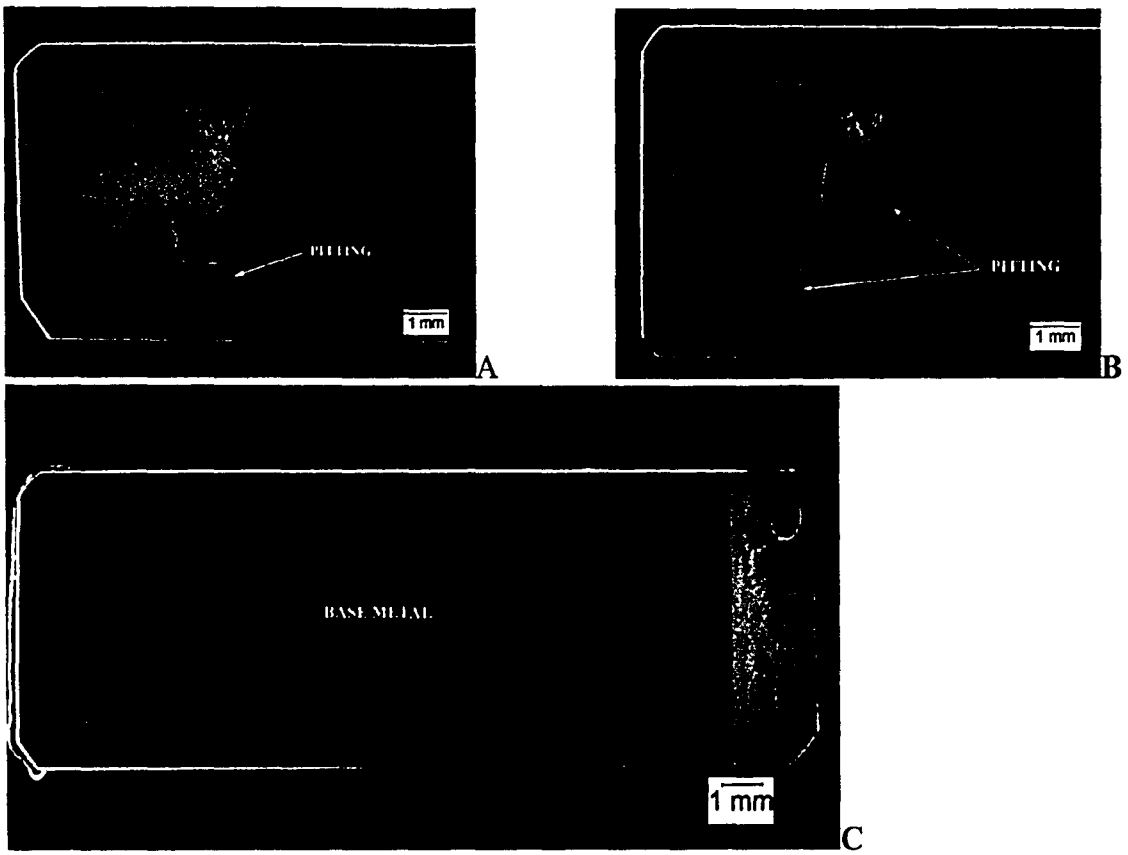

Fig. 4-22 Pitting at 55°C of the CPT samples at A and B) the worm hole and tungsten and C) the crown side of the FS weld.

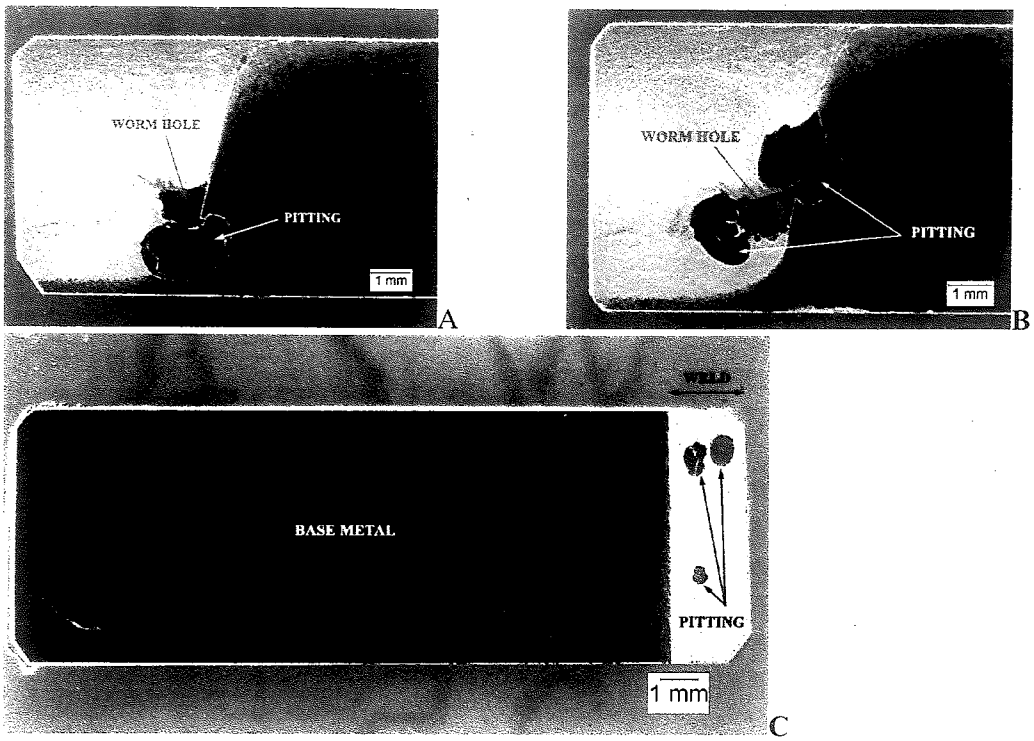

Fig. 4-22 Pitting at 55°C of the CPT samples at A and B) the worm hole and tungsten and C) the crown side of the FS weld.

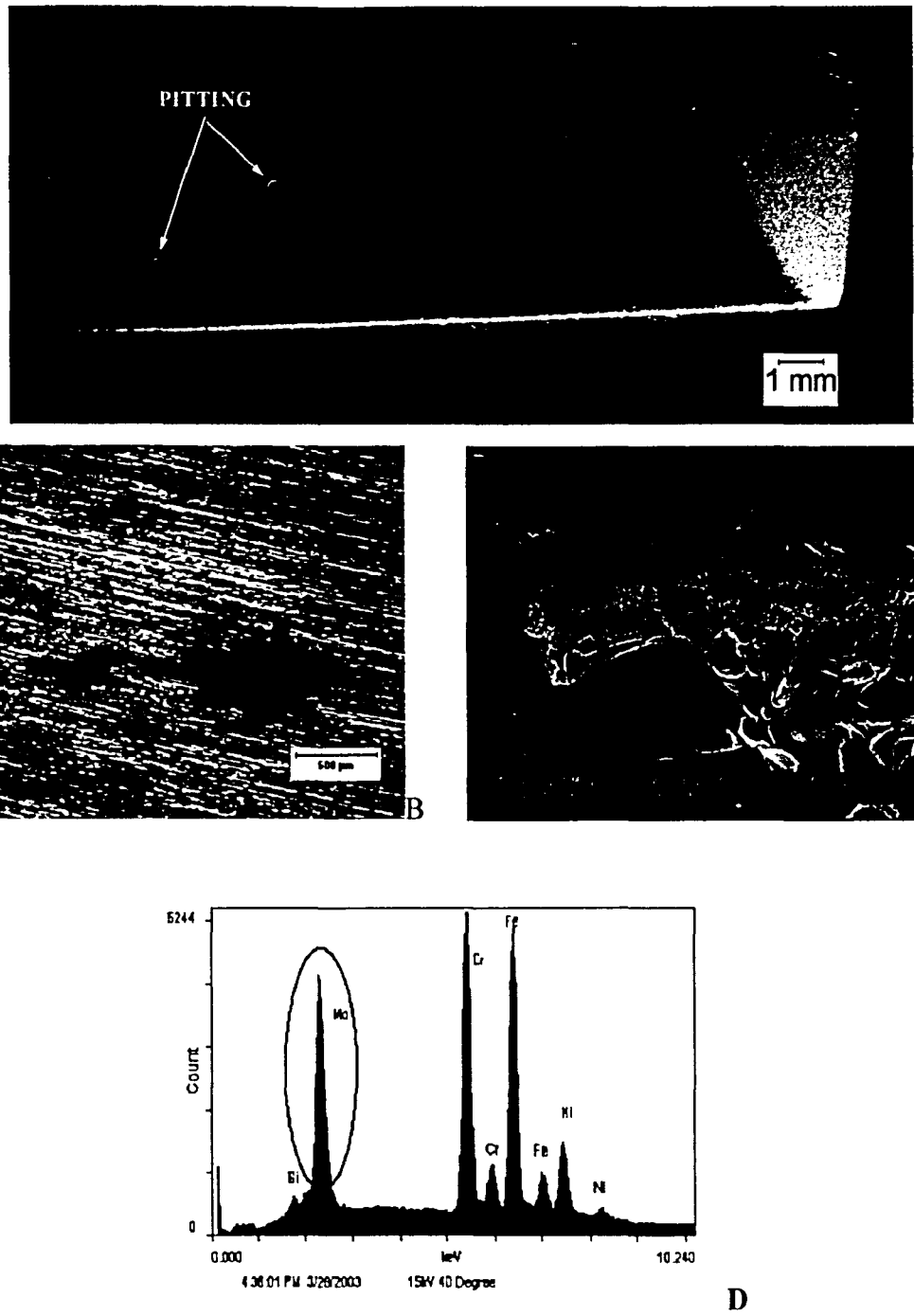

Fig. 4-23 A) Pitting in the CPT sample of the retreating side half weld on plate 1and B) the pitting in the CPT sample of the retreating side half weld on plate 2 showing pitting and C) an SEM image of the pit seen in B).

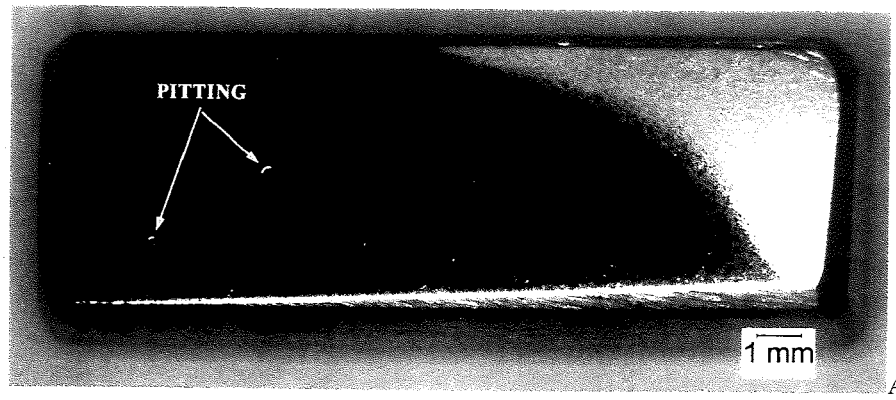

A

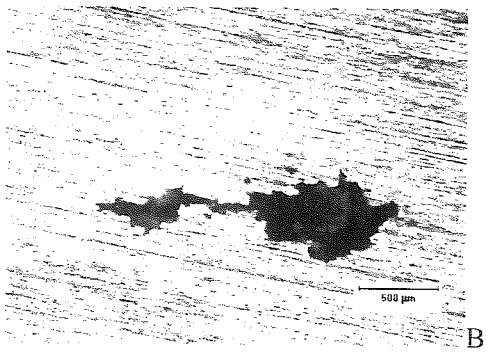

B

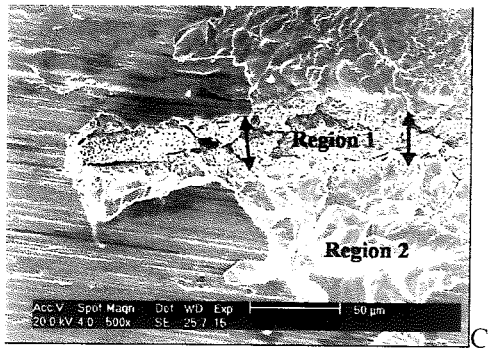

C

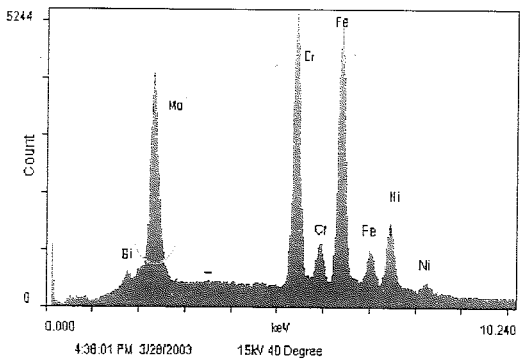

D

Fig. 4-23 A) Pitting in the CPT sample of the retreating side half weld on plate 1and B) the pitting in the CPT sample of the retreating side half weld on plate 2 showing pitting and C) an SEM image of the pit seen in B).

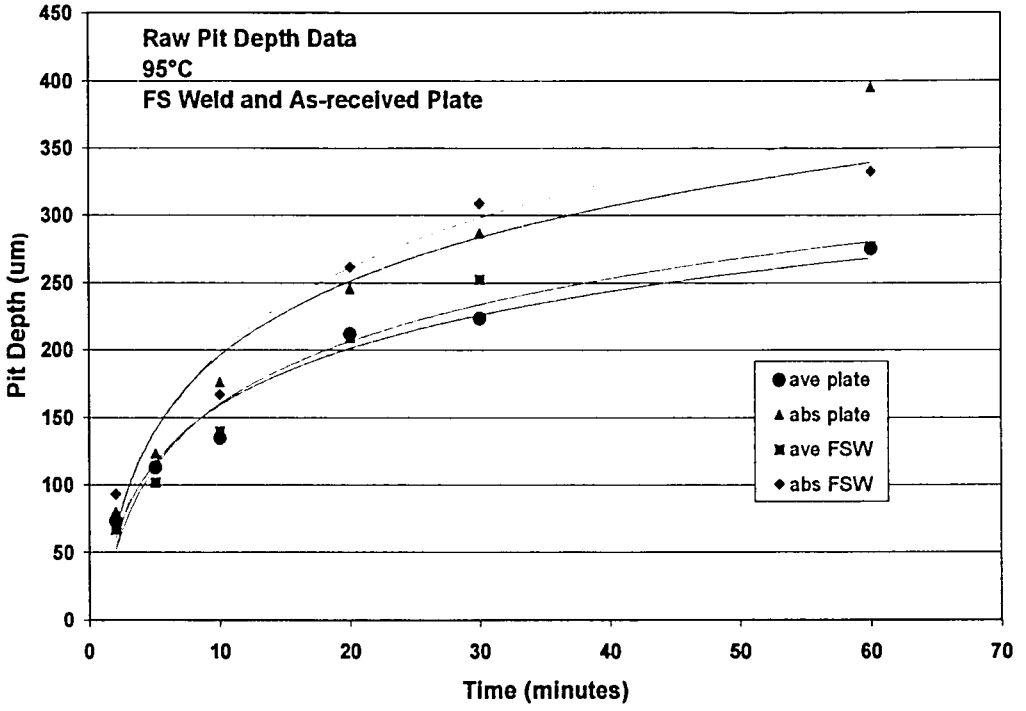

A

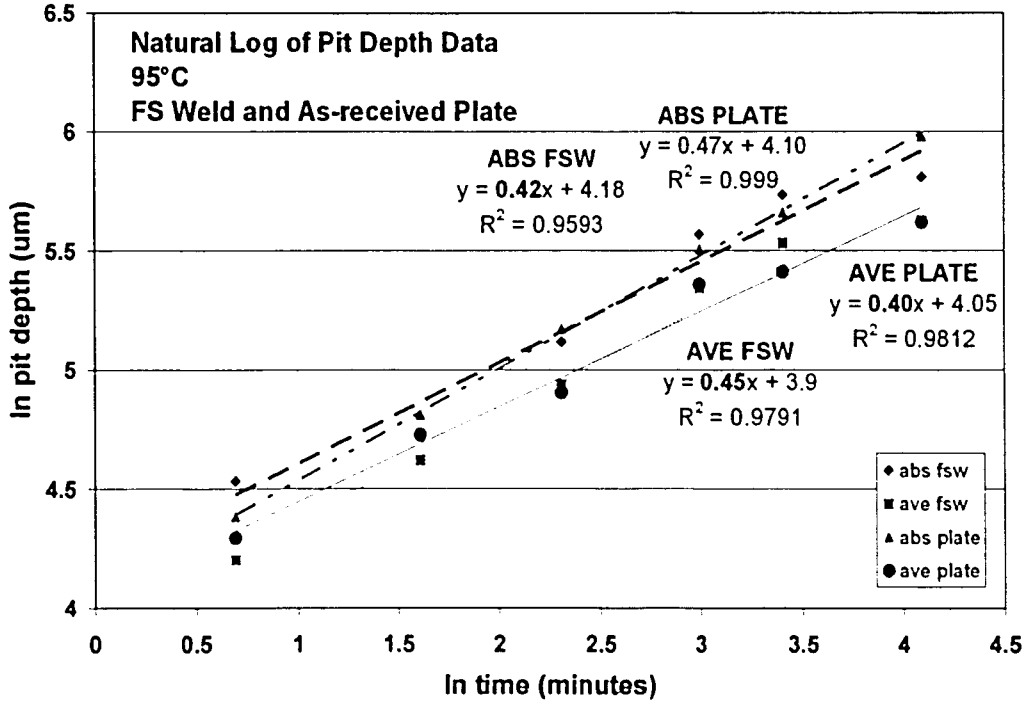

B

Fig. 4-24 The maximum pit depth plotted as a function of time with A) the raw data and B) the log values of the data.

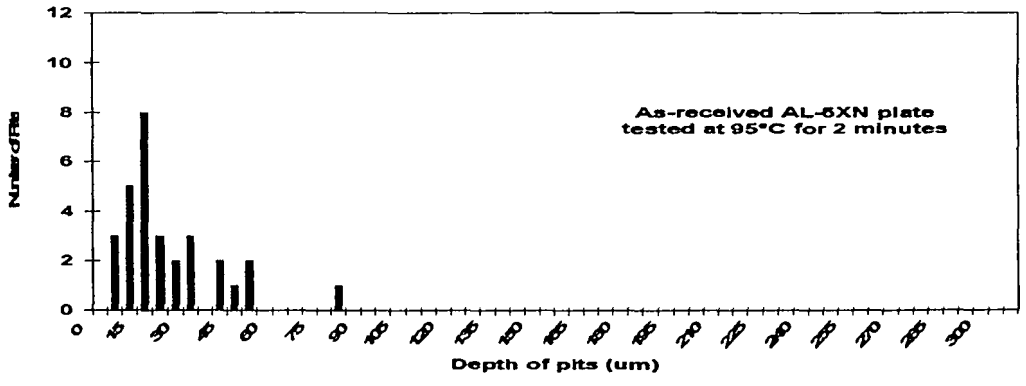

A

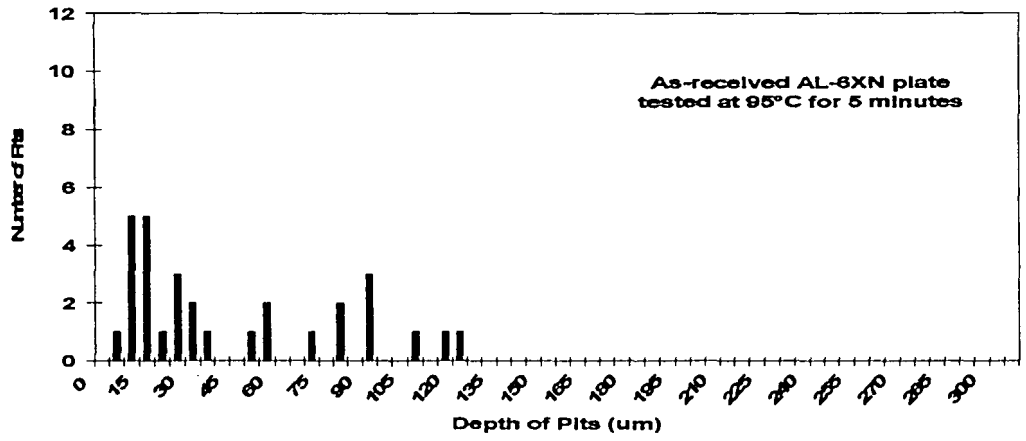

B

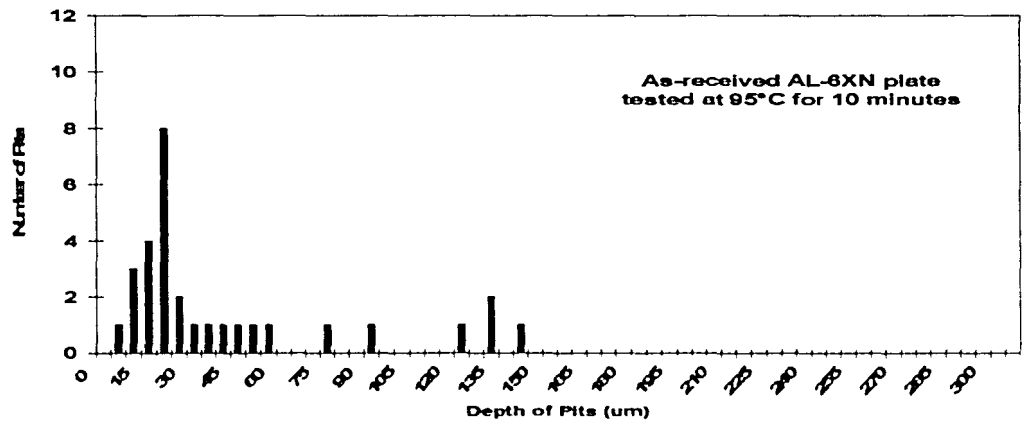

C

Fig. 4-25 The pit depth distributions for AL-6XN as-received plate tested at 95°C for times of A) 2, B) 5, and C) 10 minutes.

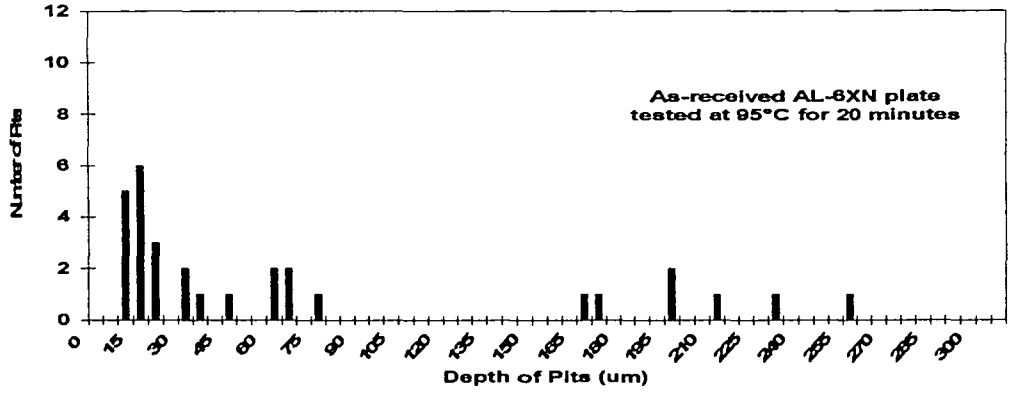

D

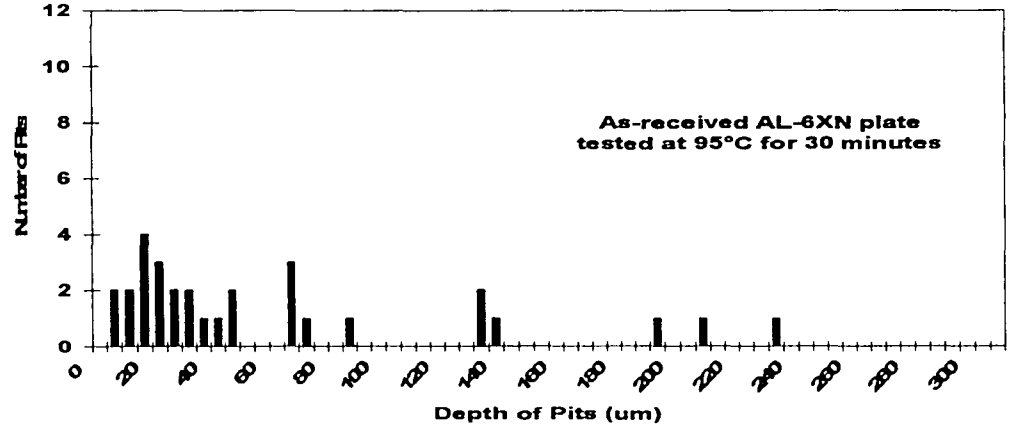

E

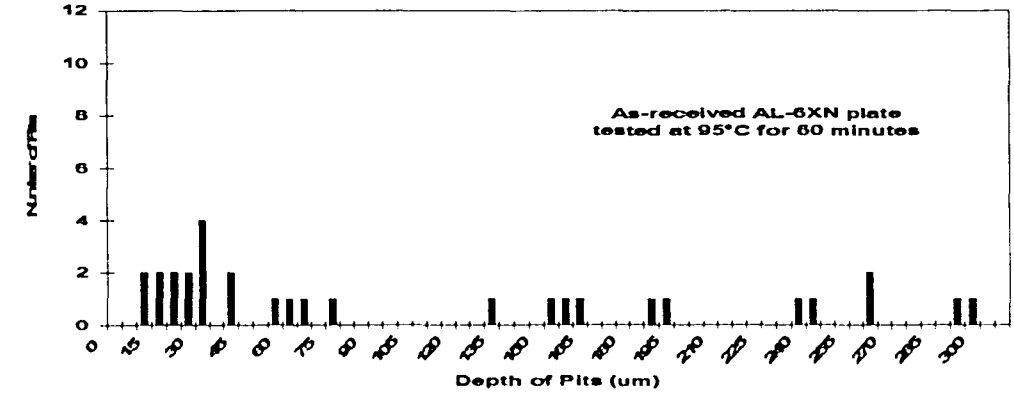

F

Fig. 4-25 The pit depth distributions for AL-6XN as-received plate tested at 95°C for times of D) 20, E) 30 and F) 60 minutes.

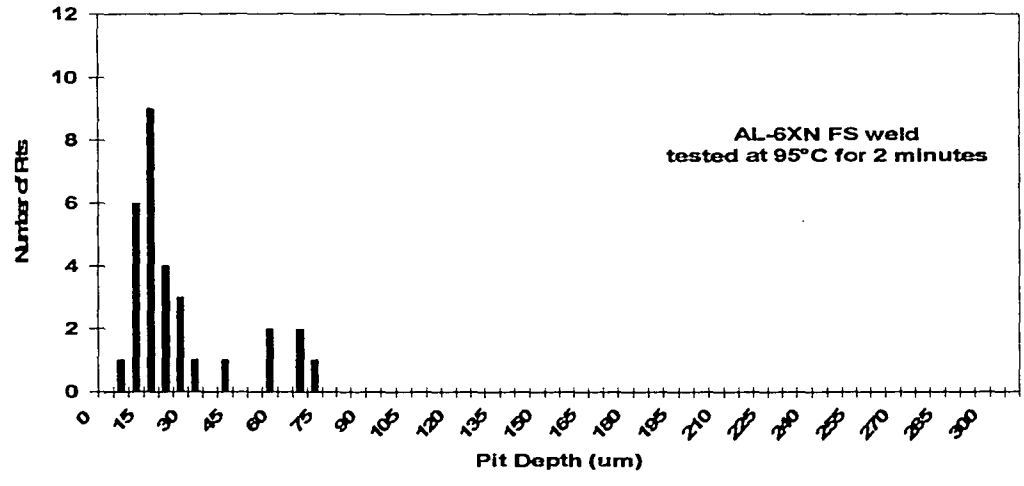

A

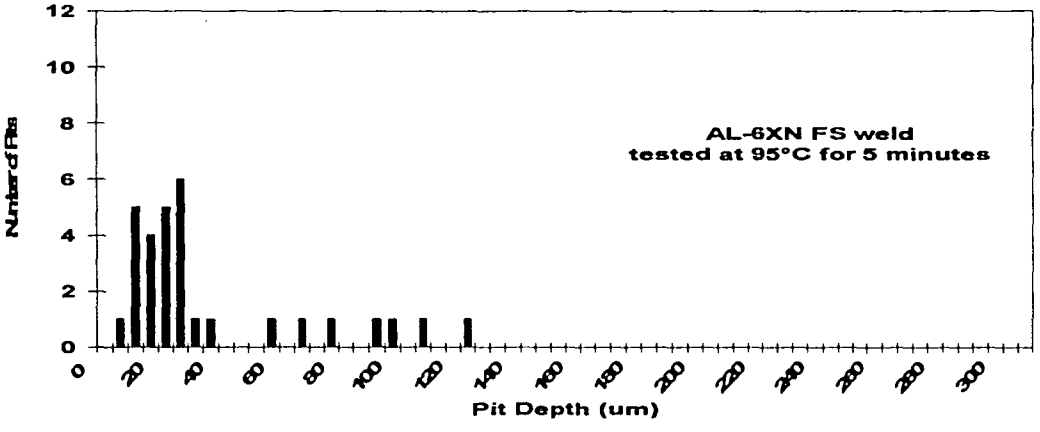

B

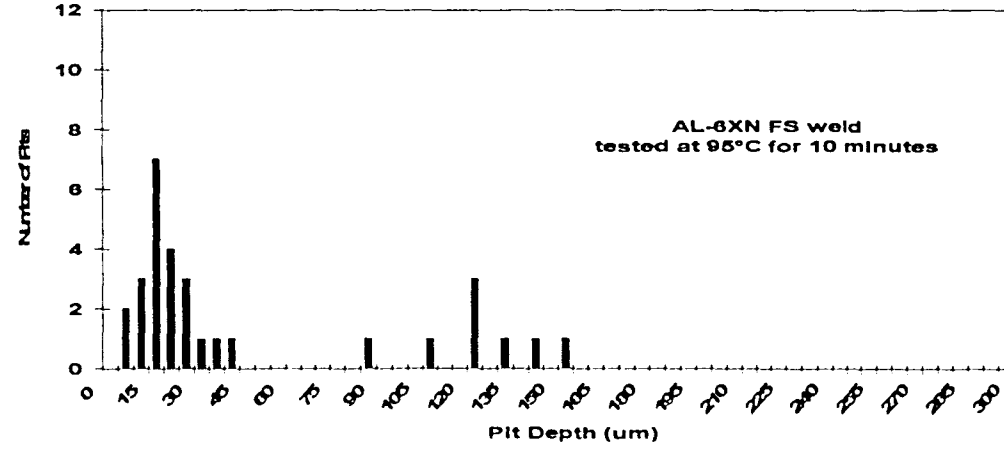

C

Fig. 4-26 The pit depth distributions for the FS weld tested at 95°C for times of A) 2, B) 5, and C) 10 minutes.

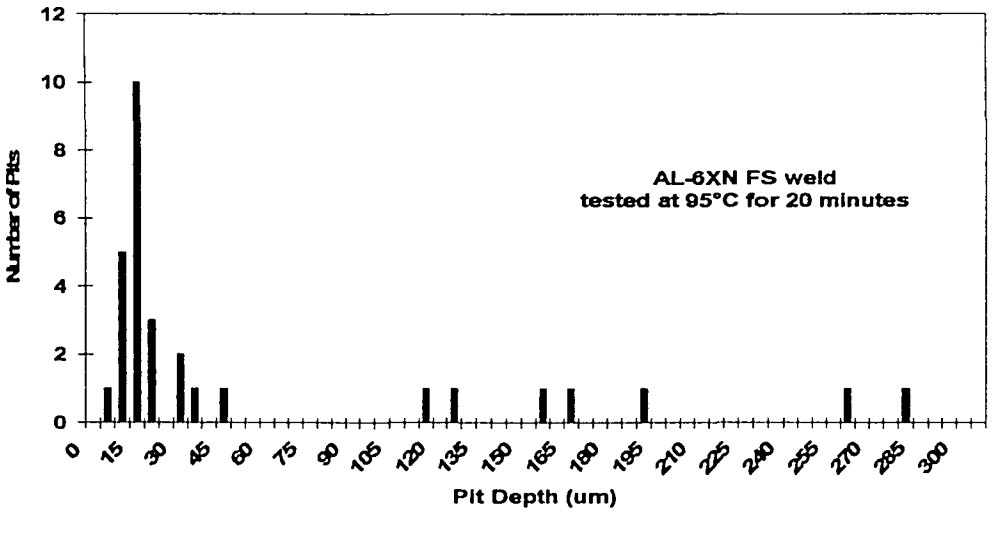

D

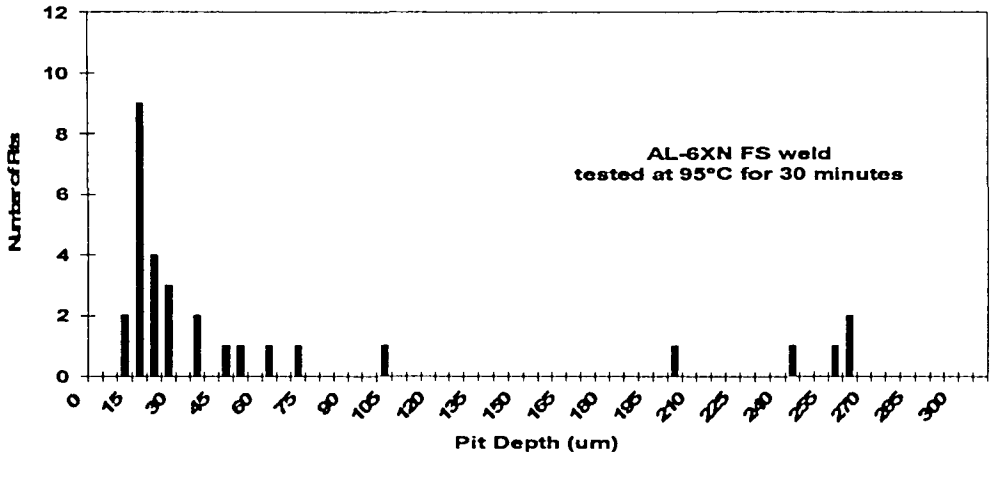

E

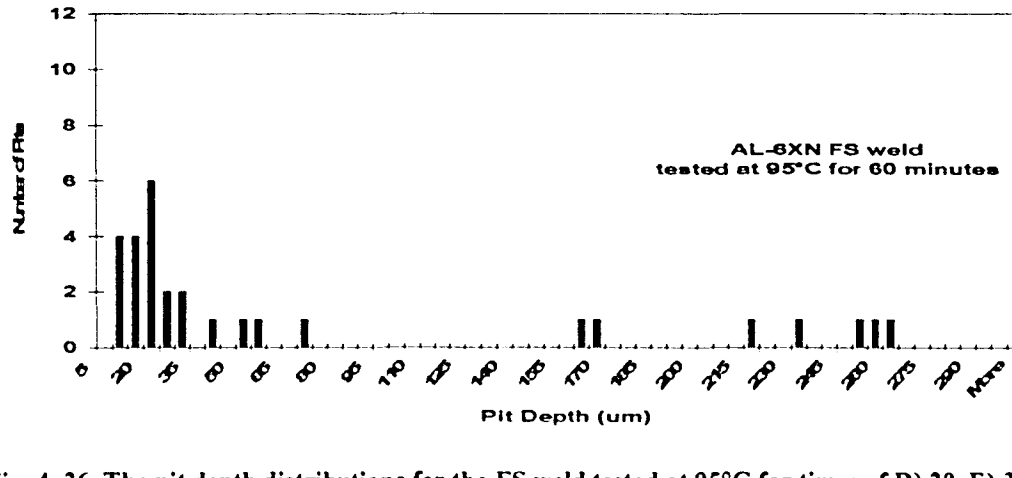

F

Fig. 4- 26 The pit depth distributions for the FS weld tested at 95°C for times of D) 20, E) 30 and F) 60 minutes.

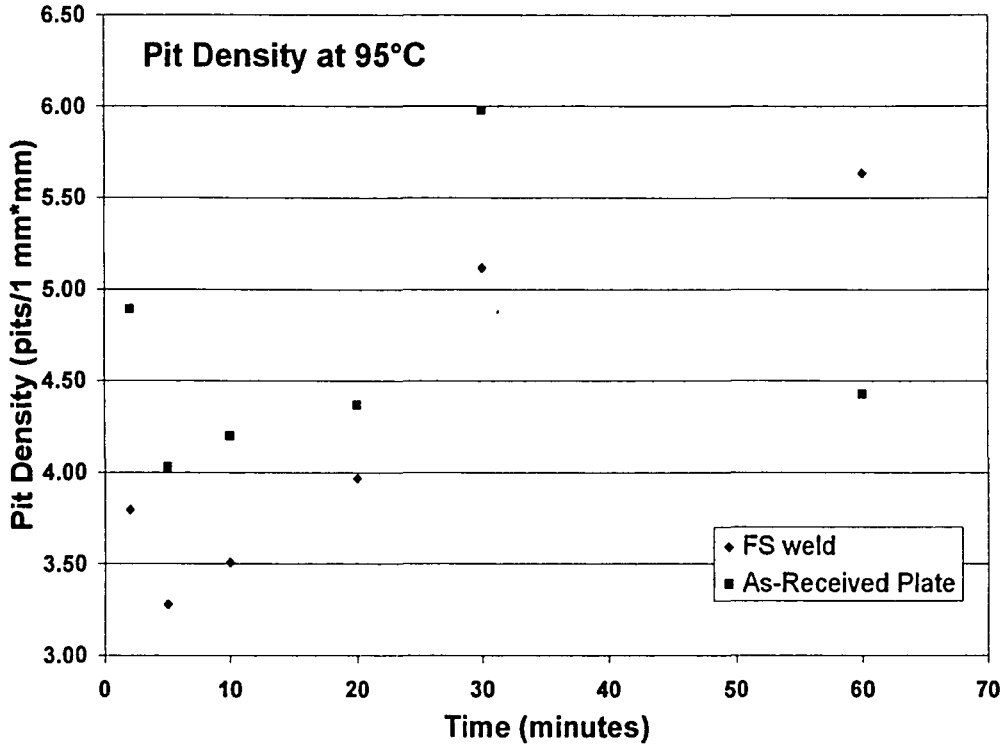

Fig. 4-27 The pit density of AL-6XN as-received plate and FS weld tested at 95°C.

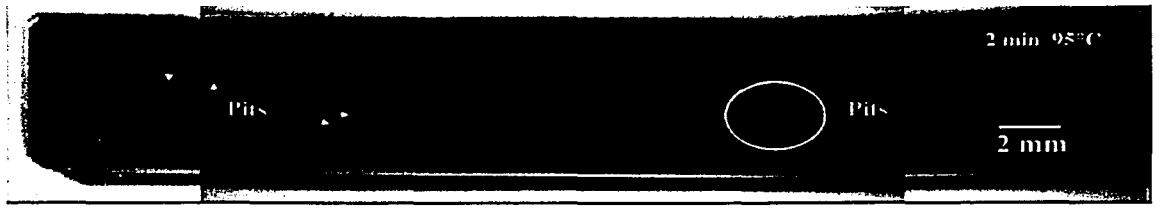

A

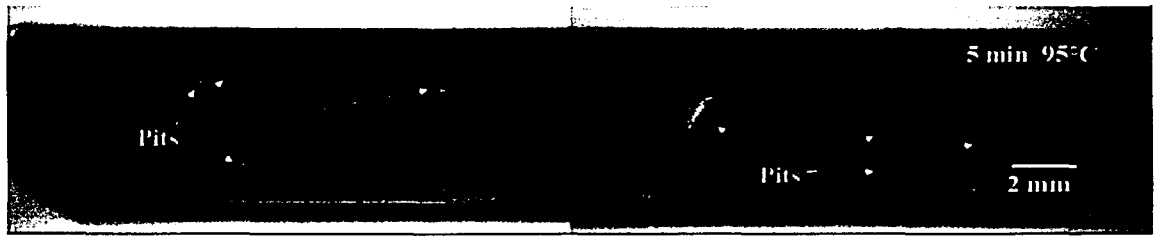

B

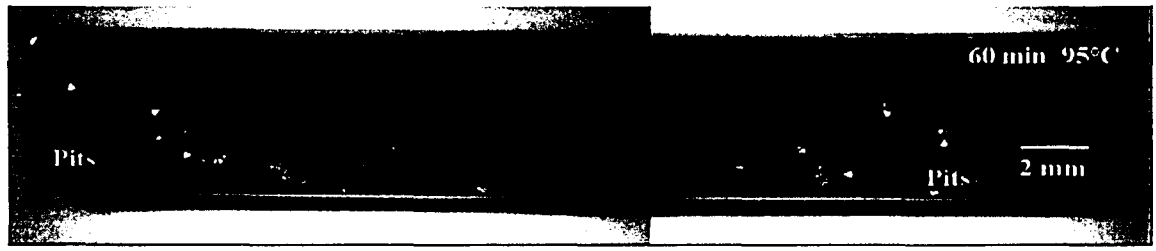

C

Fig. 4-28 Kinetics samples of A-C) AL-6XN FS weld tested at 95°C for 2, 5, and 60 minutes respectively.

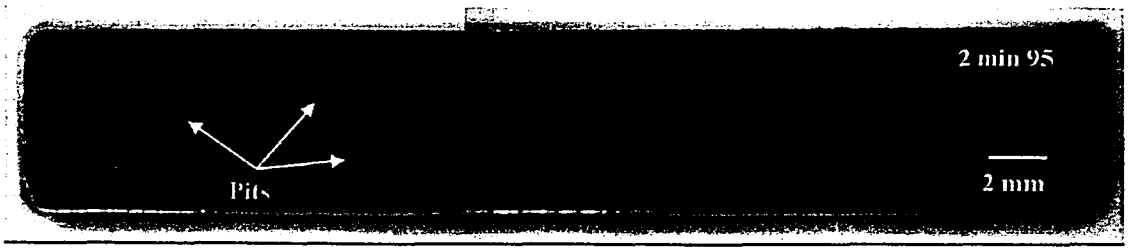

D

E

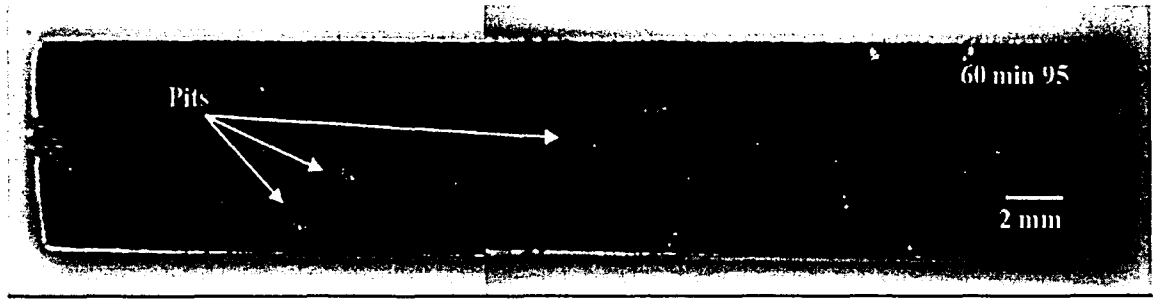

F

Fig. 4-28 Kinetics samples of D-F) as-received plate tested at 95°C for 2, 5, and 60 minutes respectively.

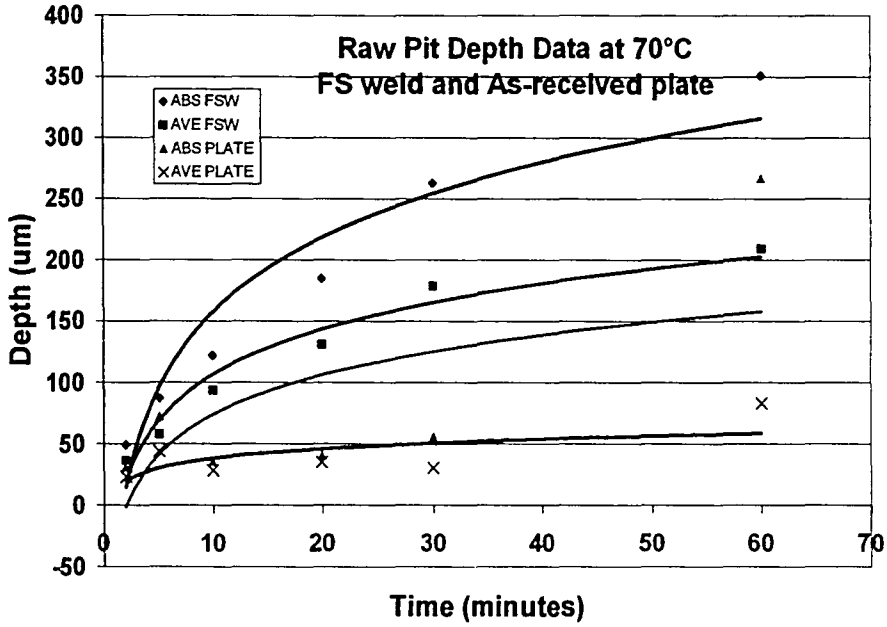

A

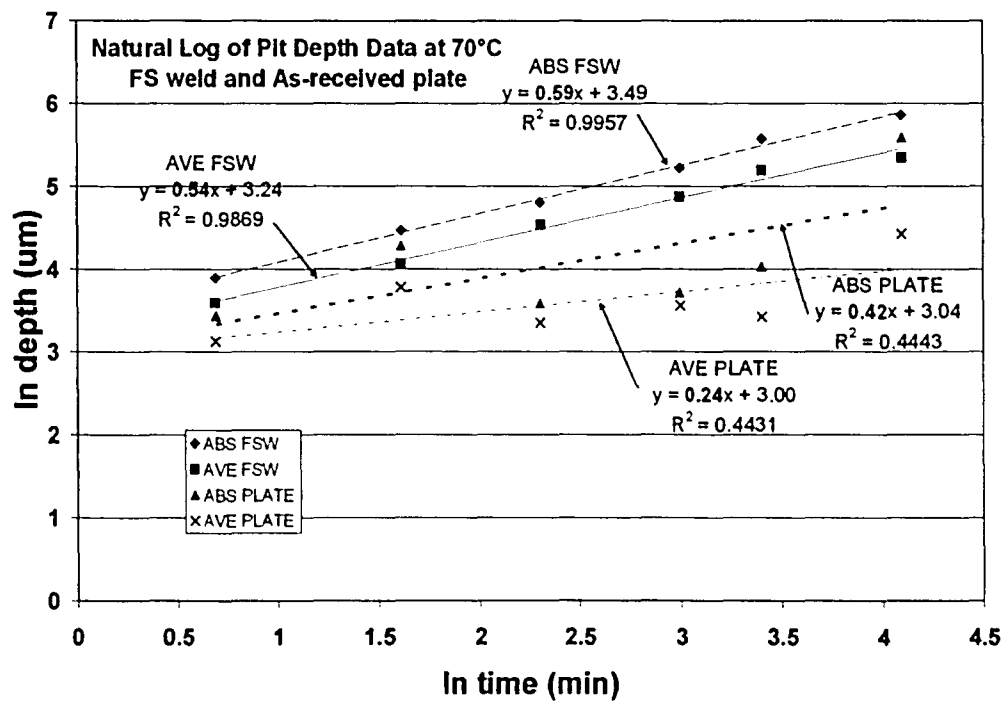

B

Fig. 4-29 The maximum pit depth at a test temperature of 70°C plotted as a function of time with A) the raw data and B) the log values of the data.

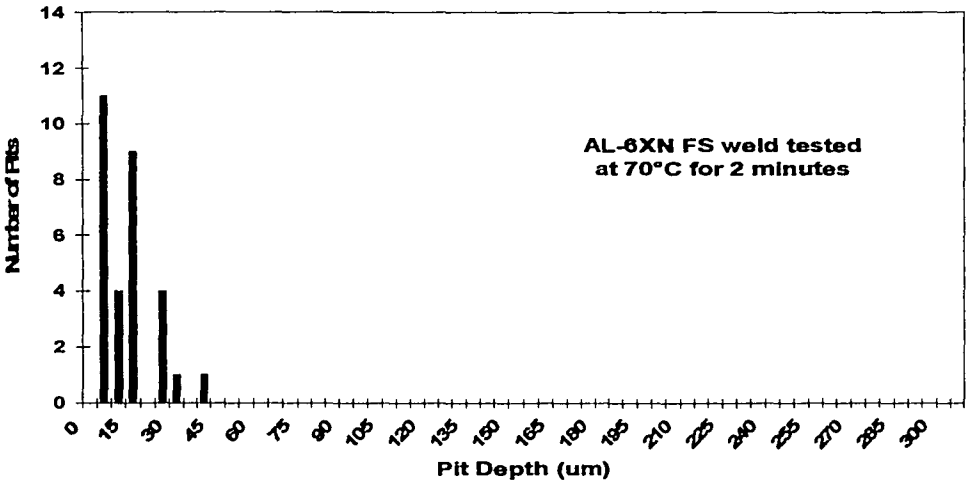

A

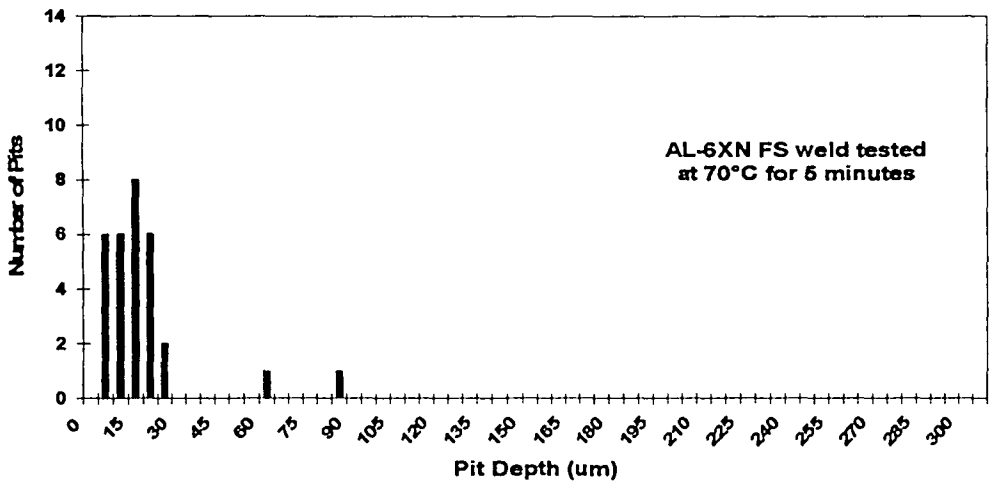

B

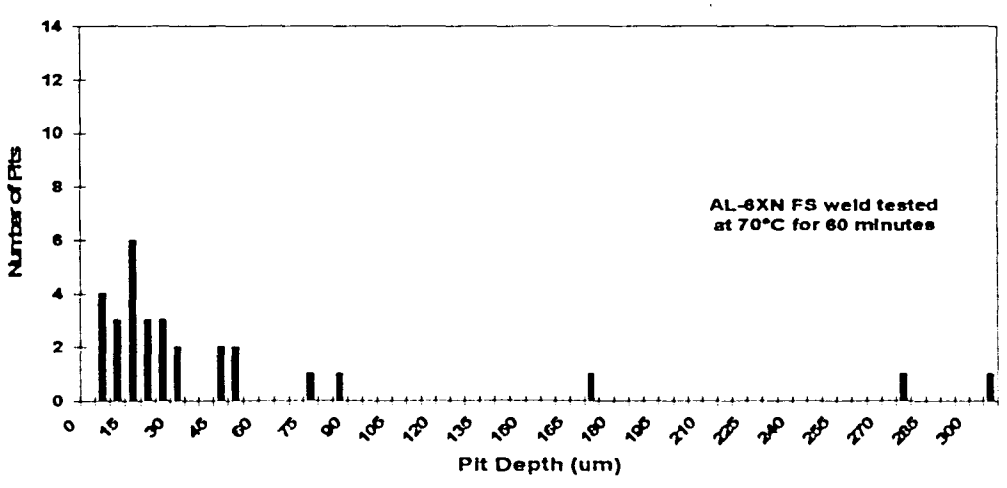

C

Fig. 4-30 The pit depth distributions for the FS weld tested at 70°C for times of A) 2, B) 5, and C) 60 minutes.

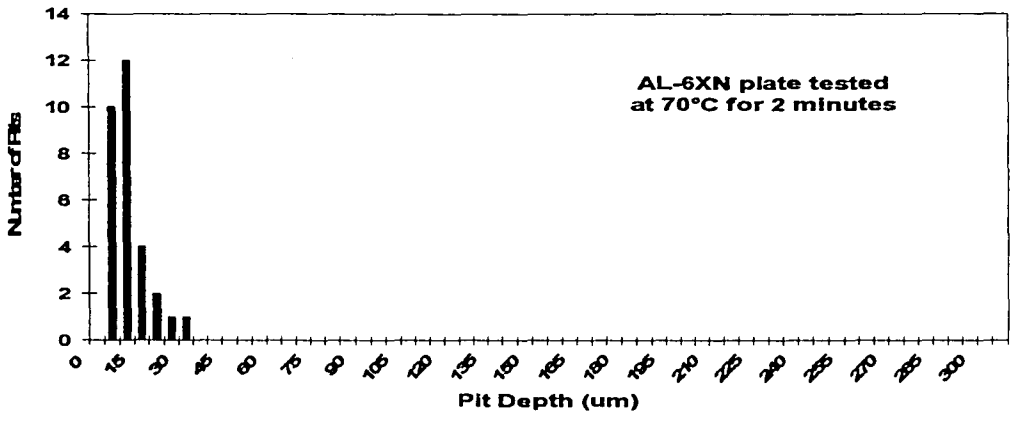

A

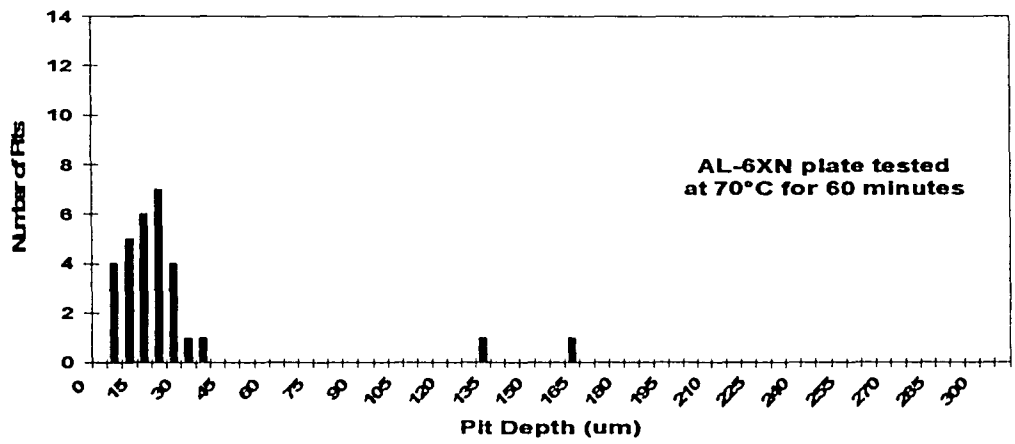

B

Fig. 4- 31 The pit depth distributions for the as-received plate at 70°C for times of A) 2 and C) 60 minutes.

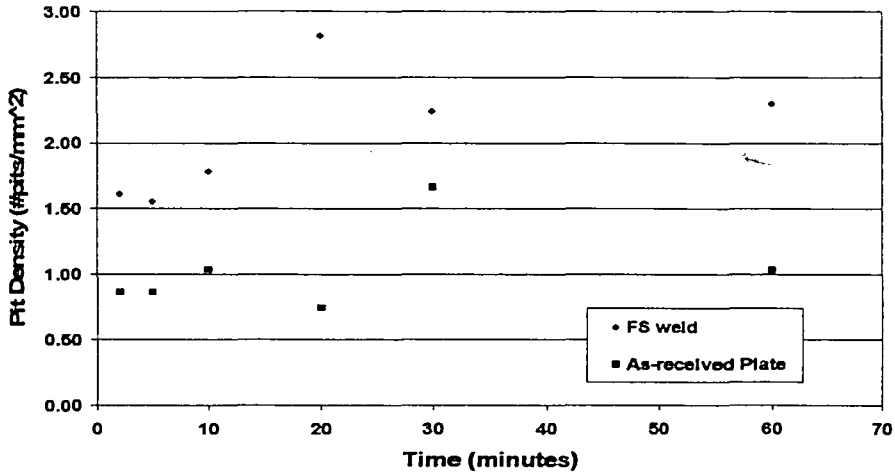

Fig. 4-32 The pit density of AL-6XN as-received plate and FS weld tested at 70°C.

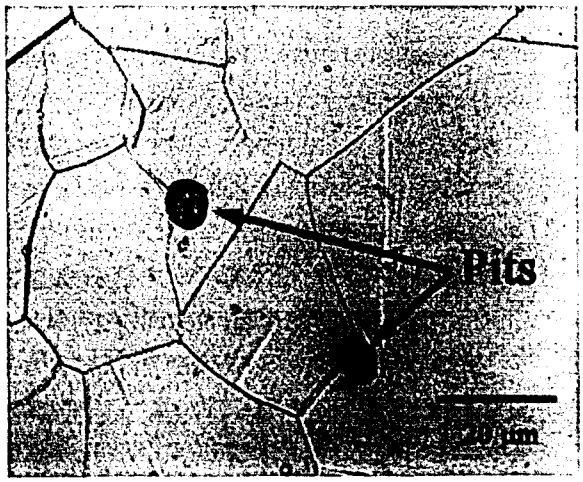

Fig. 4-33 Small pits located in the unaffected base metal in the FS weld samples tested at 70°C for 2 minutes.


A


B

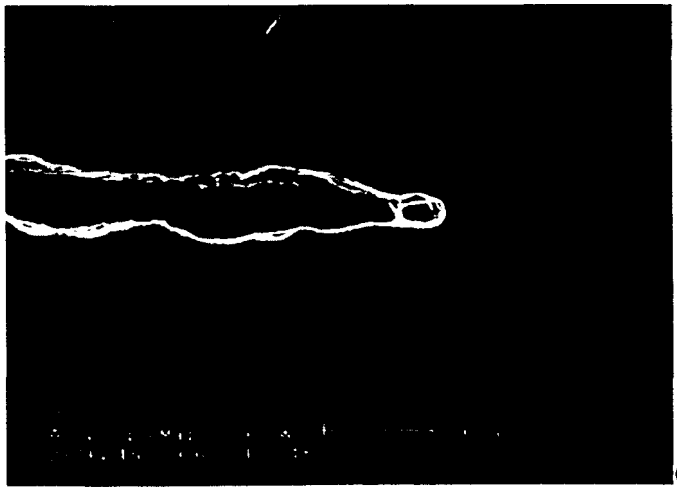
C

Fig. 4-34 A) LOM and B) SEM images of small pits at the grain boundaries in the HAZ after testing at 70°C for 2 minutes and C) high magnification image of the pit edge seen in B).


A


B

Fig. 4-35 Several pits in the TMAZ of the FS weld after testing at 70°C for 2 minutes at A) low magnification and B) higher magnification.

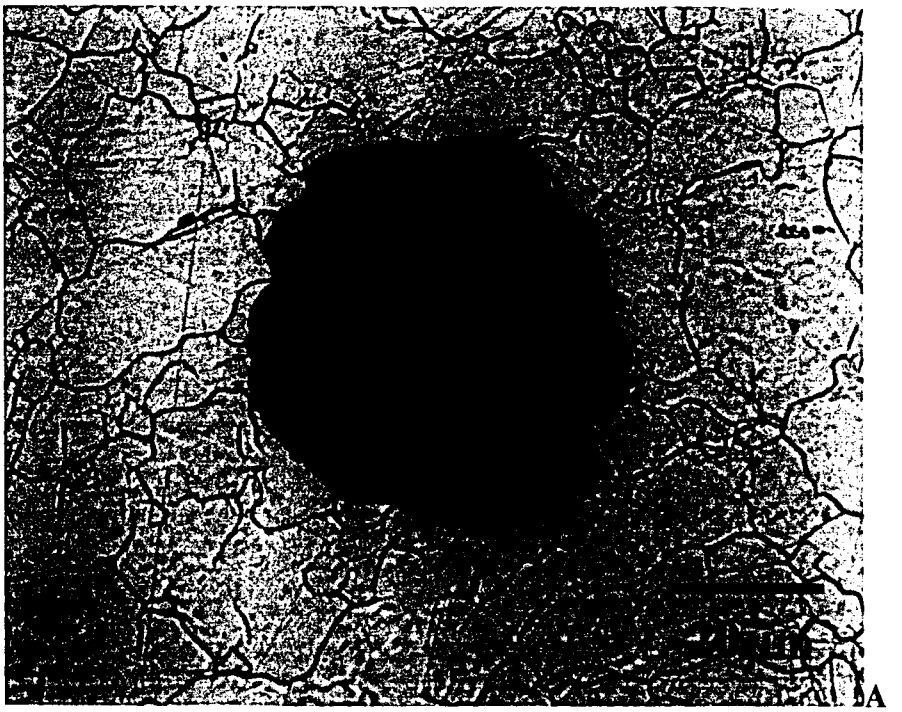

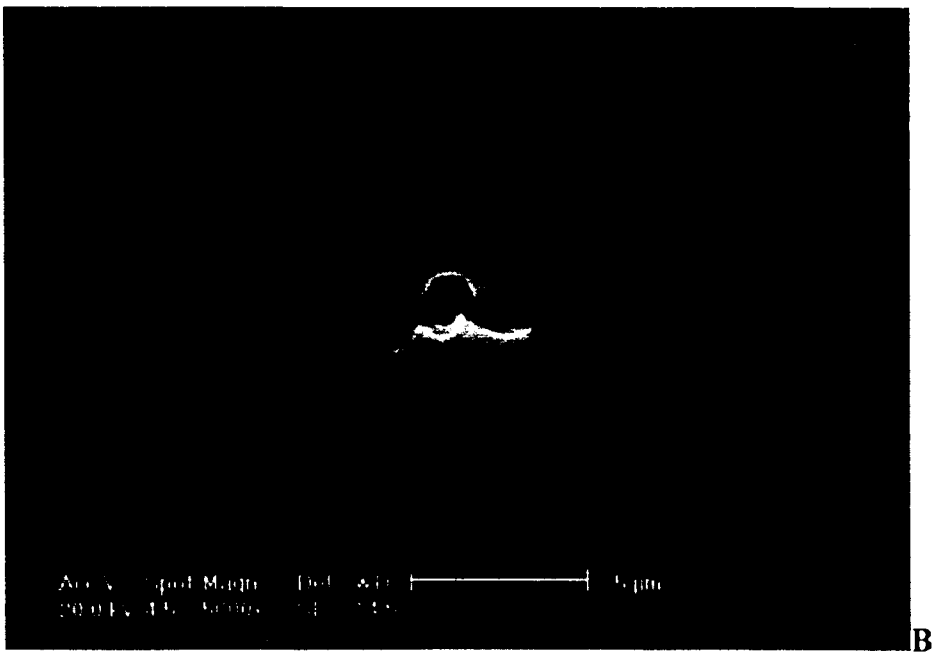

Fig. 4-36 A) LOM and B) SEM images of pits located in the nugget after testing at 70°C for 2 minutes.

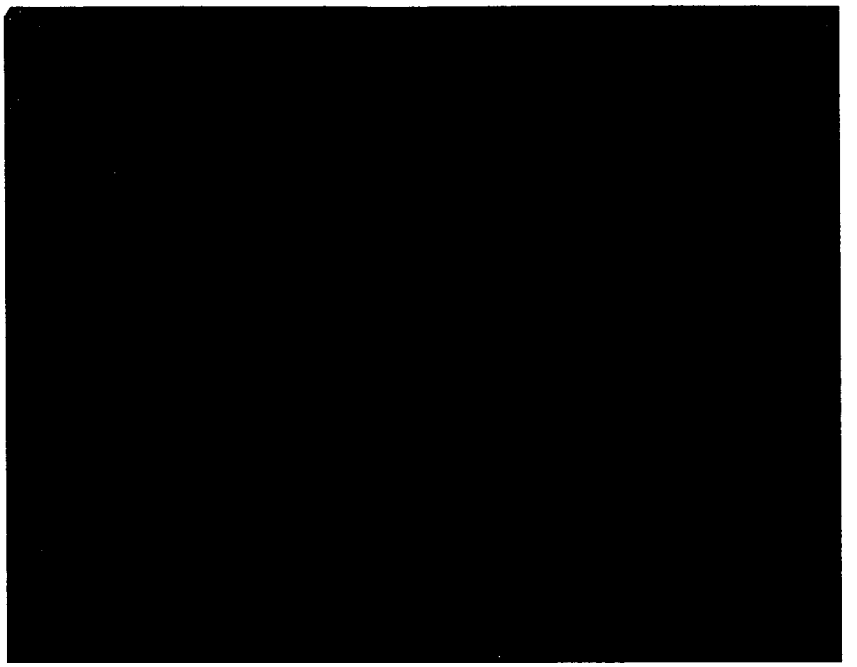

Fig. 4-37 Pit in the as-received plate after testing at 70°C for 2 minutes.

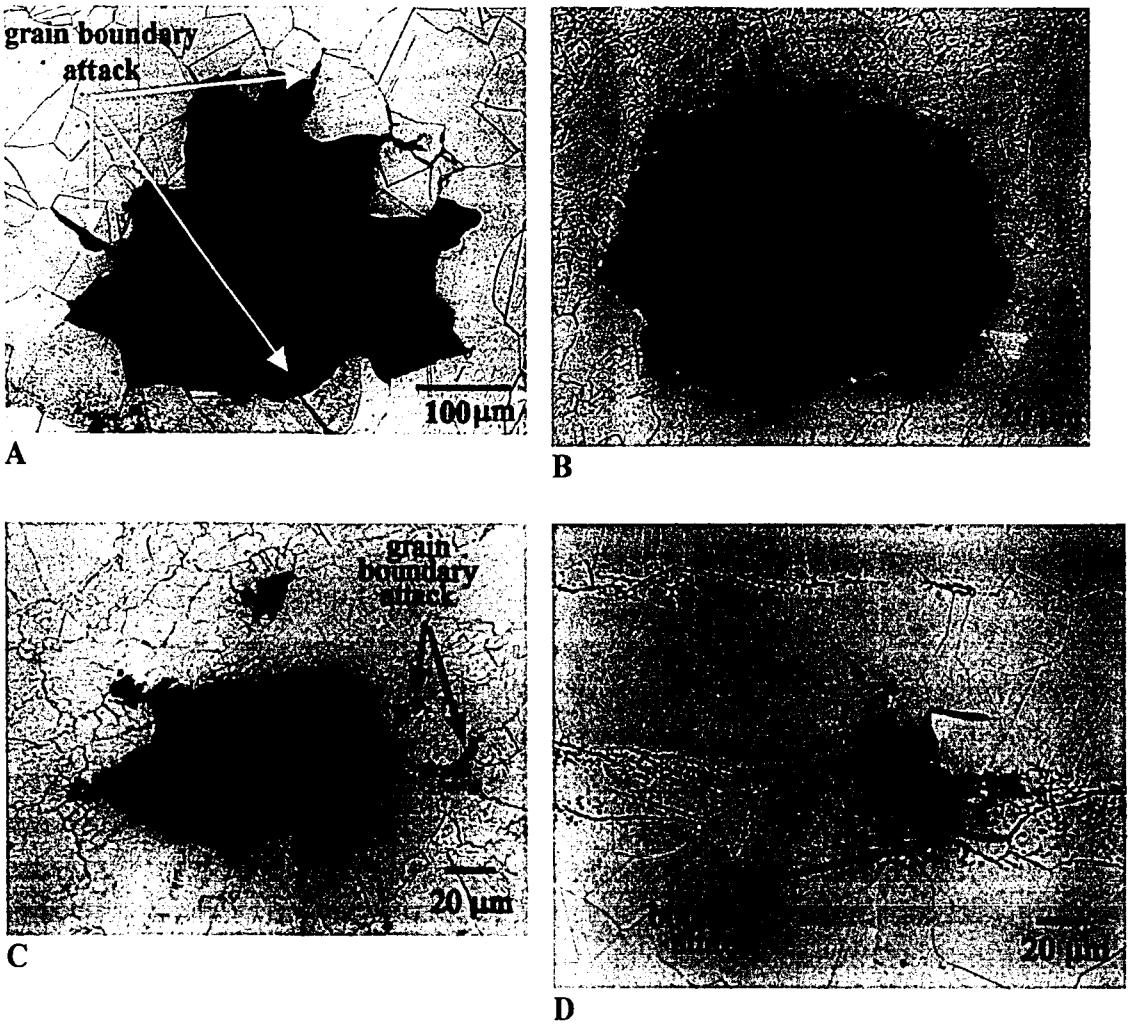

Fig. 4-38 Pitting in the AL-6XN FS weld after 60 minutes at 70°C of the A) base metal, B) TMAZ and HAZ, C) TMAZ, and D) sigma phase.

Fig. 4-39 Pit propagation in the as-received plate after 60 minutes at 70°C.

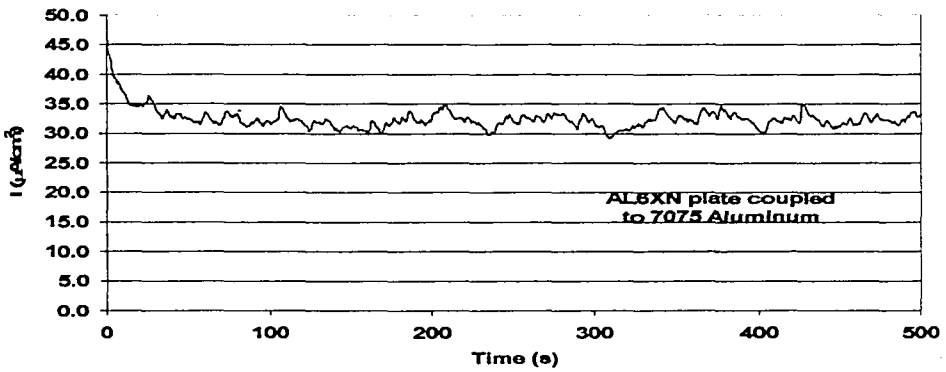

A

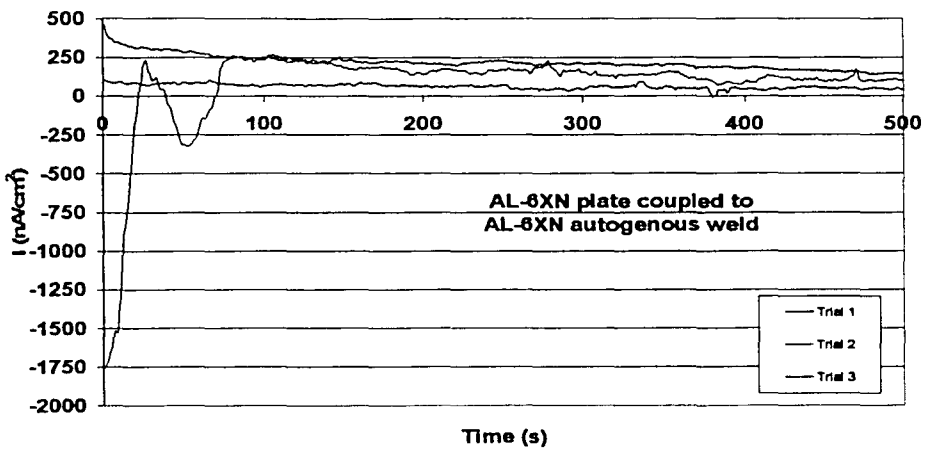

B

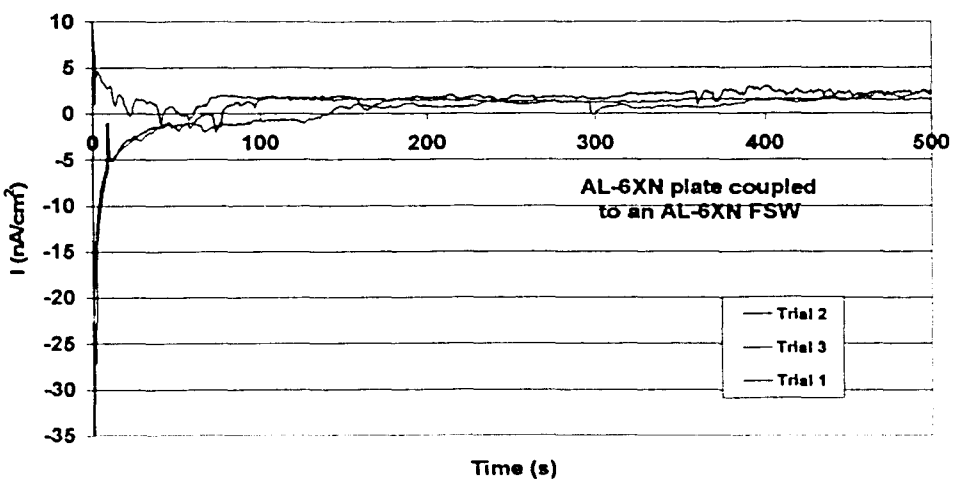

C

Fig. 4-40 Results of the galvanic corrosion experiment performed on AL-6XN plate coupled to A) 7075 aluminum, B) an autogenous weld on AL-6XN, and C) an AL-6XN FSW.

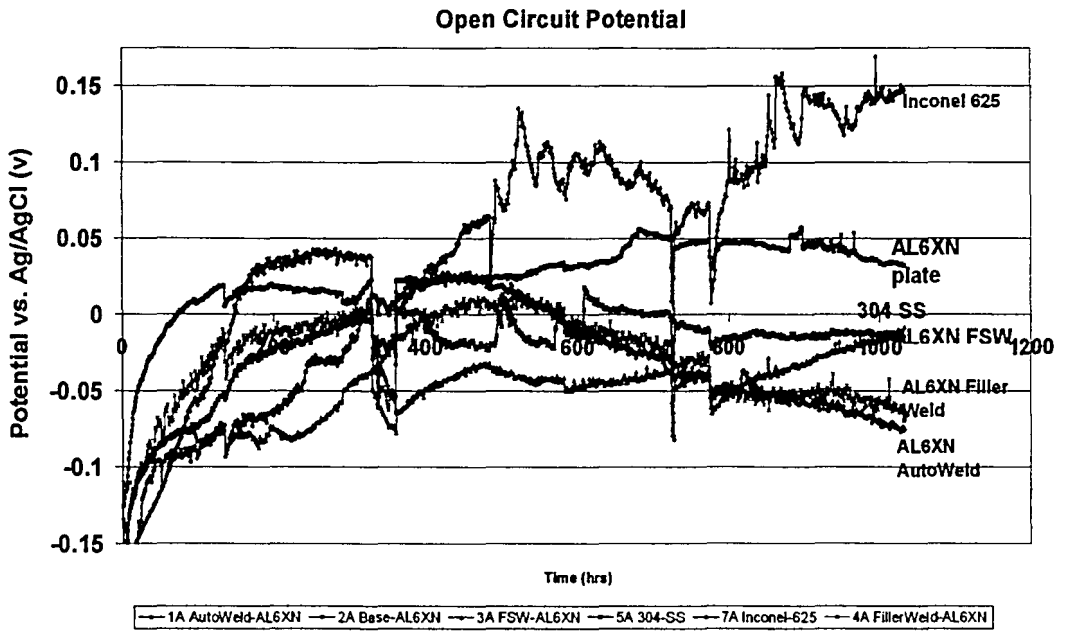

A

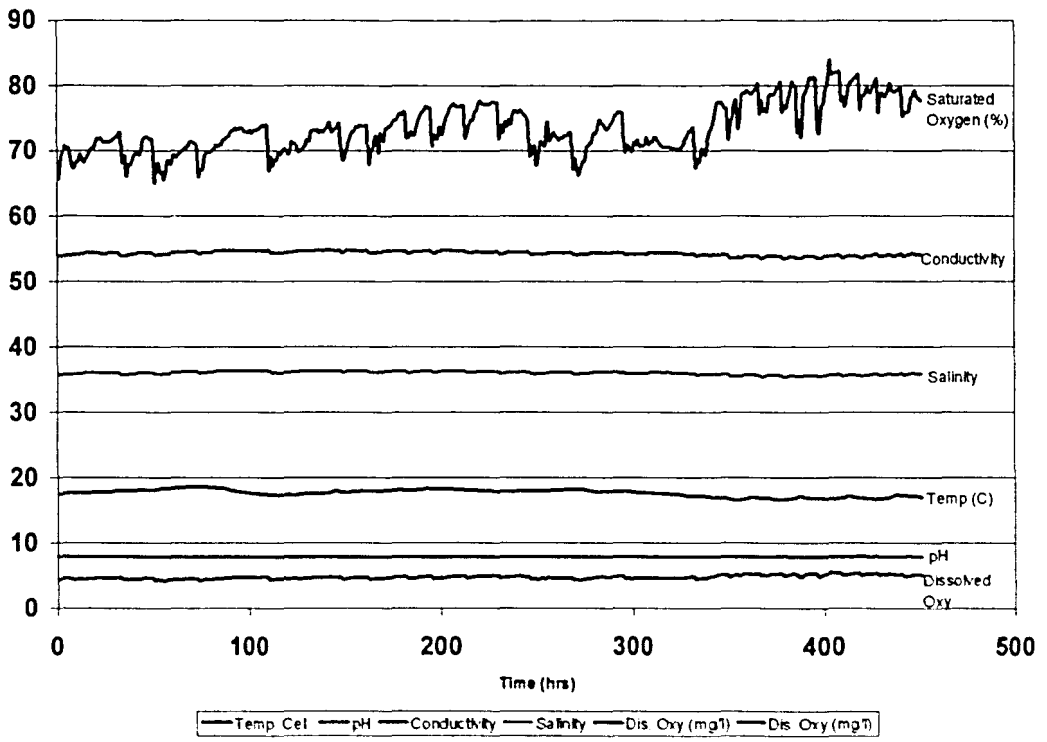

B

Fig. 4- 41 A) The OCP measured as a function of time for various samples in seawater and B) the tracking of critical test parameters during the OCP testing.

5. Conclusions

The microstructures of double-sided and single-sided FS welds on AL-6XN plate were characterized using LOM, SEM, and microhardness techniques. In addition, the pitting behavior of the single-sided FS welds was characterized. Significant results of the study are as follows:

1. The resulting microstructures of the single-sided and double-sided FS welds were similar but there were some notable differences caused by the difference in the required penetration depth.

2. For both welds, the intense deformation and temperatures experienced by the nugget produce a very fine microstructure of equiaxed grains.

3. Evident from the stream of tungsten based contaminates found in the microstructure of both welds, tool wear proves to be a significant problem in FSW of AL-6XN. The wear predominately occurs on the advancing side of the weld, possibly the result of a harsher environment compared to the retreating side. The distribution of tungsten in the double-sided weld is concentrated at one central streak while the it is dispersed throughout the nugget in the single-sided weld.

4. EPMA analysis confirms there is no microsegregation in any region of the double-sided weld and this can also be assumed to be true for the single-sided FS weld. This is significantly different than conventional arc welding where microsegregation is unavoidable when joining SASS.

5. The HAZ and the TMAZ are transition zones between the base metal and the nugget. The HAZ microstructure is characterized by large austenite grains similar to the base metal with recrystallization of austenite at grain boundaries. There are no apparent signs of deformation in this region. The TMAZ is simply a microstructural transition from the HAZ to the nugget. Approaching the weld centerline, effects of the increasing strains and higher temperatures produced during FSW are seen by the increased grain deformation and recrystallization at grain boundaries.

6. Microhardness traces reflect the microstructural changes in the different regions created during FSW. Generally, the base metal is softer than any weld affected region. Hardness increases towards the centerline, through the HAZ and TMAZ, as a result of increasing microstructural refinement. The fine-grained structure of the nugget yields maximum hardness.

7. The worm holes present in the single-sided welds are weld defects that can be avoided by altering weld parameters.

8. Although not directly determined, the CPT of the full FS weld is 55°C. This is much lower than the CPT of 70°C of as-received plate and is equal to the CPT of fusion welds made with a high alloy filler metal. Certain unavoidable microstructural features such as centerline sigma, the worm hole, and the tungsten based inclusions negatively influence the CPT. Evidence suggests that upon removal of these features, a CPT of 65°C may be attainable.

9. At 95°C, pit growth rates, pit distributions, and pit densities of the as-received plate and the FS weld are essentially the same indicating no difference in the corrosion

behavior. In the FS welds, however, it appears that some type of galvanic couple is formed between the weld zone and the base metal such that the base metal corrodes at the expense of the weld. The microstructural refinement in the nugget inhibits corrosion. The galvanic corrosion present here but not detected by electrochemical testing is a result of the test media.

10. In the as-received plate and the FS weld (regardless of microstructure), pits tend to initiate at and propagate along the grain boundaries at short exposure times in a ferric chloride solution. In the annealed or recrystallized structures of the AL-6XN, the grain boundaries are the sites of highest energy. Although, CPT tests cannot be used to determine pit initiation, it is clear that corrosion occurs preferentially at the weld defects and the grain boundary pit propagation is minimized.

11. The difference in the equilibrium currents of the as-received plate and the FS weld, as determine in OCP testing, is approximately 50 mV and suggests that FSW does sacrifice the corrosion behavior of AL-6XN plate. This joining method, however, proves to be superior to fusion welding.

12. From the variety of corrosion tests performed, it is apparent that the test media has a strong influence on the corrosion behavior. The corrosion tests which most closely approximate a realistic marine environment – galvanic and open circuit potential tests – suggest that the corrosion resistance of the AL-6XN FS weld is superior to that of AL-6XN fusion welds.

Reference List

1. W. M. Thomas, E.D.Nicholas, J.C.Needham, M.G.Murch, P.Templesmith, and C.J.Dawes. Friction Stir Butt Welding. [U.S Patent No. 5,460,317] (1991).

2. W.M.Thomas, P.L.Threadgill, and E.D.Nicholas, Feasibility of Friction Stir Welding Steel. *Science and Technology of Welding and Joining* **4**, 365-372 (1999).

3. A.F.Norman, I.Brough, and P.B.Prangnell, High Resolution EBSD Analysis of the Grain Structure in an AA2024 Friction Stir Weld. *Materials Science Forum* **331-337**, 1713-1718 (2000).

4. T.J.Lienert, JR. W.L.Stellwag, B.B.Grimmett, and R.W.Warke, Friction Stir Welding Studies on Mild Steel. *Welding Journal* **82**, 1S-9S (2003).

5. Y.Li, L.E.Murr, and J.C.McClure, Flow Visualization and Residual Microstructures Associated With the Friction-Stir Welding of 2024 Aluminum to 6061 Aluminum. *Materials Science & Engineering A* **271**, 213-223 (1999).

6. A.P.Reynolds, W.D.Lockwood, and T.U.Seidel, Processing-Property Correlation In Friction Stir Welds. *Materials Science Forum* **331-337**, 1719-1724 (2000).

7. B.Heinz, B.Skrotzki, and G.Eggeler, Microstructural and Mechanical Characterization of A Friction Stir Welded Al-Alloy. *Materials Science Forum* **331-337**, 1757-1762 (2000).

8. E.D.Nicholas and W.M.Thomas, A Review of Friction Processes For Aerospace Applications. *International Journal of Materials and Product Technology* **13**, 45-55 (1998).

9. A.P.Reynolds, Visualisation of Material Flow In Autogenous Friction Stir Welds. *Science and Technology of Welding and Joining* **5**, 120-124 (2000).

10. K.Colligan, Material Flow Behavior During Friction Stir Welding of Aluminum. *Welding Research* 229-s-237-s (1999).

11. C.G.Rhodes, M.W.Mahoney, W.H.Bingel, R.A.Spurling, and C.C.Bampton, Effects Of Friction Stir Welding On Microstructure of 7075 Aluminum. *Scripta Materialia* **36**, 69-75 (1997).

12. R.Fenn and W.M.Thomas, The Friction Stir Welding Process. *Light Metals Age* **59**, 28-33 (2001).

13. M.A.Sutton, B.Yang, A., Reynolds, and R.Taylor, Microstructural Studies of Friction Stir Weld In 2024-T3 Aluminum. *Materials Science & Engineering A* **A323**, 160-166 (2002).

14. J.E.Hatch, Aluminum - Properties and Phyical Metallurgy. *ASM Metals Park Ohio* (1984).

15. R.Dif, B.Des, D.Daniel, P.Lassince, and H.Ribes, *Materials Science Forum* **483**, 331-337 (2000).

16. L.Litynska, R.Braun, G.Staniek, C.DalleDonne, and J.Dutkiewicz, TEM Study of the Microstructure Evolution In a Friction Stir-welded AlCuMgAg Alloy. *Materials Chemistry and Physics* **81**, 293-295 (2003).

17. I.Charit and R.S.Mishra, High Strain Rate Superplasticity In a Commercial 2024 Al Alloy Via Friction Stir Processing. *Materials Science & Engineering A* **A359**, 290-296 (2003).

18. Y.J.Kwon, N.Saito, and I.Shigematsu, Friction Sitr Process as a new Manufacturing Technique of Ultrafine Grained Aluminum Alloy. *Journal of Materials Science Letters* **21**, 1473-1476 (2002).

19. Y.S.Sato, M.Urata, H.Kokawa, K.Ikeda, and M.Enomoto, Retention of Fine Grained Microstructure of Equal Channel Angular Pressed Aluminum Alloy 1050 by Friction Stir Welding. *Scripta Materialia* **45**, 109-114 (2001).

20. L.E.Murr, Y.Li, E.A Trillo, R.D.Flores, and J.C.McClure, Microstructures In Friction-Stir Welded Metals. *Journal of Materials Processing & Manufacturing Science* **7**, 145-161 (1998).

21. I.Woo, M.Aritoshi, and Y.Kikuchi, Metallurgical and Mechanical Properties of High Nitrogen Austenitic Stainless Steel Friction Welds. *ISIJ International* **42**, 401-406 (2002).

22. S. Stoltz. The What, Where and How of Friction Stir Welding. II, 469-472. 2000. ET 2000: Seventh International Aluminum Extrusion Technology Seminar. (2000).

23. A.P.Reynolds, Wei Tang, T.Gnaupel-Herold, and H.Prask, Structure, Properties, and Residual Stress of 304L Stainless Steel Friction Stir Welds. *Scripta Materialia* **48**, 1289-1294 (2003).

24. M.Posada, J.DeLoach, A.P.Reynolds, M.Skinner, and J.P.Halpin. Friction Stir Weld Evaluation of DH-36 and Stainless Steel Weldments. Friction Stir Welding and Processing, 159-171 (2001).

25. S.C.Park, Y.S.Sato, H.Kokawa, K.Okamoto, S.Hirano, and M.Inagaki, Rapid Formation of the Sigma Phase in 304 Stainless Steel During Friction Stir Welding. *Scripta Materialia* **Submitted for publication 2003**, (2003).

26. Avesta Stainless Steels, Information Brochure no. 7945. Sweeden, Avesta Jernverks, (1979)

27. M.Posada, J.DeLoach, A.P.Reynolds, and J.Halpin. Mechanical Property and Micrstructural Evaluation of Friction Stir Welded AL-6XN, 6th International Trends in Welding Research Conference Proceedings 307-311. (2003).

28. H.H.Uhlig and R.W.Revie, *Corrosion and Corrosion Control*, John Wiley & Sons, Inc., New York (1985).

29. B.D.Craig, Kinetics Of Corrosion. In *Fundametal Aspects of Corrosion Films In Corrosion Science*pp 27-46. Plenum Press, New York (1991).

30. M.G.Fontana, Modern Theory-Priciples. In , Third Edn.pp 445-481. McGraw-Hill Publishing Company, New York (1986).

31. H.Uhlig, Passivity In Metals and Alloys. *Corrosion Science* **19**, 777-791 (1979).

32. J.Kruger, Passivity of Metals - A materials Science Perspective. *International Materials Reviews* **33**, 113-130 (1988).

33. C.L.McBee and J.Kruger, Passivity and its Breakdown on Iron and Iron Base Alloys. *NACE* (1976).

34. J.Kruger, Effect of the Nature of the Passive Film On Fe and FeCr Alloys On Breakdown - A Breif Review. In pp 184-199. The Johns Hopkins University, Balitmore Mayland (2003).

35. B.D.Craig, Thermodynamics of Corrosion. In *Fundametal Aspects Of Corrosion Films In Corrosion Science*pp 1-26. Plenum Press, New York (1991).

36. D.A.Jones, Thermodynamics. In *Priciples and Prevention In Corrosion*, Second Edn,pp 40-74. Prentice Hall, Upper Saddle River (1996).

37. D.A.Jones, Passivity. In *Priciples and Prevention In Corrosion*, Second Edition Edn,pp 116-142. Prentice Hall, Upper Saddle River (1996).

38. B.E.Wilde and E.Williams, The Use of Current /Voltage Curves For The Study of Localized Corrosion and Passivity Breakdown On Stainless Steels In Chloride Media. *Electrochemica Acta* **16**, 1971-1985 (1985).

39. G.S.Frankel, Pitting Corrosion of Metals. *Journal of Electrochemcial Society* **145**, 2186-2197 (1998).

40. D.A.Jones, Pitting and Crevice Corrosion. In *Principles and Prvention of Corrosion*, Second Edn,pp 199-234. Prentice Hall, Upper Saddle River (1996).

41. B.D.Criag, Films and Pitting Corrosion. In *Fundametal Aspects Of Corrosion Films In Corrosion Scicncc*pp 109-128. Plenum Press, New York (1991).

42. T.P.Hoar, *Corrosion Scicnce* **5**, 279 (1965).

43. H.Strehblow, Mechanisms of Pitting Corrosion. In *Corrosion Mechanisms In Theory and Practice* ed. by P.Marcus and J.Oudar, pp 201-238. Marcel Dekker, Inc., New York (1995).

44. N.Sato, Theory For Breakdown Of Anodic Oxide Films On Metals. *Electrochem Acta* **16**, 1683-1692 (1971).

45. J.A.Richardson and G.C.Wood, Study Of the Pitting Corrosion of Aluminum By Scanning Electron Microscopy. *Corrosion Science* **10**, 313-323 (1970).

46. M.G.Fontana, Eight Forms of Corrosion. In *Corrosion Engineering*, Third Edn,pp 39-90. McGraw-Hill Publishing Company, New York (1986).

47. B.MacDougall and M.J.Graham, Growth And Stability of Passive Films. In *Corrosion Mechanisms In Theory and Practice* ed. by P.Marcus and J.Oudar, 143-174. Marcel Dekker, Inc., New York (1995).

48. H.H.Uhlig and R.Revie, Passivity. In *Corrosion and Corrosion Control*, Third Edn,pp 60-89. John Wiley & Sons, Inc., New York (1985).

49. D.A.Jones, Corrosion In Selected Corrosive Environments. In *Principles and Prevention of Corrosion*, 2nd Edn,pp 357-398. Prentice Hall, (1992).

50. A.J.Sedriks, *Corrosion of Stainless Steels*, New York (1996).

51. M.Stern, *Corrosion* **14**, (1958).

52. H.H.Uhlig and R.W.Revie, Polarization and Corrosion Rates. In *Corrosion and Corrosion Control*, Third Edn, 35-59. John Wiley & Sons, Inc., New York (1985).

53. A.Garner, The Effect of Autogenous Welding on Chloride Pitting Coroosion in Austenitic Stainless Steels. *Corrosion* **35**, 108-114 (1979).

54. M.Smialowski, Smialowski, M.Rychcik, and A.Szummer, Effect of Sulphide Inclusions In a Commercial Stianless Steel on the Nucleation of Corrosion Pits. *Corrosion Science* **9**, 123-125 (1969).

55. T.Suter and H.Bohni, A New Microelectrochemical Method to Study Pit Initiation on Stainless Steels. *Electrochemica Acta* **42**, (1997).

56. V.A.C.Haanappel and M.F.Stroosnijder, Influence of Mechanical Deformation of the Corrosion Behavior of AISI 304 Stainless Steel Obtained from Cooking Utensils. *Corrosion* **57**, (2001).

57. D.A.Jones, Galvanic and Concentration Cell Corrosion. In *Principles and Prevention of Corrosion*, 2nd Edn,pp 168-198. Prentice Hall, (1992).

58. A.J.Sedriks, Pitting. In *Corrosion of Stainless Steels* (1996).

59. ASTM G150-99: "Standard Test Method for Electrochemical Critical Pitting Temperature Testing of Stainless Steels". *American Society for Testing and Materials* (1999).

60. ASTM G48-97: "Standard Test Methods for Pitting and Crevice Corrosion of Stianless Steels and Related Alloys by Use of Ferric Chloride Solution". *American Society for Testing and Materials* (1997).

61. M.Liljas, Development of Superaustenitic Stainless Steels. *Welding In the World* **36**, 55-63 (1995).

62. R.M.Davison and J.D.Redmond, Practical Guide to using 6 Mo Austenitic Stainless Steels. *Materials Performance* (1988).

63. A.Garner, Corrosion of high Alloy Austenitic Stainless Steel Weldments in Oxidizing Environments. *Welding Journal* (2003).

64. A.J.Sedriks, New Stainless Steels for Seawater Service: *Corrosion* (1989).

65. A.J.Sedriks and P.J.Dudt, Corrosion Resistance, Coating, and Magnetic Property Issues of Nonmagnetic Austenitic Stainless Steels for Ship Hulls. *Corrosion* **57**, 84-91 (2001).

66. A.J.Sedriks, *International Materials Reviews* **27**, (1982).

67. R.M Kain. Crevice Corrosion Behavior of Stainless Steel in Natural Seawater. 2000. NACE. Corrosion (2000).

68. M.F.de Romero, O.T.de Rincon, F.Z.Duque, and P.Bohorquez, Super Stainless Steel, Ti, and Cu-10% Ni Alloys in Brackish Water. *Materials Performance* (2002).

69. S.W.Banovic, J.N.DuPont, and A.R.Marder, Dilution and Microsegregation In Dissimilar Metal Welds Betweeen Super Austenitic Stainless Steel and Nickel Base Alloys. *Science and Technology of Welding and Joining* **7**, 374-383 (2002).

70. T.Ogawa and T.Koseki, Welding High-molybdenum Superaustenitic Stainless Steel. *Materials Selection & Design* 87-91 (1996).

71. R.Fenn and C.J.Newton, Corrosion of Two Similar Austenitic Stainless Steels When Welded. *Materials Science and Technology* **2**, 181-188 (1986).

72. A.H.Tuthull and R.E.Avery, Corrosion Behavior of Stainless Steel and High-Alloy Weldments in Aggressive Oxidizing Environments. *Welding Journal* **72**, 41s-49s (1993).

73. J.N.DuPont, S.W.Banovic, and A.R.Marder, Microstructural Evolution and Weldability of Dissimilar Welds Between a Super Austenitic Stainless Steel and Nickel-Based Alloys. *Welding Research* 125-135 (2003).

74. A.Garner, Corrosion of high Alloy Austenitic Stainless Steel Weldments in Oxidizing Environments. *NACE* (1982).

75. A.Garner, Pitting Corrosion of High Alloy Stainless Steel Weldments In Oxidizing Environments. *Welding Journal* **62**, (1983).

76. C.D.Lundin, W.Liu, G.Zhou, and C.Y.P.Qiao, Unmixed Zone In Arc Welds: Significance On Corrosion Resistance of High Molybdenum Stainless Steels. *Welding Research Council Bulletin* **428**, (1998).

77. G.S.Frankel and Z.Xia, Localized Corrosion and Stres Corrosion Cracking Resistance of Friction Stir Welded Aluminum Alloy 5454. *Corrosion* **55**, 139-150 (1999).

78. J.Corral, Y. L. E.A.Trillo, and L.E.Murr, Corrosion of Friction-Stir Welded Aluminum Alloys 2024 and 2195. *Journal of Materials Science Letters* **19**, 2117-2122 (2000).

79. T.G.Gooch, R.N.Gunn, and S.B.Dunkerton. Friction Welding and Corrosion Resistance of High Alloy Austenitic Stainless Steel. Weldability of Materials 81-89 (1990).

80. ASTM E112-95: "Standard Test for Determining Grain Size". *American Society for Testing and Materials* (1995).

81. ASTM E384: "Standard Test Method for Microhardness of Materials". *American Society for Testing and Materials* (1989).

82. J.N.DuPont, C.V.Robino, and A.R.Marder, Modeling Solute Redistribution and Microstructural Development In Fusion Welds of Nb-Bearing Superalloys. *Acta Mater* **46**, 4781-4790 (1998).

83. K.F.J.Heinrich, A.D.Romig Jr., and W.F.Chambers, *Microbeam Analysis* **21**, 279-280 (1986).

84. L.E.Friedersdorf and K.Luer. Susceptibility of AL-6XN Gas Tungsten Arc Weldments To Localized Corrosion. Atlss Report No. 03-09, Bethlehem, Pa, Atlss (2003).

85. B.Dixon, P.Calleja, I.Jackson, J.Russell, G.Ryan, A.Gunner, and S.Lynch. Low Ductility Fracture of Welded Superaustenitic UNS S31245 Stainless Steel. ASM International. Trends In Welding Research 865-869 (1999).

86. M.R.Finlay and F.Orszag. Sigma Phase Embrittlement of 304H Austenitic Stainless Steel. New York, ASME. ASME Pressure Vessels and Piping Conference 253-260 (1997).

87. R.S.Mishra, S.R.Sharma, N.A.Mara, and M.W.Mahoney. Mechanical Properties of Friction Stir Welded Aluminum Alloys. Joining of Advanced and Specialty Materials. (2000).

88. K.N.Krishnan, On the Formation of Onion Rings in Friction Stir Welds. *Materials Science & Engineering A* **A327**, 246-251 (2001).

89. R.A.Prado, L.E.Murr, D.J.Shindo, and K.F.Soto, Tool Wear in the Friction-Stir Welding of Aluminum Alloy 6061 + 20% Al2O3: a Preliminary Study. *Scripta Materialia* **45**, 75-80 (2001).

90. M.B.Ives, Metallography of Pitting Corrosioin. *Materials Characterization* **28**, 257-270 (1992).

91. Z.Szklarska-Smialowska, D.Grimes, and J.Park, The kinetics of Pit Growth on Alloy 600 in Chloride Solutions at High Temperatures. *Corrosion Science* **27**, (1987).

Vita

Suzanna M. Klingensmith was born September 6, 1979 in Pittsburgh, Pennsylvania, to Marshall and Sandi Klingensmith. She grew up with her two older sisters, Shellee and Kristin, in Allegheny Township, PA. While attending Kiski Area high school, she was participated in track and field, volleyball, basketball, and softball and was also a member of the chorus. Suzanna graduated in 1998 and continued her education at Lehigh University. She studied Materials Science and Engineering and was a member of the Women's Varsity Track and Field Team. Suzanna received her Bachelor Degree in 2002 and continued on at Lehigh University to receive her Master Degree in Materials Science and Engineering in 2004.

END OF TITLE